UNIVERSITY ROMA TRE
Department of Engineering

Doctoral School in Engineering

Alleviation of Rotorcraft BVI Noise and Vibrations through Control Algorithms Based on Efficient Aeroelastic/Aeroacoustic Formulations

by

Alessandro Anobile

. . . . . .

Supervisor
Prof. Massimo Gennaretti . . . . . .

Co-supervisor
Dr. Giovanni Bernardini . . . . . .

Doctoral School Coordinator
Prof. Edoardo Bemporad . . . . . .

Rome, June 2015

a Barbara,
costante fonte di forza e di equilibrio

"A helicopter is an assembly of forty thousand loose pieces, flying more or less in formation".

(anonymous helicopter pilot)

Acknowledgements

Vorrei ringraziare in questa sezione tutti coloro che hanno svolto una parte nel mio percorso di studi degli ultimi anni.

Vorrei ringraziare prima di tutto il mio relatore, Massimo Gennaretti, per la sua insostituibile guida, il suo supporto e per l'impegno e la passione dimostrati nell'insegnamento e nella ricerca. Non avrei potuto immaginare guida migliore per il tracciamento della rotta durante gli anni trascorsi insieme.

Accanto a lui, un grazie di cuore va di certo al mio co-relatore, Giovanni Bernardini, verso di lui riservo profondo riconoscimento per i preziosi insegnamenti e per le numerose ore dedicate al mio lavoro.

Vorrei anche ringraziare chi in questi anni ha svolto un ruolo all'interno del gruppo di ricerca in cui ho avuto il piacere di lavorare. Sempre disponibili a fornire il proprio supporto e condividere conoscenza, mi riferisco a Jacopo, Marco e Daniel, che hanno contribuito a creare un ottimo ambiente in cui portare avanti i miei studi.

Ho poi desiderio di ringraziare con affetto la mia famiglia, per avermi dato la possibilità di fare le mie scelte, e con cui voglio condividere la soddisfazione del percorso seguito, frutto anche di loro sacrifici.

Un grazie sincero, inoltre, agli amici con cui ho condiviso importanti momenti negli ultimi anni, fuori e dentro l'Università. Un grazie di cuore soprattutto ad Angelo, Emanuele, Eugenio, Francesco, Paolo, Riccardo, Simone.

Infine, vorrei ringraziare Barbara, a cui dedico questo lavoro, sempre al mio fianco nei momenti felici e in quelli bui. Con la sua forza, il suo sostegno e la serenità che ha saputo donare agli anni insieme, sono riuscito ad affrontare con soddisfazione non solo il Dottorato.

Un grazie a tutti voi,
Alessandro

Abstract

Because of their peculiar ability to take off vertically and their excellent handling qualities in hover and low speed flight conditions, helicopters can play several roles beyond the capabilities of fixed-wing aircraft. However, the high levels of vibrations and noise generated represent nowadays critical issues limiting the helicopters operations both in civilian and military scenarios. Among the several sources contributing to the overall levels of vibration and noise, the main rotor plays a fundamental role through complex aerodynamic and aeroelastic phenomena affecting its operation. The rotorcraft research community is currently involved in exploring several active and passive approaches suited to reduce these annoying effects, and a lot of attention is particularly given to noise aerodynamically generated by main rotor when blade-vortex interactions (BVIs) occur. In this context, the aim of the thesis is to provide efficient formulations for performing fast and accurate rotor aeroelastic and aeroacoustic analyses. The availability of numerically efficient tools is extremely useful, for example, in early stages of design, optimization, and control synthesis, due to the high number of simulations that might be required. Some applications of the numerical tools developed are also presented in the thesis, in order to investigate different active and passive approaches for reducing vibration and BVI noise due to the helicopter main rotor. In particular, a procedure of advanced blade optimization is investigated as passive approach. In this procedure, blade shape and its mechanical/structural properties are selected using a genetic optimization algorithm, in order to reduce annoying vibratory loads at different flight conditions. In examining active control approaches, benefits achievable through the active twist rotor (ATR) solution are evaluated, investigating control effectiveness of both high-frequency and low-frequency actuators. The optimal, multi-cyclic, control theory is applied to identify the control law driving the ATR actuation. In all the applications proposed, rotor simulations are obtained by combining aerodynamic, aeroelastic and aeroacoustic tools able to accurately capture wake-blade mutual positions, which plays a crucial role in vibration and noise generation. In particular, rotor aeroelastic behaviour is described by a non-linear, beam-like model, coupled with a quasi-steady sectional aerodynamic formulation, taking into account three-dimensional

effects by a free-wake inflow correction. The evaluation of the wake inflow is obtained by a boundary element method (BEM) suited for the analysis of helicopter rotors in arbitrary flight conditions, including those affected by strong aerodynamic body-wake interactions. Concerning the noise emitted by the rotor, it is evaluated through solution of the well-known Ffowcs Williams and Hawkings equation, which governs the propagation of acoustic disturbances aerodynamically generated by moving bodies. Specifically, the boundary integral Formulation 1A developed by Farassat is used. In this thesis, an accurate and efficient approach is presented for predicting blade airloads used for the aeroacoustic solution. It relies on the Küssner-Schwarz aerodynamic sectional theory, coupled with wake inflow information obtained through three-dimensional, free-wake aerodynamic solutions of trimmed rotor aeroelastic responses. In order to provide inflow corrections to sectional formulations used for both the aeroelastic solution and the blade airloads prediction, surrogate inflow models are also introduced in the thesis, as good trade-off solution between accuracy and computational efficiency. Furthermore, different algorithms for blade optimization and active control synthesis, aimed at efficiently exploiting aeroelastic and aeroacoustic models for the specific considered applications, are described. Several numerical investigations are presented to demonstrate the capability of the proposed approaches and examine their performance in the optimization and active control applications considered. In particular, single-point and multi-point optimization procedures are successfully applied to define low-vibrating rotor blades at the flight condition(s) considered, showing difficulties to guarantee significant vibratory loads reductions in off-design flight conditions, even if multi-point optimization is considered. A sensitivity analysis of the results obtained to the aerodynamic models used is carried out, confirming suitability of the surrogate models introduced in optimization problems. A final acoustic assessment of the optimal rotor obtained is performed, confirming the more acoustically annoying nature of low-vibrating rotors. Then, the high-frequency ATR control application is numerically investigated. Two different closed-loop controls are obtained, leading to significant reductions of the higher-harmonic noise in some areas of the acoustic field through limited blade twist imposed. In both cases, vibratory levels appears to be unaffected by control actuation, confirming the advantage of high-frequency controllers in terms of drawbacks onset. Finally, attention is focused on low-frequency ATR control strategy. In a preliminary analysis, 2/rev frequency appears to be effective in reducing BVI noise, with limited drawbacks in terms of increase of vibratory loads and low-frequency acoustic disturbance with respect to other frequencies considered. Hence, a 2/rev closed-loop noise control is

numerically applied, showing an overall satisfactory reduction of the BVI noise in the acoustic field, with limited increase of low-frequency noise and vibratory hub loads.

Contents

List of Figures

Chapter 1

Introduction and Literature Review

1.1 Crucial steps in helicopter history

First studies on machines for vertical flight are attributable to the mind of Tuscan genius Leonardo da Vinci. Starting from observation of nature, he understood some of fundamentals of flight, and materialized these notions in several ideas survived to this day through his countless and accurate drawings and notes. The so-called "airscrew" (Figure 1.1) is one of Leonardo's flight

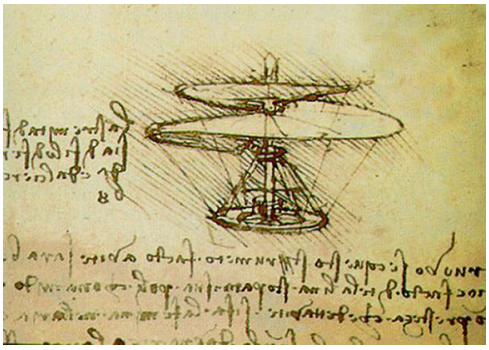

Figure 1.1: Leonardo da Vinci's "airscrew", drawing and notes (1483-86).

machines and the first concept of a vertical flight machine. It goes back to years 1483-86, well in advance with respect to first airplanes. It consists of a helical screw, connected to a platform, able to generate lift force during its rotational motion. The device so conceived was not able to fly, but represents a first concept of rotary wing aircraft.

The development resumed at the end of eighteenth century, when the Russian Mikhail V. Lomonosov presented the first self-propelled model of a lifting airscrew at Russian Academy of Sciences (1754). The French Launoy and Bienvenu answered thirty years later presenting, at the French Academy of Sciences, a device consisting of two counter-rotating propellers driven by action of an elastic bow.

One of Leonardo's airscrew issues was solved with the counter-rotating propellers: the need of balancing propulsion torque. Another problem, unmanageable in those years, still remained unsolved: availability of sufficient power to lift a relatively heavy body. The Italian engineer Enrico Forlanini provided an answer in August 1877. His models, with a weight hardly more than 3.5 kg, flew up to a height of 13 meters, remaining there for 20 seconds. This was possible thanks to two-bladed, coaxial, contra-rotating rotors powered by a steam engine. It was the first machine heavier than air and equipped with a real engine to succeed in rising from the ground.

Introduction of internal combustion engines at the end of the 19th century could provide to the first rotary wing aircraft enough power to permit flying, without adding excessive weight and dimension. In that period, also the activities of Juan de la Cierva were noteworthy for rotorcraft development. He built airplanes in Spain since 1912, but after some years with several accidents and failures mainly due to stall at low airspeed, he started to consider the possibility to install a single rotor on those airplanes, only to generate lift. The result was one of the first successful rotorcraft, which he named autogiro in 1923 (in Figure 1.2 the C-4 prototype). With the autogiro, achieving higher flight speeds became possible, experiencing for the first time the effects of lift asymmetry between advancing and retreating blades, a condition leading to the onset of an unbalanced, ungovernable, rolling moment. Juan de la Cierva overcame the problem by introducing flapping hinges, which allow the blades to move out of rotor plane, in order to assume an equilibrium under the action of aerodynamic and inertial loads, without affecting hub, and helicopter, motion.

Figure 1.2: C-4 (1923), first autogiro able to flight (`www.helistart.com`).

The 1940 was the year of the first free flight for the Vought-Sikorsky VS-300 (in Figure 1.3), often identified as the first modern helicopter. It was designed in the United States by the Russian-born engineer Igor Sikorsky. It is considered one of the first practical helicopter, in that it was able to perform manoeuvres that we now take for granted: vertical take-off and landing, hovering and forward, backward, and sideways flight. The VS-300 was powered by a 4-cylinder, 75hp Lycoming engine. It exploited a swashplate for main rotor control through imposing collective and cyclic blade pitch angles, and it had a single anti-torque tail rotor at the end of a tail which also supported a large fin. The key role of VS-300 in rotorcraft industry development was summed up, twenty years after its introduction, by Lee S. Johnson, general manager of Sikorsky Aircraft: "Before Igor Sikorsky flew the VS-300, there was no helicopter industry; after he flew it, there was."

Figure 1.3: Igor Sikorsky in the VS-300, in 1941 (`www.helistart.com`).

In 1946, the Bell 47 (model Bell 47G is reported in Figure 1.4) was the first helicopter certified for civilian use. It was designed and produced by Bell Aircraft, with the important contribution of Arthur M. Young, which introduced the rotor stabilizer bar (also known as a flybar). The Bell 47 was produced in several countries, and became the most popular helicopter model for nearly 30 years.

After the second world war, helicopter evolution saw an acceleration in terms of both numbers and performance, under impulse of new applications for civilians and increasingly advanced requirements in military field.

Nowadays[1], due to the particular operating characteristics, the helicopter

[1]Further information about history and technological evolution of helicopters can be found in Refs. [2, 8, 9].

Figure 1.4: Bell 47G, introduced in 1948 (`www.helistart.com`).

is chosen to conduct large number of tasks, not possible with other aircraft configurations. Among its missions there are passenger and cargo transportation, medical assistance and evacuation, aerial fire-fighting, search and rescue, constructions, tourism, and aerial observation. It is also widely used in military operation, for several tactical tasks. Although helicopters are limited in terms of payload, range and speed, they are the only possible choice when hovering, or excellent low-speed flight performances and handling qualities are required. An attempt to overcome the helicopter limitations is represented by the tiltrotor (the AgustaWestland AW-609 is reported in Figure 1.5a), which combines vertical lift capability with the speed and range of a conventional fixed-wing aircraft. Indeed, it has fixed (or partially fixed) wings with one or more powered rotors mounted at the tips. These rotors are installed on tilting nacelles, or movable wing sections, and are able to rotate in order to provide thrust both in vertical and horizontal flight. Other attempts to overcome helicopter limitations are represented by several compound helicopter configurations, re-appeared in recent advanced designs. They are helicopters with an auxiliary propulsion system providing additional thrust to increment maximum forward speed. Sometimes little wings or coaxial rotors could be present in order to reduce loads on the blades. In Figure 1.5b the Sikorsky X2 technology demonstrator is shown.

1.2 Focusing on main rotor: still open issues

As seen in the brief historical overview above, modern helicopters can be considered fairly new machines, still requiring significant improvements. In particular, there are considerable resources employed in optimization of main rotor, in terms of its aerodynamic/aeroelastic behaviour, in order to improve its performance and reduce noise and vibratory emissions, as required by increasingly stringent certification requirements and low level of community

(a) AW-609 (`www.helistart.com`).

(b) Sikorsky X2 (`www.wired.com`).

Figure 1.5: Innovative configurations for rotary wings aircraft.

acceptance.

Main rotor plays a fundamental role in helicopter dynamic, providing lift, propulsion, and control for the aircraft. Aerodynamic field around it is considerably more complex than around airplane wings, for several reasons: asymmetry in loads distribution over advancing and retreating sides of rotor disk, presence of strong unsteadiness, and the complex three-dimensional nature of phenomena involved, such as wake formation that, in particular flight conditions, remain close to the rotor disk, making the system simulation even more difficult. Thus study and full understanding of phenomena involved, as well as accurate prediction and simulation of rotor behaviour, result challenging tasks. The main rotor itself suffers, in terms of performance, for several aerodynamic problems, which could limit the overall capabilities of entire helicopter. Moreover, main rotor plays a fundamental role in generation of helicopter noise and vibratory loads, because of several aerodynamic and aeroelastic phenomena affecting its operation; and these annoying effects represent nowadays critical issues that hinder a further increase in using helicopters in both civilian and military scenarios.

In particular, high level of vibrations are problematic not only for pilot and passenger comfort, but they also affect fatigue life of structures, maintenance costs, on-board instrumentation efficiency, as well as acoustic disturbance inside the cabin. At the same time, external noise emission causes community annoyance, thus limiting public acceptance of helicopters for operations nearby populated areas. High noise levels can also facilitate helicopter detectability in military operations, limiting its tactical importance. Hence, prediction and control of vibrations and noise emission, in terms of magnitude and directivity pattern, are of primary interest for rotorcraft designers, both for civil applications and for improving stealthiness in military missions.

As already stated, main rotor plays a fundamental role in the noise generation through several aerodynamic and aeroelastic phenomena affecting its operation. Figure 1.6 illustrates numerous sources and generating mechanisms present in a helicopter and their spectral contents. Low frequency

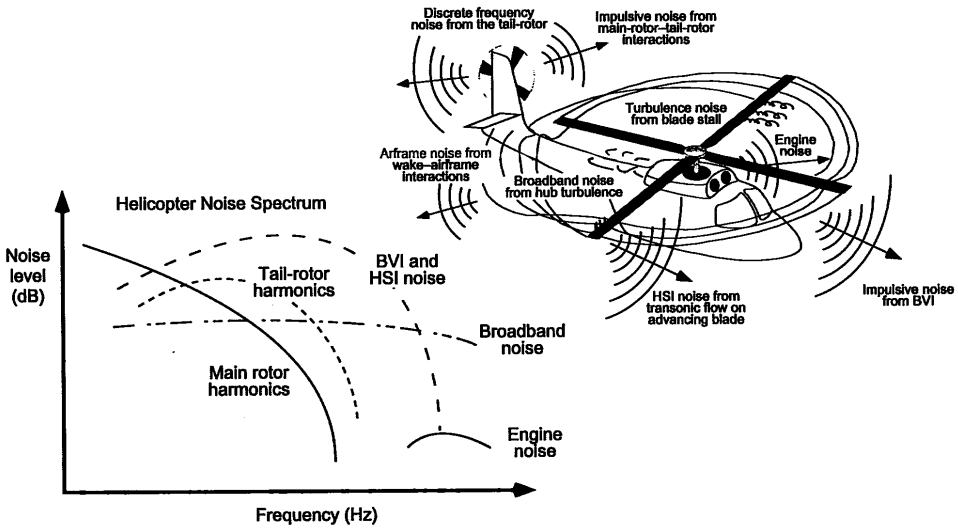

Figure 1.6: Sources of noise in a helicopter [1, 2].

noise content is mainly represented by loading noise and broadband turbulence noise, which are sources present in any condition. Other sources related to the main rotor, such as Blade Vortex Interaction (BVI) noise and High Speed Impulsive (HSI) noise, are dominant in specific flight regimes. Among these, BVI becomes a relevant source of noise when helicopter is in descent and slow advancing flights, and it can be a critical contribute. Indeed, BVI noise [10–12] has an impulsive nature, particularly annoying for the human ear, and it typically occurs when the helicopter is in approaching flights, namely when it operates near the ground and the community. As a consequence, prediction and control of BVI noise (in terms of magnitude and directivity pattern) are important issues for rotorcraft designers both for civil applications and for improving stealthiness in military missions. Regarding the HSI, it can be significant when helicopter airspeed is particularly high and compressibility effects become important. Among the several sources of noise presented, in this work the attention is mainly focused on BVI, because of its critical role in community acceptance of helicopters.

1.3 Literature review on approaches for vibrations and noise reduction

High levels of vibration and noise generated by rotors are thus important factors inspiring negative community response to helicopter operations, and also limiting their use in military missions. As a consequence, during last decades rotorcraft research community has been involved in exploring several active and passive approaches suited to reduce these annoying effects, as well as in studying procedures for the definition of optimal minimum noise descent trajectories [13], in order to reduce the acoustic impact of helicopters on communities.

A first attempt in helicopter vibration reduction could be based on fuselage, hub or blade mounted passive absorbers. These devices act on vibrations suppression only after their generation, and generally include significant weight penalty. During the brief history of modern helicopter, a wide variety of passive devices have been introduced. Many of them basically consist of extra masses attached by spring to a forced body, and they are able to reduce its vibration amplitude by properly choosing the natural frequency of the mass-spring systems [3]. In Figure 1.7 a centrifugal pendulum (bifilar) absorber developed by Sikorsky is shown. As stated before, presence of these

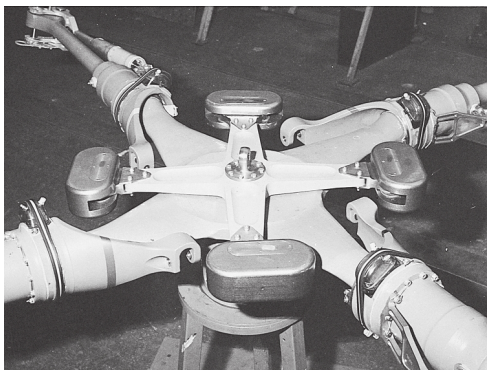

Figure 1.7: Bifilar absorber installed on Lynx rotor head [3].

devices is often associated to weight penalty and increased aerodynamic drag. Another kind of passive system is represented by isolation devices, based on anti-resonant principle [3,14], and usually mounted between fuselage and rotor/gearbox system. One of major drawback of these devices is their being tuned to provide the best vibration reduction at a specific frequency, with fast performance deterioration in off-design rotor operating conditions.

However, the most diffuse passive solution on modern helicopter is ro-

tor tailoring, with several innovative blade configurations investigated by manufacturers and researchers. See, for example, in Figure 1.8a the Airbus-Helicopter's Blue-Edge blade with its double swept tip, and in Figure 1.8b a close-up of the BERP IV tip, the blade installed on the AgustaWestland AW-101. Blade tip shape, airfoils, mass and stiffness distributions are carefully selected through multi-disciplinary optimization procedures in order to alter blade aeroelastic behaviour and achieve specific targets in different aspects [10, 15–26], such as alleviation of vibrations and noise or improvement in flight performance. A critical review concerning the use of optimization techniques in helicopter engineering is presented in [27].

(a) Blue-Edge blade (`www.wired.com`).

(b) BERP IV blade (courtesy of Burkhard Domke).

Figure 1.8: Advanced blade configurations.

Investigations into passive approaches based on blade tailoring have shown how blade design aimed at reducing vibrations can provide results more promising then those attainable by vibration absorbers and isolators [28]. These approaches are used also for noise alleviation, achieving reduction of several dB with respect to simpler solutions with rectangular blades and constant airfoil distribution [12].

The major advantage of passive solutions is that they require no activation power. Also the simplicity of absorbers and isolation devices is a plus, but they often involve a significant weight penalty and drag increase [29]. In addition, an important drawback of passive solutions is their fixed configuration in design. It permits to have moderate improving in vibration levels only in particular flight conditions and, for some solutions, only at specific locations in fuselage, such as, for example, pilot seat or avionic housing. Moreover, the use of optimal aeroelastic tailoring for the blades may lead to higher manufacturing costs.

Although passive approaches have proven themselves to be effective in

both vibration and noise alleviation, desire to achieve better results, coupled with increased technological capabilities, has stimulated investigation of active control systems for the same aim. Approaches based on higher harmonic control (described in Chapter 3) have been investigated in detail both numerically and experimentally in the recent past literature [11, 12, 28, 30–42]. Specifically, the attention has been focused mainly on two types of control systems: the individual blade control (IBC), and the so-called higher harmonic control (HHC). In the IBC systems each blade is independently controlled in the rotating frame through pitch links, flaps or other devices. Figure 1.9a shows an example of IBC actuated by trailing-edge flap in experimental tests performed by Boeing, NASA and other partners in the Ames wind tunnel. On the other hand, HHC systems act on all the blades simulta-

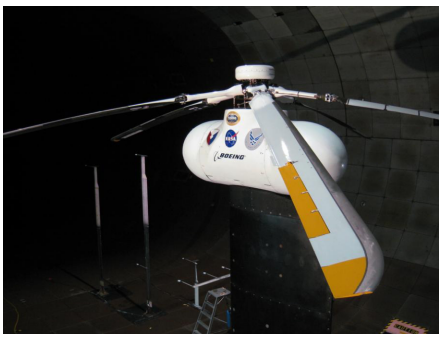

(a) SMART rotor tests [43].

(b) Rotor head close-up (courtesy of Burkhard Domke).

Figure 1.9: Examples of helicopter rotor control actuations.

neously through actuators installed underneath the non-rotating, swashplate component[2] (in Figure 1.9b a clear picture of a swashplate is shown, related to the rotor head of an Aérospatiale SA 330 Puma helicopter). Working through actuation of the non-rotating component, HHC can only provide a limited set of control frequencies in the rotating frame.

Benefits and drawbacks of both these systems in reducing vibrations and acoustic disturbance have been widely investigated, with the IBC approach

[2]The swashplate is a device that, with its motion, transmits pilot controls from the non-rotating fuselage system to the rotating rotor hub and blades. It consists of two main parts: a stationary component and a rotating one. The stationary swashplate is connected to the control chain, starting from the pilot, and is able to translate vertically and tilt in all directions. It transmits this motion to the rotating component, which is able to rotate, being mounted by means of a bearing. The upper part of the rotating swashplate is connected, via pitch link, to the blades, and transmits to them its motion, altering their pitch angle.

proven to be potentially more effective than the HHC one, which presents, however, benefits in terms of technological simplicity, as well as in terms of applicability to existent machines, without requiring massive adaptations.

Superiority of IBC mainly lies in capability of controlling virtually every frequency, acting on each blade in rotating frame. This advantage is evident for example in reducing BVI noise, which appear particularly influenced by the 2/rev frequency [12, 38, 40, 44]; indeed, the HHC is not able to act at this frequency in the case, for example, of a four- or five-bladed rotor. As already stated, IBC systems present several problems connected to increase of weight, as well as to complexity and vulnerability of the actuation devices.

Active materials and, in particular, piezoelectric materials, permit to overcome most of the limitations listed above, as addresses in some advanced designs recently presented [4, 12, 45, 46]. Indeed, capability of these materials to directly convert electrical signals in mechanical deformations allows low-mass and high-bandwidth actuators. These materials can be exploited to drive a trailing edge flap or to generate blade twist through span-wise distributed structure-embedded actuators, in the so-called active twist rotor (ATR) system. The latter solution is nowadays extensively studied by the German DLR [4, 12], and in Figure 1.10 a set of their blade demonstrators is shown. The use of smart materials increases ability to control aeroelastic

Figure 1.10: DLR active rotor blade demonstrators [4].

behaviour of each blade, for altering blades motion or cancelling unsteady aerodynamic loads, *i.e.*, the main causes of rotor noise and vibrations. As a consequence of what stated above, in recent years increasing attention to application of smart materials to rotorcraft systems has been paid by research community [4, 36, 45, 47–49] .

Finally, further observations have to be made for application of active controls in the specific problem of BVI noise alleviation, which is one of the

main topics of this work and one of the most interesting application of active control systems. Indeed, active controls seem to be particularly suitable for BVI noise alleviation, in that this kind of phenomenon is mostly relevant in low speed flight, when more power is available to actuators, compared to high speed forward flight. However, in this case there are additional drawbacks besides those related to the increase of weight and complexity due to actuation devices. Indeed, the way these controllers act for maximum BVI noise reduction, often corresponds to an increase in low-frequency noise content and in rotor vibration levels [37, 50].

This problem suggest to close this Section observing that a judicious combination of both active and passive techniques for vibration and noise reduction seems likely to provide the optimal rotor design, as also stated by other authors [11, 51].

1.4 About this work

As seen in the previous Section, research community is nowadays still focused on several topics related to rotorcraft field, with particular attention to those issues concerning application of control systems for reducing vibration and/or noise, and to increase helicopter performance. In the introduction, difficulties in rotorcraft systems simulation, related to the complex phenomena involved (especially aerodynamic ones), have also been mentioned. Those issues make the research of innovative and technologically feasible solutions a difficult and challenging task.

1.4.1 Aim of the thesis

The work illustrated here is framed into the context described above. Its purpose can be schematically described in two main points:

i) provide fast and accurate procedures and numerical tools for rotor aeroelastic/aeroacoustic analysis, useful for early stages of design, optimization, and control synthesis;
ii) present some applications of these tools in order to investigate different approaches for reducing vibrations and BVI noise due to the helicopter main rotor.

Concerning the applications proposed, attention is focused both on active and passive techniques. In particular, a procedure of advanced blade optimization has been investigated as passive approach. In this procedure, blade shape and its mechanical/structural properties are selected using a genetic optimization

algorithm, in order to reduce annoying vibratory loads at different flight conditions. Remarkable results have been presented in Refs. [52, 53].

In examining active control approaches, benefits achievable through the active twist rotor (ATR) solution are evaluated, investigating control effectiveness of both high- and low-frequency actuators [54, 55].

In order to obtain the results presented in this thesis, a number of advanced numerical tools has been used for simulating several aspects concerning helicopter main rotor behaviour, covering from blade aeroelastic analyses to accurate aerodynamic and aeroacoustic calculations. Some of these tools have been developed or modified during this thesis, to fit them to specific problems faced and with the high numerical effort needed in optimization and control synthesis procedures. However, most of these numerical tools are based on advanced solvers developed in the last two decades by the research group of Prof. Gennaretti, at Engineering Department of University Roma Tre (Rome, Italy). In the thesis also specific algorithms are introduced for enhancing optimization and control synthesis procedures.

In this section, the motivations that have led to this work are briefly illustrated, as well as the answers this thesis has given, in improving simulation capability and numerical performance of the numerical tools used in optimal design and control synthesis. In the following Chapter 2, algorithms and formulations used in this work will be described in detail, with particular attention to those introduced during this thesis.

Rotor modelling

As stated above, three main numerical solvers have been used to simulate the rotor behaviour:

i) a solver for blades aeroelastic analysis;
ii) a numerical tool for unsteady, three-dimensional, potential flows aerodynamic simulation;
iii) an aeroacoustic solver for emitted noise predictions.

A fundamental role in these simulations is played by computational tool applied for aeroelastic analysis of the rotor since, for correct prediction of vibratory loads and BVI noise emitted, the accurate knowledge of blade and wake mutual positions is a crucial factor. This represents a not easy task, involving complex, unsteady, three-dimensional aerodynamic phenomena, coupled with the structural dynamic of blades, which are slender bodies undergoing moderate deformations. In case of optimal design of blade shape, also the possibility to study blades with curved elastic axis (for the presence of swept and/or anhedral angles) contributes to increase the problem complexity.

One of the earliest structural models for swept tip blades has been presented and successfully applied to hingeless rotor blades in Refs. [56,57], while a formulation for blades with varying sweep, droop, twist angles and platform has been later introduced in Ref. [58]. In the present work, the rotor aeroelastic tool applied is based on a beam-like model spatially integrated through a Galerkin approach, deriving from the non-linear, bending-torsion formulation presented in Refs. [59, 60], which is valid for slender, homogeneous, isotropic, non-uniform, twisted blades, undergoing moderate displacements. The original formulation has been enhanced, in order to consider blades having arbitrarily curved elastic axis, including geometrical discontinuities as sweep and anhedral tip angles. The resulting tool was presented and validated in Refs. [6, 7, 52]. In performing aeroelastic analyses, distributed aerodynamic loads are evaluated by span-wise integration of loads given by quasi-steady approximation of the Greenberg sectional theory [60,61]. Three-dimensional, unsteady effects deriving from the wake vorticity are taken into account through a proper wake inflow correction.

Evaluation of wake inflow is carried out through the second numerical tool listed above, the numerical solver suited for simulation of unsteady, three-dimensional, free-wake, rotor aerodynamics. It is based on the boundary element method (BEM) for solution of the boundary integral equation, and it is formulated to be suitable for aerodynamic simulation also when strong body-wake interactions occur [62]. The same aerodynamic solver could be used in obtaining both inflow correction and pressure distribution on blades surface, which is essential to predict rotor radiated noise. Coupling the BEM solver with the aeroelastic code in an iterative process permits to achieve accurate trimmed aeroelastic solutions, taking into account also the three-dimensional and unsteady effects related to free evolution of wake vorticity. This technique leads to high computational costs, since it involves several calculations performed through numerical expensive BEM formulation for accurate simulation of aerodynamic phenomena. The problem complexity grows even further when this technique is integrated in optimization algorithms, in control synthesis procedures or implemented in on-board closed-loop controllers, where huge number of simulations need to be performed, or real time evaluations might be required. In these cases, a good trade-off solution between accuracy and computational efficiency could lie in using less expensive surrogate models (or meta-models), which can replace or reduce the intense computer analyses. This approach is widely used in multidisciplinary design optimization problems [63, 64]. In this thesis, a surrogate model of wake inflow, used for sectional aerodynamic loads prediction, is introduced for both the case of optimal blade design for vibration reduction and for active con-

trol synthesis aimed at reducing BVI noise generated. In the first case, the use of surrogate models for wake inflow determination is made even more important by choosing optimization procedures based on genetic algorithms for optimal blade design. Although these algorithms seem to be appropriate approaches to achieve the optimal solution, being able to avoid local minima and search for the global optimum even in extremely complex problems, they might required a huge number of calculations to find the optimal blade configuration[3]. This surrogate model is based upon interpolation of a database of BEM wake inflow evaluated off–line for a limited number of configurations falling in the domain of definition of the problem. Hence, a limited number of configurations (and, consequently, a limited number of off-line calculations), which differ for values of some key parameters, are sufficient to define the surrogate database to be interpolated in the whole domain of problem definition. Different interpolation tools have been used, obtaining interesting results [53]. One of these is based upon artificial neural networks, and it is developed during this thesis. Further details on this topic could be found in Refs. [67, 68].

In case the performed analysis focuses the attention on noise emitted, as for controllers synthesis for BVI noise alleviation, also the aeroacoustic code become necessary. The numerical tool aimed at noise prediction used for this thesis is based on the solution of Ffowcs Williams and Hawkings equation [69], which governs the propagation of acoustic disturbances aerodynamically generated by moving bodies. It takes, as input, pressure distribution on the body/bodies examined, and provides noise emitted at specific positions identified. As stated above, pressure distributions could be predicted through the BEM solver with high computational cost for each configuration considered. For the sake of numerical efficiency, in this thesis an accurate and efficient approach is proposed for the prediction of blade airloads to be provided to the aeroacoustic solver. It relies on the determination of the blade pressure distribution by the Küssner-Schwarz theory [70] (see Section 2.4.2), coupled with wake inflow from the database obtained through the BEM solver for specific trimmed rotor aeroelastic responses. A description of this approach and several application have been published in Refs. [55, 71, 72].

[3]Interested readers may find details on genetic algorithms optimization procedures in Refs. [65, 66]

Numerical applications

Numerical tools just described have been tested in some interesting applications of active and passive systems for reducing vibrations and BVI noise generated by helicopter main rotors.

A binary genetic optimization algorithm, coupled with a wake inflow database, has been used in optimal design of rotor blades characterized by minimum vibratory levels. The analyses have been performed in different flight conditions, and also robustness of solution in off-design conditions has been verified with satisfying results. Part of the work has been presented in Refs. [52, 53]

For BVI noise alleviation, active controls have been chosen, since this kind of phenomenon is relevant at low speed flight, when more power is available to actuators, as already stated before. In particular, two different IBC controllers, relying on two different approaches, have been investigated, based both on active twist rotor (ATR) actuations through smart materials embedded in the blades.

The first controller examined is aimed at direct suppression/alleviation of loads due to BVI through generation of opposite aerodynamic loads, concentrated where BVI phenomena occur. This is possible only with a localized high-frequency controller action, differently from what happens in more common approaches, which apply lower-frequency ($2 - 6$/rev) actuation to alter key factors of BVI phenomena like miss-distance and blade-vortex interaction angle. The proposed control strategy operates in bounded time slots during blade rotation through small, localized blade torsional moments, letting the system evolve unaffected by controller in the rest of revolution. In this way, BVI phenomena (and related emitted noise) are altered where they occur, minimizing the onset of negative by-products effects like, for instance, vibratory hub loads increase. Note that technological feasibility of the proposed high-frequency controller is still an open issue, although research in this field has been developed [50]. Thus, the purpose of the analyses is to explore potential performance of the approach, as well as to find interesting application for the efficient procedure introduced for synthesis of control law. Results concerning this application could be found in Refs. [54, 73].

The second individual blade controller considered is a more common low-frequency IBC, which exploits smart materials actions for reducing BVI noise, acting on the generating phenomena and not on the resulting loads arising. In particular, small 2/rev blade deformations are produced to modify wake-blade interaction phenomena and related emitted noise. The aim, in this case, is altering miss-distance between blades and tip vortices, which strongly affects BVI noise. This approach, well known in literature [11,31,32,39,40,74],

represents an interesting application for the high-performance aeroacoustic analysis introduced for the control synthesis process. It consists in evaluating the aerodynamic loads needed for the prediction of the emitted noise by an analytical-numerical aerodynamic formulation [71, 72], coupled with a wake inflow database spanning a suited domain of control variables. Specifically, the general Küssner-Schwarz unsteady sectional aerodynamic theory is applied to determine the aerodynamic loads associated to arbitrary profile downwash [70], whereas the wake inflow database, including three-dimensional BVI effects, is provided by combining rotor aeroelastic solver with the free-wake, BEM solver described above. The availability of a numerically efficient tool is extremely useful in applications of optimal controller synthesis processes, due to the high number of simulations that might be required. Results concerning the application just described has been published in Ref. [55].

In both the active control applications described above, a specific insight into smart device modelling that yields actuation is considered beyond the scope of the work; in the following, it will be represented by external torques concentrated or distributed along the blade span. Furthermore, the driving control law is determined through an optimal, multi-cyclic control approach, based on simulations of rotor behaviour given by computational tools that provide predictions of both aeroelastic response and radiated noise, for arbitrary steady flight conditions.

1.4.2 Structure of the thesis

In the following chapters all procedures briefly presented above will be described in detail, and results for the numerical applications considered will be discussed. The paper is organized into four main parts, corresponding to four chapters, followed by concluding remarks, appendices and bibliography. Topics addressed in each chapter are quickly mentioned below.

Chapter 1 In this Chapter, concluding with the present section, the problem statement is introduced along with a brief description of models and algorithms used in the thesis. A literature review on the topics involved is present, as well.

Chapter 2 The models used for aeroelastic and aeroacoustic simulation of helicopter rotor are presented in this chapter, without claiming to be exhaustive. In addition, particular models introduced for reducing numerical effort of the simulations carried out are described.

Chapter 3 In this chapter, efficient algorithms for optimization and control synthesis are presented. In particular, a genetic algorithm for rotor blades optimization aimed at reducing vibratory loads generated is firstly described, emphasizing how the algorithm has been adapted to the problem examined. Then, two different multi-harmonic approaches for active control of rotor BVI noise are presented, along with the optimal, multi-cyclic control algorithm used for the synthesis of the driving control law.

Chapter 4 Finally, in this chapter, several numerical applications of the tools previously presented are proposed. Firstly, optimization processes aimed at reducing helicopter vibrations are applied, taking into account different flight conditions in the objective function. Algorithm performance and robustness of the optimal configurations achieved in off-design conditions are examined. Then, two different active twist controls are applied to a rotor model for reducing BVI noise generated in descending flight conditions. Results obtained are discussed in terms of noise control performance and onset of negative by-products effects like, for instance, vibratory hub loads increase.

Chapter 2

Rotor Aeroelastic and Aeroacoustic Simulation

2.1 Rotor aeroelastic model

For the applications examined in this thesis, accurate simulations of rotor aeroelastic behaviour represent a crucial issue. They are important for correct evaluation of vibratory loads transmitted to the hub and, even more important, for accurate prediction of interactions between blades and wake. Indeed, blade deformation and corresponding blade-wake miss distance strongly influence BVI effects [31, 32, 39, 40]. Moreover, correct simulation of rotor aeroelasticity is also important for some of the control strategies analysed, based on blade aeroelastic responses to given actuation torques. A remarkable feature of the aeroelastic model used is its capability to examine rotor blades having arbitrary shape. Indeed, also the presence of geometrical discontinuities (as sweep and anhedral tip angles) has been considered in the research of the optimal blade configuration producing lower level of vibratory loads.

2.1.1 Nonlinear beam-like formulation

The blade aeroelastic model used in this thesis combines a structural dynamics model with a quasi-steady sectional aerodynamic formulation, corrected through wake inflow contribution predicted by a three-dimensional, free-wake aerodynamic solver, to have a more accurate description of the influence of the rotor wake vorticity.

Structural dynamics of helicopter rotor blades is described through a beam-like model obtained as an enhanced version of the formulation pre-

sented in Refs. [59,60]. It is valid for slender, homogeneous, isotropic rotating blades with curved elastic axis and includes span-wise variation of mass and stiffness properties, as well as, variable built-in pre-twist, precone, sweep and anhedral angles. In order to take into account the moderate displacements usually experienced by rotor blades, non-linear strain-displacement relations are considered with application of a second order approximation scheme. A detailed description of this structural blade model is presented in Refs. [6,7].

Distributed aerodynamic loads forcing the blades are evaluated through span-wise integration of loads given by quasi-steady approximation of the Greenberg sectional theory [61], an extension of the Theodorsen theory [75] valid for rotor blades airfoils, which experience non constant free-stream. The application of the more complex Küssner-Schwarz formulation [70] (presented in the following, at Section 2.4.2) is unnecessary in this step of aeroelastic analysis, where blades cross sections are assumed to be rigid, and where the presence of extremely impulsive localized phenomena are assumed to not influence the aeroelastic blades behaviour[1].

Three-dimensional, unsteady effects deriving from wake vorticity are taken into account through the influence of the corresponding wake inflow on the body-air relative velocity at the rear aerodynamic centre of the blade sections. Wake inflow evaluation is obtained by a boundary element method (BEM) for the solution of the boundary integral equation approach presented in Ref. [62], suited for the analysis of potential flows around helicopter rotors in arbitrary flight condition. A description of this formulation is presented in Section 2.2.

In the aeroelastic model equations, a further simplification has been introduced by using the elimination approach described in Ref. [60] for the axial degree of freedom (axial displacement of the blade elastic axis), u. This approach provides a final set of three integro-partial differential equations to be integrated, and expressed in terms of section torsion rotation, ϕ, and elastic axis bending displacements, lag displacement v and flap displacement w. These equations are spatially integrated through the Galerkin approach, starting from description of elastic axis deformation as a linear combination of shape functions that satisfy homogeneous boundary conditions. Specifi-

[1]The application of the Küssner-Schwarz formulation will be crucial in determining airloads used for aeroacoustic predictions, in that allowing to take into account pressure disturbances also due to impulsive phenomena, like blade-wake interactions.

cally, it consists in expressing blade displacements as

$$
\begin{aligned}
v(s,t) &= \sum_{n=1}^{N_v} q_n^v(t)\psi_n^v(s) \\
w(s,t) &= \sum_{n=1}^{N_w} q_n^w(t)\psi_n^w(s) \\
\phi(s,t) &= \sum_{n=1}^{N_\phi} q_n^\phi(t)\psi_n^\phi(s)
\end{aligned}
$$

with q_n^v,q_n^w,q_n^ϕ Lagrangian variables of the problem, and ψ_n^v, ψ_n^w, ψ_n^ϕ conveniently chosen as bending and torsion natural modes of vibration of a non-rotating, straight, cantilever beam [60]. A more detailed description of the aeroelastic model used and its numerical implementation can be found in Appendix A.

The resulting aeroelastic system consists of a set of $(N_v + N_w + N_\phi)$ nonlinear, time-dependent, differential equations of the type

$$
\mathbf{M}(t)\,\ddot{\mathbf{q}} + \mathbf{C}(t)\,\dot{\mathbf{q}} + \mathbf{K}(t)\,\mathbf{q} = \mathbf{f}_{str}^{nl}(t,\mathbf{q}) + \mathbf{f}_{aer}(t,\mathbf{q}) + \mathbf{m}(t) \tag{2.1}
$$

where $\mathbf{M}, \mathbf{C}$, and $\mathbf{K}$ are time-periodic mass, damping, and stiffness structural matrices representing the linear structural terms, $\mathbf{q}$ is the vector of Lagrangian coordinates, and $\mathbf{m}$ denotes, where present, the generalized torque moments applied for ATR actuation. Nonlinear structural contributions are collected in the forcing vector $\mathbf{f}_{str}^{nl}(t,\mathbf{q})$, whereas vector $\mathbf{f}_{aer}(t,\mathbf{q})$ collects the generalized aerodynamic forces.

The system written in Eq. (2.1) can be solved with Lagrangian variables unknowns in order to analyse rotor blades (periodic) aeroelastic response or to perform stability analyses. In the first case, time integration could be solved using a harmonic balance approach [76–78], thanks to the periodic nature of the solution. Indeed, it is a methodology suitable for the analysis of the asymptotic solution (as time goes to infinity) of differential equations forced by periodic terms, as in the present case. Because of the presence of non-linear structural terms and of aerodynamic contributions in the resulting equation, the final system has to be solved using an iterative procedure. To this aim, the Newton-Raphson procedure is applied. In case of aeroelastic stability analysis, harmonic balance approach permits to obtain the equilibrium configuration; then the set of equations is (numerically) linearised about that equilibrium, and an eigenanalysis is performed [78].

The solution process just described plays the part of the internal iterative analysis represented in the left box in Figure 2.1. It receives wake inflow corrections from the three-dimensional aerodynamic solver (described in Section 2.2) and iteratively obtains the aeroelastic solution in terms of blade deformations. These are sent to the BEM solver as boundary conditions for an accurate aerodynamic analysis which provide an updated wake inflow correction to the aeroelastic solver, till reaching the convergence in the external loop represented in figure.

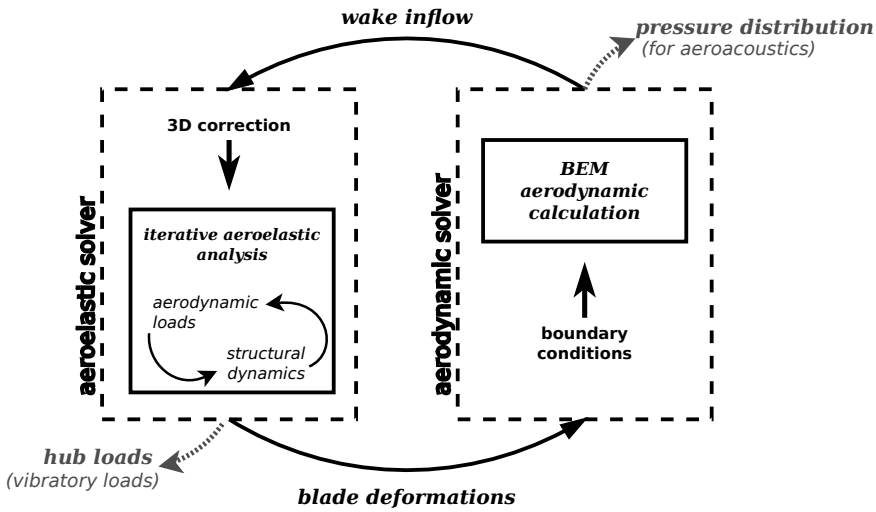

Figure 2.1: Iterative process for accurate aeroelastic simulations.

2.1.2 Linearized blade torsion dynamic response

As mentioned in Section 1.4.1, in this thesis efficient procedures for rotor optimization and active control law synthesis are introduced. One of this techniques, described in detail in Section 3.2, relies on the simplified aeroelastic model described here[2], which is used for aeroelastic simulations, instead of the complete system of non-linear equations described above, when required for computational efficiency of numerical procedures. In particular, in order to synthesize the control law for the high-frequency ATR, the required actuation torques in the closed-loop control are (rapidly, but with a satisfactory

[2]For better understanding role and importance of this simplified model, please refer to Section 3.2 and Figure 3.5, where a controller block is depicted.

degree of accuracy) determined by solution of an inverse aeroelastic rotor blade problem. It consists of a reduced version of Eq. (2.1), describing only the linear torsion behaviour. Indeed, non-linear terms are eliminated and torsional deformation is assumed to be the only blade degree of freedom left. The resulting simplified (easy to invert) aeroelastic system is:

$$\mathbf{M}_T(t)\,\ddot{\mathbf{q}}_T + \mathbf{C}_T(t)\,\dot{\mathbf{q}}_T + \mathbf{K}_T(t)\,\mathbf{q}_T = \mathbf{f}_{aer,T}(t) + \mathbf{m}(t) \tag{2.2}$$

where $\mathbf{M}_T, \mathbf{C}_T$, and $\mathbf{K}_T$ are time-periodic, mass, damping, and stiffness matrices representing the linear structural and aerodynamic contributions, $\mathbf{f}_{aer,T}(t)$ denotes the part of the generalized aerodynamic torque moments independent on blade deformation, while $\mathbf{m}$ denotes generalized torque moments devoted to ATR actuation.

2.2 Aerodynamic formulation

As stated in the previous section, aerodynamic loads collected in the term $\mathbf{f}_{aer}(t, \mathbf{q})$ of Eq. (2.1) are obtained by span-wise integration of loads from the Greenberg sectional theory [61]. However, three-dimensional, free-wake inflow corrections are needed to be able to accurately predict BVI occurrence, and its corresponding aeroelastic and aeroacoustic effects. This wake inflow is evaluated by an aerodynamic solver based on boundary integral formulation for potential flows suited for prediction of strong aerodynamic body-wake interaction effects [62]. The same solver could be used to obtain the pressure distribution on the blades surface (as schematically represented in Figure 2.1), which is essential to predict the rotor radiated noise (see the description of aeroacoustic formulation in Section 2.3). A brief description of the aerodynamic formulation is given below.

Starting from the description of the flow velocity field, $\mathbf{v}$, as $\mathbf{v} = \nabla\varphi$, and combining this with the continuity equation yields, for incompressible, quasi-potential flows[3] the Lagrange equation:

$$\nabla^2\varphi = 0 \tag{2.3}$$

Problem is completed with condition at infinity

$$\lim_{|x|\to\infty} \varphi = 0$$

[3]The aerodynamic formulation used for simulations performed in this thesis is developed for flows usually defined as quasi-potential flows. They are inviscid, initially irrotational and remain so at all times and in the whole field, with the exception of points belonging to the wake surface (S_W).

and with impermeability boundary condition on body surface:

$$\left.\frac{\partial \varphi}{\partial n}\right|_B = \chi = \mathbf{v}_B \cdot \mathbf{n}$$

with $\mathbf{v}_B$ representing the body velocity and $\mathbf{n}$ the outward unit vector normal to its surface. In these conditions, velocity potential calculated in a point, $\mathbf{x}$, of the field is given by:

$$\varphi(\mathbf{x}, t) = \int_{S_B} \left(G \frac{\partial \varphi}{\partial n} - \varphi \frac{\partial G}{\partial n} \right) d\mathcal{S}(\mathbf{y}) - \int_{S_W} \Delta\varphi \frac{\partial G}{\partial n} d\mathcal{S}(\mathbf{y}) \tag{2.4}$$

where $G = -1/4\pi r$ is the unit-source solution of the three-dimensional Laplace equation, with $r = \|\mathbf{y} - \mathbf{x}\|$, $\mathbf{y}$ represents points belonging to the body surface (S_B) or wake surface (S_W), whereas $\Delta\varphi$ is the potential jump across the wake surface. This value is known from the past history of the potential discontinuity at the trailing edge of the blades (through the Kutta-Joukowski condition), observing that it remains constant following a material point of the wake [79]:

$$\Delta\varphi(\mathbf{x}_W, t) = \Delta\varphi(\mathbf{x}_W^{TE}, t - \tau) \tag{2.5}$$

where τ is the time it takes to travel from trailing edge ($\mathbf{x}_W^{TE}$) to a generic point on the wake surface ($\mathbf{x}_W$).

In general, Eq. (2.4) can not be solved exactly. A technique to approximately solve the problem relies on discretization of body (the blades, in the case examined) and wake surfaces in several panels. For each time step, velocity of body surface must be updated[4], along with the wake surface which can have a prescribed motion or a free motion. This possibility is crucial for aerodynamic analyses in presence of BVI occurrences, but the model presented so far is still not suitable for this analysis, because of numerical instabilities which can arise in case of close interaction between wake and body surfaces.

This difficulty has been overcome with the formulation presented in [62]. In this formulation the potential field, φ, is obtained as superposition of an incident field, φ_I, with a scattered field, φ_S (*i.e.*, $\varphi = \varphi_I + \varphi_S$). The scattered potential is generated by sources and doublets over the surfaces of the blades, S_B, and by doublets over the wake portion that is very close to the trailing edge from which emanated (near wake, S_W^N). The incident potential is due to doublets distributed over the complementary wake region that compose the far wake, S_W^F (see Figure 2.2). Furthermore, the division of

[4]In case of analysis of helicopter rotor, this means to know blade motion at each time steps, in terms of kinematics and, eventually, blade elastic deformations.

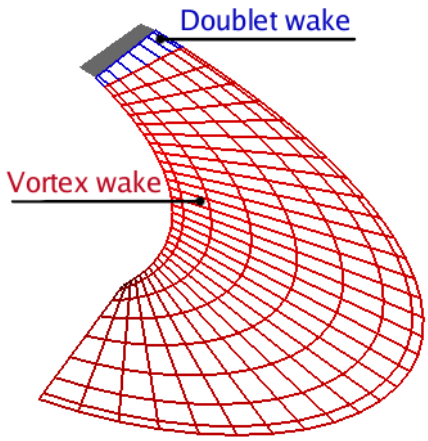

Figure 2.2: Division of blade wake surface.

the wake surface is such that the far wake is the only wake portion that may come in contact with blades. The scattered potential is discontinuous across S_W^N, whereas the incident potential is discontinuous across S_W^F. Recalling the equivalence between surface distribution of doublets and vortices, the far wake can be represented as the equivalent distribution of vortices with finite core, permitting to avoids numerical issues mentioned above[5]. Indeed, they generate a regular velocity field even nearby the body, unlike the zero-thickness distribution of doublets.

Splitting the wake into far and near parts (such that $\mathcal{S}_W^N \cup \mathcal{S}_W^F = \mathcal{S}_W$), Eq. (2.4) becomes:

$$\varphi(\mathbf{x},t) = \underbrace{\int_{\mathcal{S}_B}\left(G\frac{\partial\varphi}{\partial n} - \varphi\frac{\partial G}{\partial n}\right)d\mathcal{S}(\mathbf{y}) - \int_{\mathcal{S}_W^N}\Delta\varphi\frac{\partial G}{\partial n}d\mathcal{S}(\mathbf{y})}_{\varphi_S} - \underbrace{\int_{\mathcal{S}_W^F}\Delta\varphi\frac{\partial G}{\partial n}d\mathcal{S}(\mathbf{y})}_{\varphi_I} \tag{2.6}$$

Therefore, as demonstrated in Ref. [62], for the scattered potential the following expression can be obtained:

$$\varphi_S(\mathbf{x},t) = \int_{S_B}\left[G\left(\chi - \chi_I\right) - \varphi_S\frac{\partial G}{\partial n}\right]dS(\mathbf{y}) - \int_{S_W^N}\Delta\varphi_S\frac{\partial G}{\partial n}dS(\mathbf{y}) \tag{2.7}$$

where $\chi_I = \mathbf{u}_I \cdot \mathbf{n}$, with $\mathbf{u}_I$ denoting the velocity induced by the far wake. In turn, considering the far wake discretized into M panels, assuming the

[5]In order to assure a regular distribution of the induced velocity within the vortex core, and thus a stable and regular solution even in blade-vortex impact conditions, a Rankine finite-thickness vortex model is introduced in the equations [62].

potential jump constant over each panel, and recalling the equivalence between surface distribution of doublets and vortices, the incident velocity field is evaluated through the Biot-Savart law applied to the vortices having the shape of the far wake panel contours as [62]

$$\mathbf{u}_I(\mathbf{x},t) \approx -\sum_{k=1}^{M} \Delta\varphi_S(\mathbf{y}_{W_k}^{TE}, t-\vartheta_k) \int_{C_k} \nabla_{\mathbf{x}} G \times d\mathbf{y} \tag{2.8}$$

where $\mathbf{y}_{W_k}^{TE}$ is the trailing edge position where the wake material point currently in $\mathbf{y}_{W_k}$ emanated at time $t-\tau_k$, C_k denotes the contour line of the k-th far wake panel, and $\nabla_{\mathbf{x}}$ denotes gradient operator with respect to the variable $\mathbf{x}$. The equations above show that the incident potential affects the scattered potential through the induced-velocity term, χ_I, while the scattered potential affects the incident potential by its trailing-edge discontinuity that is convected along the wake and yields the intensity of the vortices of the far wake. Equation (2.8) is applied to evaluate both the term χ_I in Eq. (2.7) and the velocity field from which the wake shape evolution is determined in a free-wake analysis. Note again that, for an accurate prediction of BVI phenomena, the accurate evaluation of the wake distorted shape is essential in that a crucial role is played by the relative positions between body and wake.

Akin to the far wake contribution, Eq. (2.7) is solved numerically by boundary elements, *i.e.*, by dividing S_B and S_W^N into quadrilateral panels, assuming φ_S, χ, χ_I and $\Delta\varphi_S$ to be piecewise constant (zero-th order boundary element method), and imposing that the equation be satisfied at the centre of each body element (collocation method) [62]. Once the potential field is known, blade loads may be evaluated through integration [80] of pressure distribution obtained through the Bernoulli theorem. In a body-fixed frame of reference, it reads:

$$\dot{\varphi}_S + \dot{\varphi}_I - \mathbf{v}\cdot(\nabla\varphi_S + \mathbf{u}_I) + \frac{|\nabla\varphi_S + \mathbf{u}_I|^2}{2} + \frac{p}{\rho} = \frac{p_0}{\rho} \tag{2.9}$$

where the incident potential is obtained by the incident velocity [62].

After this brief description of the boundary element formulation implemented in the aerodynamic solver used, in the following Figure 2.3, an exemplary result is shown. It is an output visualization provided by the aerodynamic solver for a four-bladed rotor in severe BVI condition, in which the free-wake related to a single blade remains close to the rotor disk causing strong interactions.

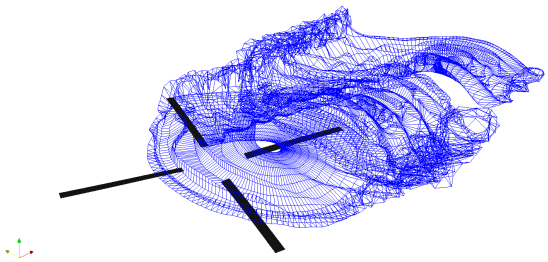

Figure 2.3: Example of a rotor in severe BVI condition.

2.3 Aeroacoustic formulation

In the aeroacoustic simulations presented in this work, noise radiated by rotor blades is evaluated through a boundary integral formulation solution of the well-known Ffowcs Williams and Hawkings equation [69]. It permits to predict acoustic disturbances aerodynamically generated by moving bodies in specific positions taking, as input data, the pressure distribution on the bodies surface provided by an aerodynamic solver.

The formulation implemented starts from the Lighthill analogy introduced in 1952 [81], and widely applied in numerical aeroacoustics, which represents a rearrangement of the mass and momentum conservation laws into the following inhomogeneous wave equation:

$$\frac{\partial^2 \tilde{\rho}}{\partial t^2} - c_0^2 \frac{\partial^2 \tilde{\rho}}{\partial x_i^2} = \frac{\partial^2 T_{ij}}{\partial x_i \partial x_j} \tag{2.10}$$

where c_0 is the speed of sound in the undisturbed medium and $\tilde{\rho}$ is the density perturbation. All the right-hand side terms are collected in the Lighthill tensor having, for inviscid flows, components:

$$T_{ij} = \rho\, u_i u_j + (p - c_0^2\, \tilde{\rho})\, \delta_{ij}$$

where u_i and u_j are components of the fluid velocity, p the undisturbed medium pressure and δ_{ij} denotes the Kronecker delta.

The formulation used in this thesis represents an extension of Eq. (2.10) due to Ffowcs Williams and Hawkings [69], which include a moving body in the field. Assuming that the flow is compressible and undergoes transformations with negligible entropy changes, the acoustic pressure disturbance is defined as $p' = c_0^2\, \tilde{\rho}$. Then, for $f(\mathbf{x}, t) = 0$ describing the moving body

(blade, for the case in exam) surface, the Ffowcs Williams and Hawkings equation reads

$$\begin{aligned} \frac{1}{c_0^2}\frac{\bar{\partial}^2 p'}{\partial t^2} - \bar{\nabla}^2 p' &= \frac{\bar{\partial}}{\partial t}\left[\rho_0 v_n\, \delta(f)\right] - \frac{\bar{\partial}}{\partial x_i}\left[p\, \delta_{ij}\, n_j\, \delta(f)\right] \\ &+ \frac{\bar{\partial}^2}{\partial x_i \partial x_j}\left[T_{ij}\, H(f)\right] \end{aligned} \tag{2.11}$$

where ρ_0 is the density of the undisturbed medium, $v_n = v_i\, n_i$, with v_i denoting the body velocity components and n_i the components of outward unit vector orthogonal to the body surface $f(\mathbf{x}, t) = 0$, while the overbars denote generalized derivatives. In addition, $H(f)$ represents the Heaviside step function. The presence of δ and H functions denotes the different nature of right-side terms: two terms associated with discontinuity due to the presence of the body surface $f(\mathbf{x}, t) = 0$ in the field, and a final term including all other sources.

A computationally efficient and widely-used method to determine the acoustic field from Eq. (2.11) is the application of a boundary integral formulation approach, based on the introduction of the Green function of the differential operator. Among the boundary integral solutions of Eq. (2.11) available in the literature, particularly suited for the problems examined here is the well-known Formulation 1A, developed by Farassat [82, 83]. The resultant aeroacoustic field is found as superposition of three separate integral contributions known as thickness noise, loading noise and quadrupole noise, each related to a specific mechanism of acoustic disturbance generation. For aeroacoustic analysis of helicopter rotor, the thickness (surface integral) term depends on the blade geometry and the kinematics of the problem, the loading (surface integral) term is related to the blade airloads, whereas the quadrupole (field integral) contribution mainly accounts for nonlinear effects from the flow velocity field around the blade. The quadrupole term, that is the most difficult to evaluate, is negligible when the blade rotational velocity is far from the transonic/supersonic range, and this condition is valid for the applications presented in this thesis.

From Formulation 1A, thickness and loading noises (respectively identified as p'_T and p'_L) are given by the following integrals evaluated over the

actual blade surface, S_B, [82, 83]

$$
\begin{aligned}
4\pi p'_T(\mathbf{x},t) &= \int_{S_B} \left[\frac{\rho_0 \dot{v}_n}{r|1-M_r|^2}\right]_\tau dS(\mathbf{y}) \qquad (2.12)\\
&+ \int_{S_B} \left[\frac{\rho_0 v_n \left(r\dot{M}_i\hat{r}_i + c_0 M_r - c_0 M^2\right)}{r^2|1-M_r|^3}\right]_\tau dS(\mathbf{y})\\
4\pi p'_L(\mathbf{x},t) &= \frac{1}{c_0}\int_{S_B} \left[\frac{\dot{p}\, n_i\hat{r}_i + p\,\dot{n}_i\hat{r}_i}{r|1-M_r|^2}\right]_\tau dS(\mathbf{y}) \qquad (2.13)\\
&+ \int_{S_B} \left[\frac{p\, n_i\hat{r}_i - p\, M_n}{r^2|1-M_r|^2}\right]_\tau dS(\mathbf{y})\\
&+ \frac{1}{c_0}\int_{S_B} \left[\frac{p\, n_i\hat{r}_i}{r^2|1-M_r|^3}\left(r\dot{M}_i\hat{r}_i + c_0 M_r - c_0 M^2\right)\right]_\tau dS(\mathbf{y})
\end{aligned}
$$

with $\mathbf{r}$ denoting the distance between $\mathbf{x}$ and $\mathbf{y}$, $r = |\mathbf{r}|$, and $\hat{r}_i = r_i/r$ (where r_i represent the components of the distance vector). In addition, $M_i = v_i/c_0$ are the components of the local Mach vector of module M, $M_r = M_i\,\hat{r}_i$ and $M_n = M_i\, n_i$. The notation $[...]_\tau$ indicates that the quantities inside the brackets are evaluated at the emission time, τ, *i.e.*, the time at which the signal arriving in $\mathbf{x}$ at time t started from $\mathbf{y} \in S_B$ [82, 83].

For the problems faced in this work, surface S_B represents the blades surfaces, and the integrals appearing in Eqs. (2.12) and (2.13) are evaluated by a discretization of the blade surfaces into quadrilateral panels, assuming that within panels the integrand functions that multiply the kernel terms are uniform and equal to their values at the centroids (zero-th order formulation).

In problems dealing with weakly loaded rotors, thickness and loading noise are comparable. However, when strongly loaded rotors are examined, the thickness noise contribution tends to be negligible and the acoustic disturbance is dominated by the loading noise. Rotors in BVI conditions fall within this category of acoustic phenomena, with the terms including pressure time derivatives strictly related to BVI effects. Hence, accurate evaluation of blade loads is of paramount importance for rotorcraft acoustic performance assessment and identification of reliable noise control law. This relies on determination of rotor pressure distribution during the blade revolution, considering that high time and spatial resolutions are needed to accurately capture impulsive phenomena like BVIs. This means an intense computational effort required for noise prediction and for identification and numerical application of active control laws.

2.4 Computationally efficient aeroelastic and aeroacoustic rotor simulations

This section and the following Chapter 3 are the core of this thesis, along with the applications presented in Chapter 4. In the previous sections, formulations used to simulate rotor aeroelastic and aeroacoustic behaviour have been described, underlining the high computational demand of these models due to the high level of accuracy required for solutions. Numerical effort becomes extremely intense when these tools are used integrated in optimization algorithms or for active control synthesis procedures, which often require a large number of calculations (as shown in the following chapter).

In this Chapter, models able to speed up single simulations, preserving the required level of accuracy, are described. In the following Chapter 3 the attention is instead focused on particular approaches efficiently exploiting aeroelastic and aeroacoustic models for the specific considered applications.

As stated in Section 2.1, in the aeroelastic solver used, distributed aerodynamic loads are evaluated by span-wise integration of loads given by a sectional theory. In the same solver, three dimensional interaction effects are taken into account by a wake inflow correction, which changes the effective sectional angle of attack (AoA).

This concept, of modelling rotor blades through an assembly of aerodynamically independent airfoil elements, is known as blade element theory (BET) [3,59,84,85]. It is widely used, with different levels of approximation, for rotor aerodynamic analysis, especially in the early stages of helicopter design. The theory is based on the assumption that each blade section can be considered as a quasi-bi-dimensional airfoil, without mutual influence between adjacent elements. The overall blade loads are then obtained through spanwise integration of all sectional contributions. Three-dimensional effects, like tip loss or non uniform inflows over the rotor disk, can be accounted through proper modification of the AoA (and thus, the section-air relative velocity) of each blade element. Considering, for example, the blade element in Figure 2.4 at a radius r from the axis of rotation: although the geometric pitch angle of the blade element relative to the plane of rotation is θ (with vertical speed V_c), the local induced velocity v_i alters the effective AoA in

$$\phi = tan^{-1}\left(\frac{V_c + v_i}{\Omega r}\right)$$

Unless using simple analytical model for inflow distribution over the disk (constant or linear inflows), in this way the blade element analysis provides

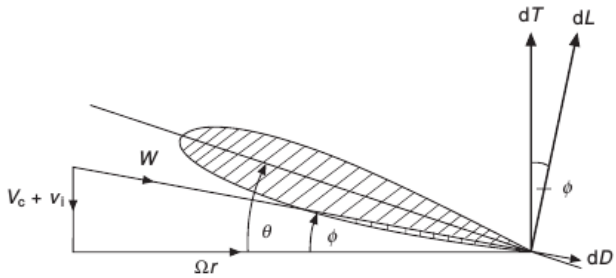

Figure 2.4: Representation of effective AoA due to inflow correction.

quite accurate simulations, capable of taking into account non-uniform wake inflow, as well as some effects of mutual influence from blades or other aircraft components, such as airframe and aerodynamic surfaces.

In the aeroelastic analyses performed in the present work, the quasi-steady approximation of Greenberg theory [60, 61] is used for sectional loads evaluation. Inflow corrections are provided, as body-air relative velocity at the rear aerodynamic centre of blade sections, by a three-dimensional, free-wake aerodynamic solver for unsteady, potential flows. This permits to accurately evaluate deformations of blades undergoing unsteady loads, and to accurately predict blades-wake mutual positions during rotor revolution. The application, at this step, of a more complex sectional formulation results unnecessary, since blades cross sections are assumed to be rigid.

A different approach is instead needed in evaluating sectional loads devoted to aeroacoustic analysis[6]. In this case, the presence of localized, impulsive phenomena, such as BVI occurrences, must be predicted with sufficient accuracy and the Greenberg model results not suitable for this task[7]. This aspect leads to the use of the more complex Küssner-Schwarz formulation [70], able to predict sectional loads from arbitrary chordwise shapes of inflow field, for evaluating blade surface pressure distribution to be used in aeroacoustic

[6]As stated above and schematically represented in Figure 2.1, loads to be used for aeroacoustic prediction can be directly evaluated through the BEM aerodynamic solver. This approach is extremely computationally demanding to be applied in optimization and control synthesis procedures. This justifies, as described below, the use in this work of surrogate inflow models, which are evaluated still using the BEM solver, but only for specific configurations falling within a domain of interest, and before performing the procedures just mentioned (*i.e.*, off-line). Such approach permits to quickly obtain (on-line) aeroacoustic pressures for the desired configuration through analytical sectional models.

[7]Although the capability of Greenberg model in considering impulsive events during blade revolution depends only on time discretization, it is not able to take into account inflow distributions along the airfoil chord more than linear.

analyses.

In the following sections, a surrogate model of wake inflow, used to relieve numerical calculations, and the Küssner-Schwarz theory are briefly presented as approaches able to reduce computational cost of simulations performed, assuring the required level of accuracy.

2.4.1 Surrogate wake inflow models

In the description provided in the Section 2.2, a numerical demanding formulation is introduced as tool for aerodynamic simulation. Indeed, a solver able to accurately predict global behaviour and localized unsteady phenomena of interaction is needed to correctly reproduce the complex aerodynamic field in which helicopter rotors operate. This numerical tool must be also able to simulate free wake evolution, and loads arising from strong interactions occurring between wake and blades, without leading to numerical instabilities. The formulation described in Section 2.2 is able to meet all these requirements, representing in turn the bottleneck in simulation processes, because of the high level of accuracy needed for the solution. This is especially true in optimization and control synthesis procedures, where high number of calculations are usually performed varying values of several parameters involved in the simulated phenomena.

As stated above, the BEM solver participates to the solution providing corrections to the simplified aerodynamic model implemented in aeroelastic code. These corrections consists in contributions to the body-air relative velocity at the rear aerodynamic centre of the blade sections due to wake vorticity. Another result provided by BEM solver is the pressure distribution over blades surfaces evaluated through Eq. (2.9) and used as input for aeroacoustic predictions of noise aerodynamically generated by the helicopter rotor. In particular, the latter result needs to be obtained through finer discretization of blade surface in order to capture localized pressure jumps due to blade-wake interactions.

In applications like those described in this thesis, wake inflow and pressure distributions need to be evaluated in every rotor configuration examined, in case of optimization procedure, and for several values of control variables, in case of controller synthesis process. In these cases, as widely used in multidisciplinary design optimization problems [63, 64], wake inflow surrogate models are proposed as good trade-off between accuracy and computational efficiency. Indeed, these models permit to significantly reduce computational time for simulating the complex aerodynamics involved in rotor operations.

This thanks to approximate inflow models obtained by interpolating[8] inflow database created off-line, *i.e.*, out of optimization or controller synthesis processes, which replace, in the cases examined, the BEM demanding calculations. This approach might also allow models implementation within onboard closed-loop controllers, where availability of off-line inflow database makes affordable the real time evaluations required.

In the following subsections, approaches used to build and use wake inflow database are described referring to the applications presented in this thesis.

Surrogate model aimed at blade optimization

The goal of the optimization procedure presented in this work, and described in Section 3.1 with more details, is pursued by tailoring structural, inertial and aerodynamic properties of rotor blades using a genetic algorithm to identify configurations generating minimum vibrations. In particular, the following design variables are considered: bending and torsional stiffnesses, blade mass per unit length (assumed to be uniformly distributed spanwise), sweep and anhedral angles (see, for instance, Figure 3.2) defined in the 15% long blade tip region. This means that, in the optimization procedure, a huge number of configurations are examined, altering simultaneously the values of the design variables within a defined domain (firstly randomly, then as driven by the algorithm, see Section 3.1) It is clear that, if complete aeroelastic analysis was performed for each configuration considered (which would require achieving convergence between the aeroelastic and aerodynamic BEM solutions), unsustainable time lapse would be required to achieve a worthy result, and great difficulties would be met in properly covering the whole domain considered for the design variables.

In order to avoid this unaffordable numerical effort, a surrogate inflow model has been created for the application and, during the optimization procedure, aeroelastic analyses[9] have been performed getting inflow corrections from the surrogate model. Embracing this approach, the computationally expensive BEM solver is not used during the optimization process, but only for off-line calculations, to obtain wake inflow for a limited number of configurations falling in the domain of definition of the optimization problem.

[8]Depending on the application examined, three interpolation strategies has been considered in the work presented here: feed-forward neural networks, thin-plate splines and linear interpolation.

[9]In the optimization examined in this thesis, evaluation of surrogate inflow model is exclusively performed to be used in aeroelastic solution (for sectional aerodynamic loads prediction), since the procedure is only aimed at reducing vibratory level, without considering aeroacoustic disturbances in the function to be minimized.

The blade configurations chosen to contribute in building the surrogate inflow model differ only for values of sweep and anhedral tip angles. Indeed, a preliminary sensitivity analysis performed has shown that the wake inflow is less affected by mechanical/structural blade properties[10]. Database of wake

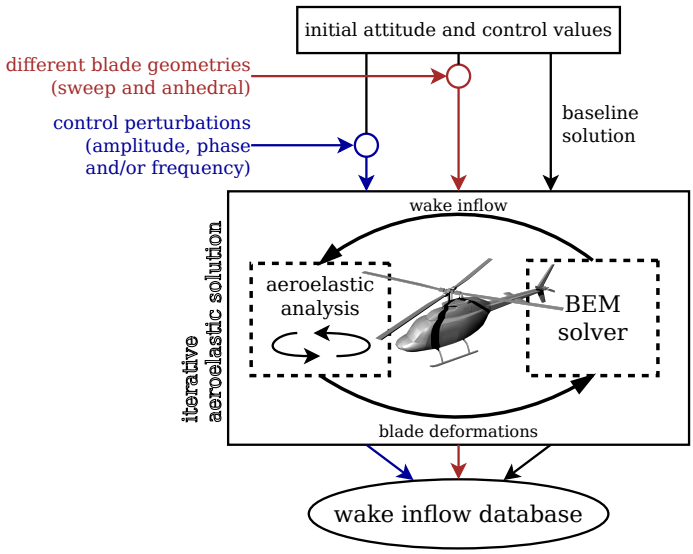

Figure 2.5: Scheme of wake inflow database creation.

inflow is created as shown in Figure 2.5, where the black path represents the analysis performed to obtain baseline solution, whereas the red path is that related with the other blade configurations, characterized by different sweep and anhedral tip angles falling in the domain considered for the optimization (the blue path will be considered in the following, in that concerning with the active control synthesis procedure). As shown in Figure 2.5, trimmed aeroelastic solutions are obtained for baseline (straight) and curved blades using the complete iterative procedure illustrated in Sections 2.1 and 2.2. The wake inflow data relative to each configuration selected are stored, contributing to the database used to quickly obtain sectional aerodynamic corrections during the genetic optimization process.

The way the use of a surrogate inflow model improves the aeroelastic

[10]This is mostly true if elastically deformed blade geometry is not considered in performing aerodynamic calculations through the BEM solver, like in the case examined. A different approach is necessary in creating inflow database for active control of BVI noise: in that case, deformed geometry must be included in aerodynamic analysis because of the crucial role covered by the blade-wake mutual distance (influenced by both the deformation of the blades and the free evolution of the wake) in noise generation.

simulations performed within the optimizer, in terms of computational efficiency, is schematically shown in Figure 2.6. The path shown with dashed

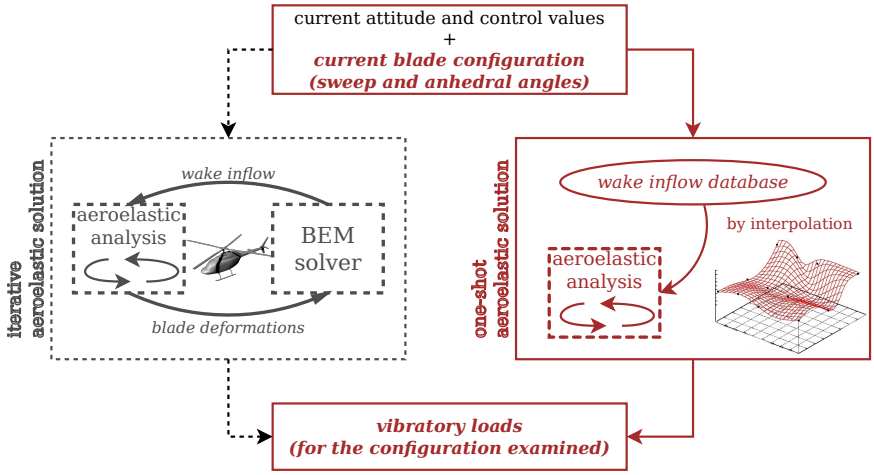

Figure 2.6: Effect of surrogate inflow model on evaluation of rotor vibrations.

lines represents the time consuming iterative process that should be executed for each configuration examined during the optimization. This process, in the applications discussed in this thesis, is instead replaced by the extremely faster process indicated by the path in red: the aeroelastic simulation is not iteratively performed coupled with the BEM solver, but it provides the solution through a single-shot calculation, obtaining the desired inflow correction properly interpolating[11] the samples contained in the database.

Surrogate model aimed at controller synthesis

In general, also for active control synthesis, the availability of numerically efficient simulation tools is extremely useful, due to the high number of simulations that might be required. In the applications presented in this thesis, two kinds of controller are studied: one acting at high frequencies and the other at lower ones, both aimed at reducing noise due to BVI, but pursuing the objective through different approaches, as it will be seen below, in Section 3.2.

[11]For the work presented here, three interpolation strategies are proposed and investigated: feed-forward neural networks, thin-plate splines and linear interpolation.

Despite the two different control strategies, in both approaches the synthesis of driving control law is carried out by means of an optimal, multi-cyclic control algorithm, which may be interpreted as the natural extension of standard optimal LQR control method applied to steady-periodic response of an arbitrary system. Furthermore, in both cases the application of the controller is performed in closed-loop, applying the controlling action in a series of steps, and giving to the control algorithm the possibility to know, in iterative manner, system response at each step of actuation.

As stated before, for this kind of approaches having highly efficient simulation tools is very important. Indeed, synthesis of a controller using the multi-cyclic optimal control technique requires the iterative (on-line) application of a number of control actuations (simulating system response at each iterate) in order to achieve convergence on the best result obtainable in closed-loop, as it will be seen below in Section 3.2.

Proposing some useful tools for alleviating the numerical effort of these operations is among the objectives of this thesis. Akin to what stated for the optimization procedure, the first step is the creation of a surrogate model for wake inflow, following operations schematically shown in Figure 2.5. This time, paths in black (baseline) and in blue must be considered. In particular, the latter represents aeroelastic solutions obtained through open-loop responses to small perturbations of each control variable[12], spanning a suited domain. Also in this case, trimmed aeroelastic solutions are obtained for baseline (uncontrolled) and controlled rotors using the complete iterative procedure illustrated in Sections 2.1 and 2.2. This procedures differs for the two control approaches only for the rotor geometry implemented in the BEM aerodynamic calculations aimed at evaluating inflow velocity induced by wake on blades surface. Indeed, in creating the inflow database for the high-frequency controller synthesis, the BEM solver sees an undeformed rotor geometry beside receiving boundary conditions on the velocity of the blades related to the aeroelastic solution obtained at each iterate (see, Figure 2.1). Instead, in the case of databases for low-frequency controller, the BEM solver also sees the deformed geometry of the blades. This different choice is related to the fact that considering the deformed configuration for the low-frequency control is of paramount importance, in that its action is mainly focused in altering the miss-distance between the wake vortices and the blades (aeroelastically deformed). At the end of the simulations, the wake inflow data relative to each configuration selected are stored, contributing to

[12]Control variables may differ in terms of amplitude, phase and frequency of the control actuation. Further information about domain spanned by control variables used in the applications considered will be provided in the next sections.

the database used to quickly obtain sectional aerodynamic corrections during the control synthesis procedure.

However, as shown in Figure 2.7, for the active control applications examined, the surrogate inflow model is not exploited by aeroelastic solver (as for the optimization aimed at evaluating and reducing vibratory loads transmitted to the hub by the entire rotor), but it is provided to an analytical solver for determination of pressure distribution on the blades surfaces, starting point for predicting the acoustic disturbance related to the configuration analysed (blue path in the figure). An option for evaluating this load

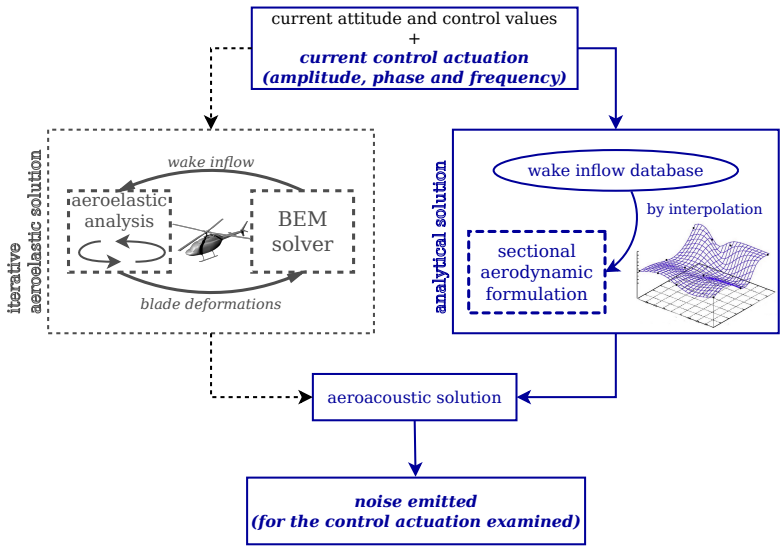

Figure 2.7: Effect of surrogate inflow model on evaluation of noise emitted.

distributions lies in using the BEM solver, as stated above (dashed path in the figure); this, however, as pointed out several times, requires high computational effort. For the sake of numerical efficiency, as leaner alternative, an accurate/efficient, analytical blade element approach is proposed for predicting blade airloads to be provided to the aeroacoustic solver. It relies on the determination of the blade pressure distribution by the Küssner-Schwarz theory [70] (see the following section), coupled with wake inflow from the surrogate model. This formulation has been chosen for its capability to predict sectional loads from arbitrary chordwise shapes of inflow field. Indeed, this characteristic is of paramount importance in BVI conditions, because of the need of capturing also impulsive phenomena along the sectional chord, in order to accurately predict effects of strong interaction between blades and wake. Precisely for these aspects, in case of surrogate model for BVI noise

control applications, inflow database is created collecting values of downwash due to wake vorticity across the entire chord of the airfoils. Otherwise, for the case of surrogate model to be used in the aeroelastic simulations, inflow database is created collecting values of downwash only at the rear aerodynamic centre of the blade sections, as needed for the Greenberg aerodynamic formulation [61] implemented in the aeroelastic solver.

2.4.2 Sectional Küssner-Schwartz formulation

As already stated, the Küssner-Schwartz formulation, starting from the knowledge of chordwise inflow, allows to capture even the presence of phenomena that cause impulsive loads on the blade sections, making it the best solution available in the context of models based on blade element theory. This applies even more if the inflow distribution comes from a solver based on boundary element formulation[13] for three-dimensional, unsteady, potential flows, conceived for free wake analysis of rotors experiencing operations with strong BVI occurrences. Indeed, when a sectional aerodynamic model is applied, evaluation of a realistic blade load distribution requires the inclusion of wake inflow and velocity perturbations from other bodies (if present) to the downwash on the airfoils[14].

In steady-periodic flight, rotor blade surface is subject to periodic inflow with a chordwise distribution that depends on the complexity of the configuration examined. When BVI occurs, local impulsive changes of the wake induced velocity appear and different points along the airfoil chord may experience inflow distributions with different amplitudes and phases. This is clearly shown, in terms of pressure perturbations, in Figure 2.8, where effects of interaction between a two-dimensional airfoil and a parallel vortex are reported for part of the blade revolution [5]. These considerations motivate application of the general Küssner-Schwarz theory for unsteady aerodynamic analysis of the blade airfoils[15], which is briefly presented in the following lines.

For a thin airfoil located between $x = -1$ and $x = +1$, the following

[13]The use of surrogate models increases numerical efficiency of the simulation system, but its level of accuracy must be verified.

[14]Note that, in principle, the wake inflow should take into account effects from trailed vortices and part of shed vortices not already considered in the theoretical model.

[15]A successful application of this aerodynamic solution approach for BVI noise analysis is presented in Ref. [72]

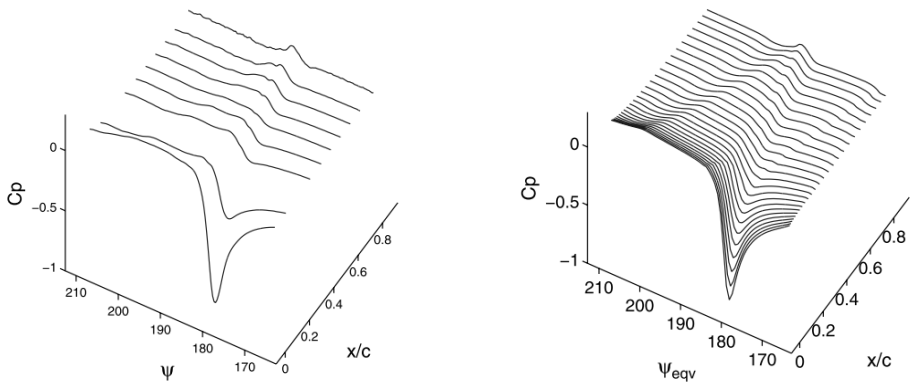

(a) Experimental. (b) CFD results.

Figure 2.8: Pressure perturbation on airfoil surface during revolution [5].

general multi-harmonic distribution of downwash can be considered:

$$w(x,t) = \sum_m f(x,\omega_m)\, e^{i\,[\omega_m\, t - \psi(x,\omega_m)]} \tag{2.14}$$

where $f(x,\omega_m)$ denotes the amplitude of the ω_m-harmonic component of the

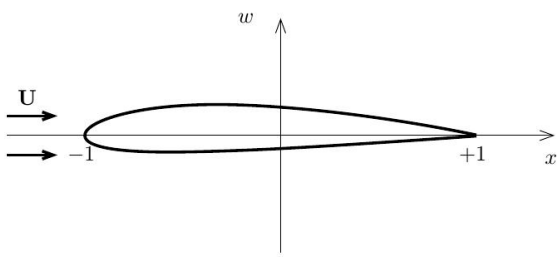

Figure 2.9: Airfoil profile and coordinate system.

downwash, while $\psi(x,\omega_m)$ denotes distribution of the corresponding angular phase[16]. Then, introducing the new variable $\theta \in [0,\pi]$, such that $x = \cos\theta$, and expressing the downwash distribution by the Fourier series

$$w(\theta,t) = \sum_m \left(P_0^m + 2\sum_{n=1}^{\infty} P_n^m \cos n\theta \right) e^{i\,\omega_m\, t} \tag{2.15}$$

[16]Note that, this general unsteady aerodynamics formulation reduces to the Theodorsen theory for downwash given by the combination of chordwise linear distributions of velocity amplitudes with constant phases, while it reduces to the Sears theory for constant downwash amplitudes and linear downwash phases [70].

with

$$P_n^m = \frac{1}{\pi} \int_0^{\pi} f(\theta, \omega_m)\, e^{-i\,\psi(\theta,\omega_m)} \cos n\theta \, d\theta \qquad (n \geq 0) \tag{2.16}$$

the general Küssner-Schwarz theory yields the following distribution of differential pressure, $\Delta p = p_{upper} - p_{lower}$, along the airfoil [70]:

$$\Delta p(\theta, t) = -\rho\, U \sum_m \left(2\, a_0^m \tan\frac{\theta}{2} + 4 \sum_{n=1}^{\infty} a_n^m \, \sin n\theta \right) e^{i\,\omega_m\, t} \tag{2.17}$$

where ρ is the fluid density and U is the airfoil velocity. The coefficients a_n^m appearing in Eq. (2.17) are given by the relations [70]

$$\begin{aligned} a_0^m &= C(k_m)(P_0^m + P_1^m) - P_1^m \\ a_n^m &= P_n^m + \frac{i k_m}{2n}(P_{n-1}^m - P_{n+1}^m) \end{aligned} \tag{2.18}$$

where, for $k_m = \omega_m\, b/U$ denoting the reduced frequency related to the considered section (with b representing the semi-chord length), $C(k)$ is the lift deficiency function introduced by Theodorsen [75] that reads

$$C(k) = \frac{H_1^2(k)}{H_1^2(k) + i\, H_0^2(k)} \tag{2.19}$$

with H_p^2 denoting Henkel functions of second kind of order p.

Dividing the blade into a discrete number of sections and considering downwash distribution given by wake inflow database for a prescribed control input, Eq. (2.17) applied to each blade section yields the corresponding unsteady aerodynamic blade loads to be used in Eqs. (2.12) and (2.13) for the evaluation of the emitted noise. It is clear that the more accurate is the evaluation of the downwash considered in the Küssner-Schwarz theory, the more realistic are the blade loads predicted. It results from combination of blade motion, velocity induced by wake vorticity and aerodynamic interference effects (if present). Of particular importance is the downwash due to wake inflow, especially when BVI occurs[17].

[17] Note that the close shed vorticity generated by the examined section is already taken into account in the airfoil theory, and therefore its contribution to downwash should be neglected.

Chapter 3

Vibration and Noise Reduction

One of the objective of this thesis is the development of effective and numerical efficient methodologies for blade optimization and active control. These procedures are presented here and their effectiveness is investigated in the chapter dedicated to the numerical results, in applications aimed at identifying active and passive techniques for reducing vibrations and BVI noise due to the helicopter main rotor. In particular, a procedure of advanced blade optimization has been investigated as passive approach, in which blade shape and mechanical/structural properties are selected using a genetic optimization algorithm, in order to reduce annoying vibratory loads at different flight conditions. In examining active control approaches, benefits achievable through the active twist rotor (ATR) solution are evaluated, investigating control effectiveness of both high- and low-frequency actuators.

In the following sections, efficient algorithms used for identifying control laws and for obtaining optimized blade configurations are presented.

3.1 Blade optimization

The blade optimization procedure applied in this work is driven by a binary-based genetic algorithm [65, 66] aimed at finding the optimal blade configuration with minimum level of vibratory loads transmitted to the rotor hub. The goal of the optimization procedure is pursued by tailoring the structural, inertial and aerodynamic properties of the rotor blade, under blade aeroelastic stability constraint.

Genetic algorithm (GA) are heuristic programming techniques that mimic the process of natural selection in finding the optimal solution of a given prob-

lem. They belong to the larger class of evolutionary optimization algorithms, inspired by natural evolution, such as inheritance, mutation, selection, and crossover. In the selection process reproduced, each potential candidate solution is called individual and the whole set of individuals is called population. Each individual is identified by a set of properties ordered in a specific sequence (chromosome), which can be mutated and altered. In case of binary-based algorithms, chromosomes are represented by strings of binary digits. This is the most common solution but other encodings are also possible.

The optimization procedure starts from a completely random-generated population[1] (the first generation) and, at each step of the evolution process, individuals are quantitatively evaluated in terms of the corresponding value of the objective function that, coupled with the constraints matching level, results in the individual fitness (please, refer to Figure 3.1 for a better understanding of the present description).

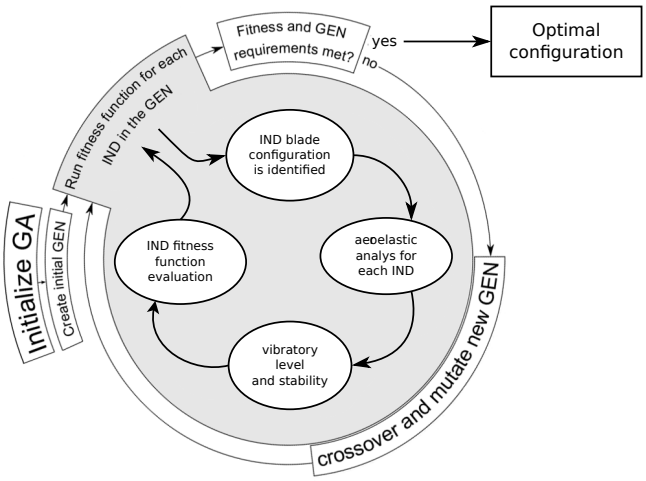

Figure 3.1: Scheme for GA optimization procedure.

In the problem studied, evaluating objective function associated at each individual[2] means to obtain vibratory loads transmitted to the hub through the procedure illustrated in Figure 2.6.

[1]Population size in genetic algorithms is a crucial issue to consider when dealing with specific optimization problems, as it can seriously affect their efficiency. Indeed, a very small population (*i.e.*, composed of few individuals) may lead to an unsatisfactory coverage of the problem domain, as well as to sampling errors [86], while a large population can lead to high computational time, due to the number of evaluations of the objective function larger than necessary. In this work, following Ref. [66], an estimate of the population size based on the variance of the objective functions has been used.

[2]Note that, as already stated several times, operations contained in the grey area

As initially stated, also constraints of aeroelastic nature must be fulfilled by the blade configurations (individuals) examined during the optimization process. Constraints are included through a quadratic extended interior penalty-function approach [87], which enhances the breeding possibility of individuals potentially able to generate good offspring. To form a new generation, the best individuals are selected from the current population on the basis of a fitness measure evaluated from the objective function and constraints fulfilling. Their genome could be modified, recombined and possibly randomly-mutated to create a new generation. For the present analysis, a tournament selection operator is used, based on a stochastic selection of four parents, which are compared one-vs-one in two pairs and the couple of "winners" are selected to be parents of two children with two independent crossover operations.

Once the mate is performed, a binary uniform mutation operation is applied, to avoid premature convergence to local optima, altering one or more binary digit (gene) in the chromosome by flipping it with a given probability. The amount of chromosome variations during the evolutionary process can be controlled through a user-defined mutation probability factor, which decreases during the optimization, for reducing the impact of random mutations as the solution converges to an optimum. In order to prevent possible negative aspects of the evolution process and to enhance solution convergence properties, the best individuals at each step of the optimization process (a given, user-defined, percentage of the population size) are selected to become part of an elite group which stays unchanged in the next generation. The optimization procedure is iterated until either the chromosomes similarity (bit-string affinity) achieves a user-defined value, or the maximum number of iterations is reached.

In this work, optimization process is applied to reduce vibratory hub loads generated by a helicopter rotor in forward flight. Following past works [19, 21, 88], the goal is pursued by tailoring the structural, inertial and aerodynamic properties of the rotor blade. In particular, the following six design variables are considered: blade flap, lead-lag and torsion stiffnesses, mass per unit length (assumed to be uniformly distributed spanwise), sweep and anhedral angles (defined in the 15% long blade tip region). Examples of rotor

of the Figure 3.1 are performed a huge number of times, examining several individuals that are part of each generation at each process iteration, before achieving the optimal solution. This makes using a complete aeroelastic solver for examining each configuration a not affordable approach. Here, the importance of introducing the efficient simulation technique based on surrogate inflow models, presented in Section 2.4.1 and schematically reported in Figure 2.6.

blades with advanced tip geometry characterized by the presence of sweep and anhedral angles are show in Figure 3.2.

(a) AgustaWestland AW109 blade tip.

(b) NHIndustries NH90 blade tip.

Figure 3.2: Examples of advanced blade tips (courtesy of Burkhard Domke).

In order to identify an objective function for measuring vibratory level at the rotor hub, it is helpful notice that a N-bladed rotor transmits to the hub periodic forces and moments of fundamental frequency N/rev, filtering the other harmonic components (a brief description of the hub filtering effect is provided in Appendix B). Hence, as objective function, J, defined in the optimization process, a linear combination of the scalar norm of the N/rev harmonics of hub forces and moments has been chosen[3]:

$$J = \eta_1 \left(\frac{\sqrt{F_x^2 + F_y^2 + F_z^2}}{F_{ref}} \right) + \eta_2 \left(\frac{\sqrt{M_x^2 + M_y^2 + M_z^2}}{M_{ref}} \right) \tag{3.1}$$

where η_i are scalar constants weighting the terms of the linear combination, while F_{ref} and M_{ref} are reference values chosen from the straight reference blade[4].

[3]The x, y and z subscripts refer to a right-handed orthogonal system with origin in the centre of rotor hub. The plane (x, y) is parallel to the undeformed disk, with x-axis pointing backward and y-axis pointing to the right of helicopter. Consequently, the z-axis points upwards.

[4]Alternative methods can be used to define the objective function. A possibility is to embrace the min-max method, in which the function is:

$$J = max\left\{ \frac{F_x}{F_x^{base}}, \frac{F_y}{F_y^{base}}, \frac{F_z}{F_z^{base}}, \frac{M_x}{M_x^{base}}, \frac{M_y}{M_y^{base}}, \frac{M_z}{M_z^{base}} \right\} \tag{3.2}$$

where the superscript *base* refer to baseline values of the loads components. By this approach, the GA tries to minimize all the components simultaneously, achieving a lower maximum decreasing in some values, but showing an almost equal amount of percentage reduction of all the components.

Furthermore, constraints on the equilibrium trim conditions and on the rotor aeroelastic stability for each configuration (individual) examined are introduced. This is necessary because tailoring of inertial, structural and geometrical properties of the rotor blades may have negative effects on the rotor aeroelastic stability (a characteristic of helicopter main rotors is to have low-damped lead-lag bending modes). Moreover, different blade tip shapes alter the aerodynamic loads, thus affecting the helicopter trim condition. Specifically, momentum trim equilibrium conditions are imposed for each configuration contributing to create the inflow surrogate model used in each computation of the objective function, whereas the aeroelastic stability constraint is imposed by setting a minimum acceptable value of the resulting critical damping.

Finally, in order to have a dynamic behaviour of the optimal blade similar to that of the reference one (in terms of eigenfrequencies and blade deflections amplitude), upper and lower bounds on the design variables are imposed, as it will be specified in the Chapter 4, dedicated to the numerical results.

3.2 Definition of the active control approach

In this thesis, IBC techniques are used in order to reduce acoustic disturbance due to BVI phenomena. Using active controls is particularly convenient for this purpose, because BVI noise is relevant in low speed flight, when more power is available to actuators.

Two different IBC approaches are investigated, both based on active twist rotor (ATR) actuations through smart materials. These are simulated by external torques concentrated or distributed along the blade span, since details smart device modelling is beyond the scope of the work.

Purpose of the first controller examined is the direct suppression of impulsive loads due to BVI phenomena by generation of opposite loads concentrated where the interaction occurs, minimizing the onset of negative effects deriving for a more extended control action. An example of impulsive loads experienced by blade sections during parallel blade-vortex interaction is shown in Figure 2.8, whereas in Figure 3.3 acoustic effects on near-field and far-field microphone locations are presented [5], in order to better understand its high-frequency feature.

Cancelling this loads where they are generated become possible only with a controller acting at frequencies significantly higher than those currently studied for the more common approaches in rotorcraft research community, which apply actuation in the range frequency of $2 - 6$/rev. This first proposed control strategy operates in bounded time slots during blade rotation

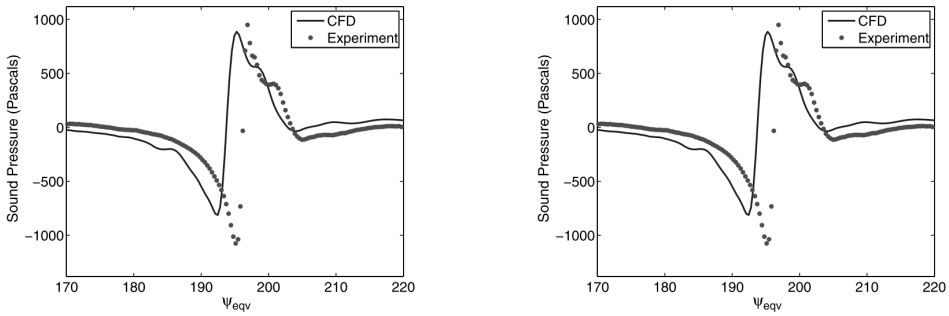

(a) Near-field microphone.

(b) Far-field microphone

Figure 3.3: Acoustic pressure perturbation due to parallel BVI [5].

through small, localized blade torsional moments, letting the system evolve unaffected by controller in the rest of revolution.

The second individual blade controller investigated is a more common low-frequency IBC, which exploits smart materials actions for reducing BVI noise, acting through small 2/rev blade deformations. The attention, in this case, is focused on the BVI generating phenomena and not on the resulting impulsive loads arising, like in the first case. In particular, controller action is aimed at altering miss-distance and interaction angle between blades and tip vortices (see, as a reference, the sketch in Figure 3.4), which are parameters that strongly affect BVI noise. This approach, widely studied in the

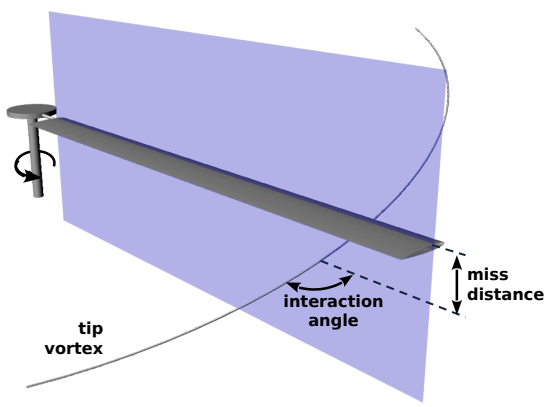

Figure 3.4: Typical parameters characterizing the BVI phenomenon.

literature (see, for example, [11, 31, 32, 39, 40, 74]), represents an interesting

application for the high-performance procedure introduced for the control synthesis, which combines an analytical-numerical formulation for predicting aerodynamic loads, a surrogate model for wake inflow evaluation and an efficient algorithm for control synthesis.

In both of the active control applications described above, the driving control law is determined through an optimal, multi-cyclic control algorithm, based on simulations of rotor behaviour for arbitrary steady flight conditions properly supported by the use of surrogate wake inflow models. This algorithm is described in the following sections, along with specific efficient procedures introduced in this thesis for the applications examined. Numerical models used in simulating aeroelastic and aeroacoustic rotor behaviour were presented in Chapter 2.

3.2.1 Active multi-cyclic optimal control algorithm

The expression "multi-cyclic control" indicates, in general, any control system driven by multi-harmonic actuation[5]; indeed, 1/rev intervention is dedicated, in helicopters, for the trim control. Hence, in addition to the so called HHC, also the IBC and the systems for the active control of vibration in the fuselage (ACSR, active control of structural response) may be included in the category of multi-cyclic controls.

An extensive discussion on the multi-cyclic algorithm is presented in Refs. [30, 37, 42], where also techniques for improving its convergence and robustness qualities are illustrated. In Ref. [30] main characteristics of multi-cyclic controls applied to helicopter rotors are summarized in three items:

i) model of rotor response to the controls[6] is considered linear, quasi-steady and in the frequency domain;
ii) this model can be identified by the least squares method or by the Kalman filter. The identification can be carried out off-line, *i.e.*, before the actuation (invariant control), or it can be performed on-line, recursively during the the control actuation (adaptive control);
iii) the synthesis of the control law consists in minimizing a cost function J, expressed in a quadratic form.

[5]They are sometimes also referred as HHC, creating confusion when this acronym refers to a subset of the multi-cyclic controls, those characterized by action on all the blades simultaneously through actuators installed underneath the non-rotating, swashplate component.

[6]It is clear that, within this framework, talking about helicopter rotor refers to the collection of numerical tools used for modelling its aeroelastic and aeroacoustic behaviour at high level of accuracy. Many of the considerations reported, however, can be directly referred to controller installed on real aircraft.

First of all, the (local) linear approximation of the system response must be highlighted as a crucial step. Indeed, akin to the standard optimal LQR control method (of which the present approach may be interpreted as the natural extension for the application to the control of steady-periodic systems), the minimization of the cost function J is obtained under the constraint of satisfying the governing equation of the system controlled: difficulties related to the simulation of this system clearly require a linearised version of this governing equation. Hence, such constraint is given by a simplified linear (local) relationship between control (input) variables, $\mathbf{u}$, and system response in terms of controlled (output) variables, $\mathbf{z}$.

In case of BVI noise control, the output variables considered in the controller can be the noise harmonics decibels predicted for specific frequencies at microphones properly located (further details about the elements of $\mathbf{z}$ vector for each application considered will be provided in the following sections). Concerning the input vector $\mathbf{u}$ used for the applications investigated, it collects cosine and sine components of torque moments strength applied to the blade through smart materials at the frequencies considered for each application. Of course, these quantities must be evaluated at each time step $t_n = n\Delta t$ in order to leave the system free to evolve till a new steady-state (thus ignoring the behaviour in transient situations). Hence, the linearised relationship between output at time step t_n and the control imposed is:

$$\mathbf{z}_n = \mathbf{z}_{n-1} + \mathbf{T}_{n-1}(\mathbf{u}_n - \mathbf{u}_{n-1}) \tag{3.3}$$

where $\mathbf{T}_{n-1}$ is the (gradient) transfer matrix at $\mathbf{u} = \mathbf{u}_{n-1}$ providing local system response perturbations to variation of control input. It can be identified through least squares method or Kalman filter, as stated in the first paragraph. In the applications objects of this thesis, it is obtained through two different approaches based on least squares method, starting from results of aeroelastic-aeroacoustic rotor coupling. The procedure is outlined in Section 3.2.2.

The sensitivity matrix $\mathbf{T}$ is used to achieve the control law represented by the gain matrices, $\mathbf{G_u}$ and $\mathbf{G_z}$, which provide the optimal control input to be imposed to the system at time step t_n, knowing the system state at t_{n-1}:

$$\mathbf{u}_n^{opt} = \mathbf{G}_u\mathbf{u}_{n-1} + \mathbf{G}_z\mathbf{z}_{n-1} \tag{3.4}$$

These matrices are obtained through the optimal control procedure (widely used in aeronautical field) that consists of minimizing the following cost function

$$J = \mathbf{z}_n^T\mathbf{W}_z\mathbf{z}_n + \mathbf{u}_n^T\mathbf{W}_u\mathbf{u}_n \tag{3.5}$$

where $\mathbf{W_z}$ and $\mathbf{W_u}$ are weighting (generally diagonal) matrices defined so as to get the best compromise between control effectiveness and actuation effort[7].

Combining Eqs. (3.5) and (3.3) permits to eliminated $\mathbf{z_n}$ from the cost function expression, imposing the system to fulfil the constraint represented by Eq. (3.3). Hence, minimizing the cost function J leads to:

$$\mathbf{u}_n^{opt} = \mathbf{D}(\mathbf{T}_{n-1}^T \mathbf{W}_z)\mathbf{z}_{n-1} + \mathbf{D}(\mathbf{T}_{n-1}^T \mathbf{W}_z \mathbf{T}_{n-1})\mathbf{u}_{n-1}$$

that is equivalent to the Eq. (3.4) with

$$\mathbf{D} = (\mathbf{T}_{n-1}^T \mathbf{W}_z \mathbf{T}_{n-1} + \mathbf{W}_u)^{-1}$$

and the gain matrices

$$\begin{aligned} \mathbf{G}_u &= \mathbf{D}(\mathbf{T}_{n-1}^T \mathbf{W}_z \mathbf{T}_{n-1}) \\ \mathbf{G}_z &= \mathbf{D}(\mathbf{T}_{n-1}^T \mathbf{W}_z) \end{aligned}$$

Now Eq. (3.4) has to be used in a recursive way: starting from a given control input and corresponding output, the law of the optimal controller yields an updated control to be applied to the system that, in turn, provides an updated response. This process is repeated until convergence.

Relaxed algorithm

A further improvement to the algorithm for control synthesis is proposed in [37], in which a relaxation factor α_R is used in the evaluation of the control input used at the present time step t_n. It is provided by:

$$\mathbf{u}_n = (1 - \alpha_R)\mathbf{u}_{n-1} + \alpha_R \mathbf{u}_n^{calc}, \quad 0 < \alpha_R < 1$$

where the input $\mathbf{u}_n^{calc}$ is that calculated by Eq. (3.4), whereas the one imposed to the system (on the left-hand side of the equation) is evaluated limiting the deviation from control input of the preceding step, through the relaxation factor α_R. In Ref. [37], it is shown that this procedure, despite slowing down the algorithm convergence rate, increases robustness characteristics of the control algorithm, even in some cases of inaccurate identification of the $\mathbf{T}$ matrix.

[7] In the applications presented in this thesis, elements of weighting matrices are obtained through a genetic optimization algorithm, similar to that presented in Section 3.1. It is exploited to find the optimal set of weights able to obtain the minimum cost function J of the control algorithm varying values of each element of $\mathbf{W_z}$ and $\mathbf{W_u}$ diagonals. It is clear that this approach has been possible only using very efficient numerical procedures in controller synthesis for the extremely high number of simulations required.

3.2.2 Linear system representation: the T matrix

As deduced from the description above, a crucial issue of the control methodology applied is the identification of the $\mathbf{T}$ matrix, which strongly affects both numerical efficiency of control synthesis and effectiveness of controller action. Indeed, the so-called local model[8] [30,37] described in the Eq. (3.3) requires the evaluation, with an adequate level of accuracy, of the gradient matrix, $\mathbf{T}(\mathbf{u})$, at each step of the iterative control process. Recalling that evaluating the gradient matrix means determining sensitivities of noise emitted with respect to variations of each control variable, this would require a large computational effort.

In order to develop fast tools for the control law synthesis, two different efficient approaches are proposed for achieving accurate local model identification in the applications proposed. In the first approach (used in the high-frequency active twist control application) the $\mathbf{T}$ matrix is completely evaluated off-line and its local values are estimated through a least square polynomial approximation similar to what presented in [89]. On the contrary, for the second application (low-frequency control application) only the initial gradient matrix, $\mathbf{T}_0$ is evaluated off-line. Then, the matrix is continuously updated, adding new data collected at each iteration for its determination through the least squares technique.

Local T matrix through polynomial interpolation

In order to obtain efficient determination of the matrix $\mathbf{T}_n = \mathbf{T}(\mathbf{u}_n)$, the following procedure is applied in the first application proposed, concerning the high-frequency active twist control of BVI noise:

i) starting from undeformed rotor blades, a set of output vectors, $\mathbf{z}$, is evaluated as open-loop responses to a set of small blade twist deformations (input vector, $\mathbf{u}$);
ii) from this database, a least squares polynomial approximation of the functions relating each output variable to each input variable is determined;
iii) at each step of the iterative control process, each element of the gradient matrix, $T_{ij} = \partial z_i / \partial u_j$, is analytically derived from the initially

[8] The linearised relationship is named local model because the transfer matrix represents the local system response (this is underlined by the presence of a subscript that indicates the variability of the matrix at each iteration). Also global model, with invariant $\mathbf{T}$ matrix, can be used to synthesize controller laws (see again Refs. [30,37]), but they are more suitable for open-loop controls, because of the low level of robustness of controllers synthesized using invariant sensitivity matrices.

identified polynomial forms.

Thanks to the least squares approximation applied, the application of the optimal local controller become as fast as that of a global controller (*i.e.*, considering a constant gradient matrix), in that it avoids the numerical evaluation of the gradient matrix at each step of the control process.

Local T matrix through adaptive algorithm

In order to develop an efficient tool for the synthesis of the low-frequency control law (the second application investigated), the local model is obtained through the adaptive gradient matrix process. This consists in starting with the gradient matrix, $\mathbf{T}_0$, related to the initial, uncontrolled configuration, and evaluated through open-loop responses to small perturbations of each control variable. Then, following an adaptive control matrix approach similar to that presented in Refs. [11,30,42], matrix $\mathbf{T}$ is updated in order to make it closer to local gradient required by Eq. (3.3), as the iterative process evolves. Specifically, at the n-th iterative step, it consists in firstly collecting applied control variables perturbations, $\Delta\mathbf{u}_k = \mathbf{u}_k - \mathbf{u}_{k-1}$, and measured/calculated output variable perturbations, $\Delta\mathbf{z}_k = \mathbf{z}_k - \mathbf{z}_{k-1}$, at $k \leq n$, into matrices

$$\Delta\mathbf{Z}_n = [\Delta\mathbf{z}_1 \;\; \cdots \;\; \Delta\mathbf{z}_n], \qquad \Delta\mathbf{U}_n = [\Delta\mathbf{u}_1 \;\; \cdots \;\; \Delta\mathbf{u}_n] \tag{3.6}$$

then defining the gradient matrix appearing in Eq. (3.3) as such that

$$\Delta\mathbf{Z}_n = \mathbf{T}_n \, \Delta\mathbf{U}_n \tag{3.7}$$

and finally estimating it through the following matrix pseudo-inversion[9]

$$\mathbf{T}_n = \Delta\mathbf{Z}_n \, \Delta\mathbf{U}_n^T \, (\Delta\mathbf{U}_n \Delta\mathbf{U}_n^T)^{-1} \tag{3.8}$$

In this approach, the linear representation of the controlled system is continuously updated during the iterative procedure, making matrix $\mathbf{T}$ progressively closer to the correct local value of local gradient, as convergence is approached [30, 37].

3.2.3 Computationally efficient approaches for ATR control

Although less computationally expensive than the evaluation of gradient matrix by local sensitivities to all control variables, the approaches presented so

[9] As further improvement in numerical efficiency, in Refs. [30, 37], also a recursive algorithm is proposed for evaluating the n-th gradient matrix, in order to avoid matrix inversion at each control iteration.

far could still require evaluation of a high number of aeroacoustic/aeroelastic responses, depending on the rate of convergence of the iterative control process. Thus, to assure high computational performance of control synthesis in any case, efficient rotor noise prediction tools, like that presented in Chapter 2, are used for control synthesis purposes[10]. Numerical efficiency achieved in the process has allowed the use of a genetic algorithm, which requires large number of simulations, for finding optimal sets of weights for the $\mathbf{W}_z$ and $\mathbf{W}_u$ matrices in Eq. (3.5).

In the following sub-sections, the complete procedures used for the synthesis and application of the active control approaches investigated are summarized, showing how all the tools presented are combined in order to obtain accurate and efficient algorithms useful in closed-loop control applications.

As already stated, both the proposed controllers relies on multi-harmonic blade twist deformations to reduce, as much as possible, rotor BVI noise. However, their synthesis and application have specific features that will be discussed in the next sections.

Algorithm for high-frequencies control

The first proposed control strategy relies on high-frequency actuations to generate loads aimed at direct suppression/alleviation of those due to BVI. It operates in bounded time slots during blade rotation through small, localized blade torsional moments. These are determined by a simplified inverse, aeroelastic problem (see Section 2.1.2), after that a closed-loop, multi-cyclic, optimal control algorithm has provided the desired optimal twist deformation to be applied to the blades (see Figure 3.5 for a schematic representation of the controller action).

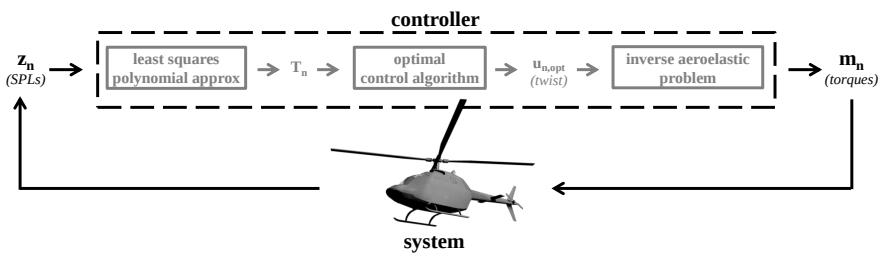

Figure 3.5: High-frequency ATR controller block.

[10]It is worth noting that, its application would mitigate also the computational cost of the local gradient matrix approach based on control variable sensitivity evaluation, starting from an initial determination of the wake inflow database.

For the application presented here, the control action is focused within a time interval during the retreating blade motion[11] defined through application of the Hann windowing. The control variables, $\mathbf{u}$, are defined as some specific harmonics of the blade torsion deformation in the windowed period (torsion harmonics considered are discussed in the section concerning the numerical results). Furthermore, the output variables, $\mathbf{z}$, considered in the controller are noise harmonics decibels predicted at a microphone suitably located. Specifically, the microphone is positioned at the rear edge of the left skid of the helicopter, that is just below the retreating side region of the disk rotor affected by strong BVI, where the controller is actuated. Akin to the approach followed in previous works on this subject [11, 42], the noise harmonics considered in the output vector, $\mathbf{z}$, are those between the 6th and the 17th blade passage frequency[12] (bpf), that are representative of the BVI contribution to the noise. Note that, differently to present analysis, in Ref. [11] the feedback microphone is located on the right skid, since that controller action is mainly focused on advancing side BVI. Relationship between input and output variables is determined, in the present case, through the polynomial approximation described above.

In the control procedure, once the matrix $\mathbf{T}$ is evaluated, the desired blade torsion deformation (limited to the selected window) are iteratively obtained through the multi-cyclic algorithm. At each iteration, the control action is determined in terms of torque moments corresponding to the twist deformations indicated by the optimal control algorithm. To this purpose, for the sake of numerical efficiency (and feasibility of real-time controller), a simplified inverse aeroelastic operator is applied. It is derived from the aeroelastic model presented in Eq. (2.2) which, for a given twist deformation, allows the evaluation of the corresponding torque moments (inverse aeroelastic problem). This completes the control feedback that, starting from noise measurements at the rear edge of the left skid provides ATR actuation moments, during the process synthetically illustrated in the scheme of Figure (3.5), where steps of control process, as well as data exchanged among them

[11] In helicopter configurations in descent flight, several interactions between blades and wake vortices occur in specific regions of both advancing and retreating sides of the rotor disk [10]: the most severe usually occurring in the advancing region for counter-clock rotating rotors. For the application proposed the attention is, instead, focused on the alleviation of the retreating side BVI. This is due, as it will be seen analysing the numerical results, to the fact that retreating side interaction generates effects more clearly bounded with respect to those due to advancing BVI, providing a well-suited test case for proposed control verification.

[12] The rotor blade passage frequency is defined as the number of revolutions the rotor performs per second, multiplied by the number of blades.

are illustrated.

It is worth noting that, an equivalent two-step control process might be defined, instead the three-step in Figure 3.5 by directly considering as control variables, **u**, the harmonics of the blade torque moments actuating the ATR device. The drawback of this approach is that bounding of blade torsion deflections is more difficult to apply in the control synthesis procedure.

Finally, two different uses of the above procedure must be distinguished: when it is applied to synthesize the controller (looking for the weighting matrices assuring the best control performance), and when the control law just synthesized is implemented (and verified) to control a system. In the first case, the procedure described is numerically applied assuming Eq. (3.3) as the equation governing[13] the system evolution in order to identify the control weights and, consequently, the respective gain matrices[14]; then, in the second case, the same procedure is used as a closed-loop control process with responses given by the complete rotor modelling or by application to the real helicopter rotor system[6]. Note that, in the latter case, the time interval between two control steps should be long enough to allow rotor response to reach the steady-periodic state corresponding to the updated control inputs [11].

Algorithm for low-frequencies control

The objective of the second control application proposed is to develop a low frequency noise controller that affects the miss distance between blade and wake vortices, decreasing the strength of BVI phenomena.

The driving control law is derived, as already illustrated, by a closed-loop, multi-cyclic, optimal algorithm, under assumption of linear relationship between control (input) variables, **u**, and (output) monitored variables, **z**, representing the phenomenon to be controlled. In this case, input variables are directly represented by control actuation torques (obtaining the two-step control procedure shown in Figure 3.6), consisting of spanwise distributed twist moments at 2/rev frequency inducing blade twist and bending that, in turn, affect blade motion and wake vorticity.

Furthermore, the output variables considered are assumed to be the Sound Pressure Levels (SPLs) predicted at some microphones suitably lo-

[13] Using the surrogate inflow model in the synthesis phase could be a valid alternative for predicting system response using the procedure outlined in the Figure 2.7. This approach will be followed for the second control application examined.

[14] This allows to carry out a large number of calculations with limited effort, giving the possibility of a better choice for weight matrices (crucial for obtaining gain matrices) using, for example, genetic algorithms.

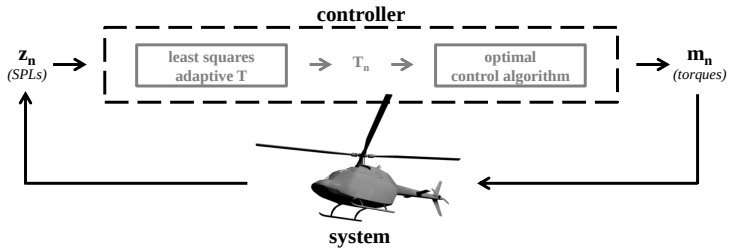

Figure 3.6: Low-frequency ATR controller block.

cated at different points of the helicopter skids. Also in this case, the noise harmonics considered in the output vector, $\mathbf{z}$, are considered in the range representative of the BVI noise contribution (especially between the 6th and the 17th blade passage frequency). Relationship between input and output variables is determined, in this second case, through the adaptive control algorithm presented above.

Finally, differences between control synthesis and control actuation/verification must be highlighted. Also for this second application, control procedure is applied in the synthesis phase assuming fast models as prediction of the system evolution. In particular, system response is predicted following the steps outlined in Figure 2.7 and based on definition of surrogate inflow models. Then, for the control actuation phase, the same control procedure is used as a closed-loop process with responses given by the complete rotor modeling or by application to the real helicopter rotor system[6]. Again, attention should be paid to the time interval between two control steps, which have to be long enough to allow rotor aerodynamics to reach the steady-periodic state corresponding to the updated control inputs [11].

Chapter 4

Numerical Applications

Here, several numerical applications of the tools presented in the previous chapters are proposed. Firstly, the optimization process based on the genetic algorithm described in Section 3.1 is applied to obtain advanced blade configurations generating minimum vibratory hub loads. Single-point and multi-point optimizations are performed and robustness of the optimal configurations in off-design conditions are examined, along with impact of low-vibrating blades on the emitted noise. Then, two different individual blade controls are applied to a rotor model for reducing BVI noise generated in descending flight conditions. The optimal, multi-cyclic control algorithm presented in Section 3.2 is used for obtaining the driving control law in both cases. Results obtained are discussed in terms of noise control performance and onset of negative by-products effects like, for instance, vibratory hub loads and low-frequency noise increases.

4.1 Blade optimization for low vibrating rotor

Here, the optimization process described in Section 3.1 is applied to reduce vibratory hub loads generated by the helicopter four-bladed rotor presented in Appendix C.1. Different level forward flight conditions are examined during the discussion. The objective function to be minimized is a linear combination of the scalar norm of the 4/rev harmonics of hub forces and moments equally weighted, *i.e.*, $\eta_1 = \eta_2 = 0.5$ referring to the Eq. (3.1).

As already stated, the design variables considered are: bending and torsional stiffnesses, blade mass per unit length (assumed to be uniformly distributed spanwise), sweep and anhedral angles defined in the 15% long blade tip region (see Figure 4.1). The largest variations allowed, with respect to the baseline values, for the bending and torsional stiffnesses are selected to

be equal to 30%, the largest acceptable variation of distributed mass is 20%, while the tip sweep angle, Λ_S (positive backwards), and the tip anhedral angle, Λ_A (positive downwards), are constrained to be in the ranges $[-20°, 30°]$ and $[-10°, 15°]$, respectively. Furthermore, constraints on the equilibrium trim conditions[1] and on the rotor aeroelastic stability are introduced for the advancing flights considered. However, noting that hovering flight is usually critical in terms of aeroelastic stability, this constraint has been imposed in hovering, as well.

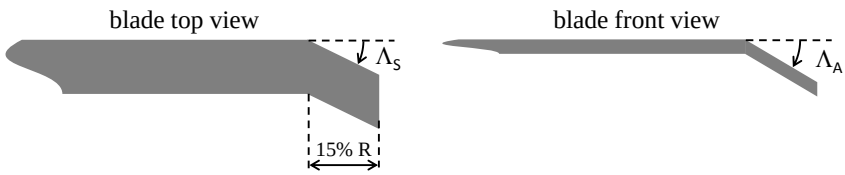

Figure 4.1: Tip sweep and anhedral angles considered.

All the low-vibrating optimal blade configurations presented in the next section have been obtained through the genetic optimization algorithm illustrated in Section 3.1 by considering a population of 60 individuals, each of them identified through a chromosome string of 24 digits (which allows very fine resolution of the design variable range). The optimization process is iterated until a bit-string affinity of 85%, or a maximum number of 50 populations, is reached.

Nine blade configurations, which differ for the values of the sweep and anhedral tip angles[2], have been used to define a coarse surrogate database used in the optimization process.

In the following sub-sections, application strategies and effectiveness of the proposed optimal approach are examined. In particular, attention is focused on the following main issues:

- single-point and multi-point optimization algorithms performance, meaning with these expressions that the rotor blades are optimized considering vibratory loads arising in one or more flight conditions within the objective function expression;

[1] Control settings have been determined as those corresponding to the rotor momentum trim for each flight condition and blade configuration considered.

[2] Indeed, as stated in Section 2.4.1, the wake inflow results weakly affected by mechanical/structural blade properties if elastically deformed geometry is not considered in preforming aerodynamic calculations through the BEM solver.

- effects of different inflow corrections for the aerodynamic sectional model used on reliability of the optimization results;
- robustness of optimal blade design in off-design flight conditions, *i.e.*, flight conditions not considered in the optimization process;
- impact of low-vibration blade design on the emitted noise.

4.1.1 Single-point optimization

First of all, a single-point optimization algorithm has been applied, considering the only design flight condition at advance ratio $\mu = 0.30$.

Before using the surrogate model described in Section 2.4.1, an analytical linear wake inflow model has been considered as first candidate of inflow correction for the sectional aerodynamic Greenberg formulation implemented in the aeroelastic solver. It is a standard non-uniform inflow model based on Drees formula [85,90], yielding a solution extremely efficient from the computational point of view, fully suitable for GA optimizations. It postulates that the inflow profile in forward flight can be approximated with a plane over the disk rotor with deviation from the uniform inflow distribution depending on thrust coefficient, advance ratio and rotor disk angle of attack. Evaluating adequacy of this model in providing inflow corrections in optimization processes aimed at vibrations reduction is the objective of this first analysis.

This first optimization process led to a reduction of about 84% of the objective function, J, repeated below for the 4/rev hub loads harmonics at $\mu = 0.30$

$$J = \frac{1}{2}\left(\frac{\sqrt{F_x^2 + F_y^2 + F_z^2}}{F_{ref}}\right) + \frac{1}{2}\left(\frac{\sqrt{M_x^2 + M_y^2 + M_z^2}}{M_{ref}}\right) \tag{4.1}$$

Such a reduction has been achieved with the identified optimal blade design variables given in Table 4.1. With respect to the baseline values, the optimal design shows an increase of blade mass and bending stiffnesses, a reduction of torsional stiffness, a rearward tip sweep-angle of 19.3° and a downward tip anhedral angle of 4.2°.

Figure 4.2a depicts the 4/rev vibratory hub loads from baseline and optimal rotors evaluated through the aeroelastic model used in the optimization procedure (numerical solver described in Section 2.1 coupled with Drees inflow correction), demonstrating that very good reductions, ranging from 60% to 85%, are achieved.

Then, the optimal blade design has been validated against application of an aerodynamic model more accurate than that used in the optimization process for providing wake inflow correction. To this purpose, the high-fidelity

	Baseline	Single-point opt. (Drees)	Single-point opt. (linear surrogate)
$EI_\eta/m_0\Omega^2R^4$	0.01060	0.01283	0.00857
$EI_\zeta/m_0\Omega^2R^4$	0.03010	0.03514	0.02948
$GJ/m_0\Omega^2R^4$	0.00147	0.00104	0.00113
m/m_0	1.0	1.053	1.188
$\Lambda_A[deg]$	0.0	4.24	-4.4
$\Lambda_S[deg]$	0.0	19.29	23.7

Table 4.1: Blade design variables.

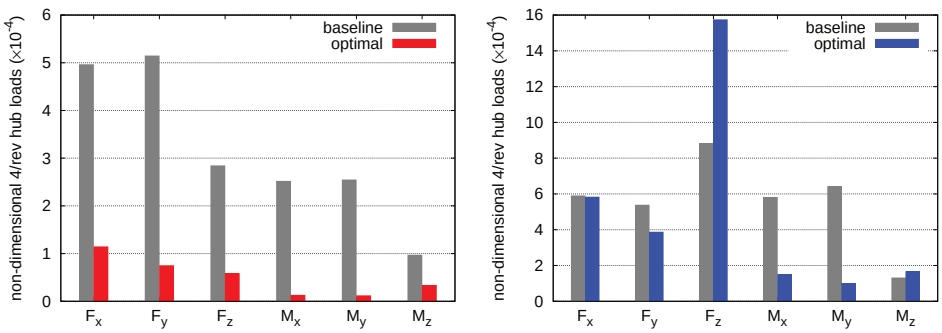

(a) Synthesis (Drees wake inflow). (b) Verification (BEM wake inflow).

Figure 4.2: Vibratory 4/rev hub loads: optimal *vs* baseline configuration at $\mu = 0.30$.

BEM solver mentioned in Section 2.2 has been considered. This analysis confirms the aeroelastic stability of the optimal rotor configuration, but not the significant reduction of the objective function obtained with respect to the baseline configuration. Indeed, aeroelastic solution for the optimal blade configuration using the high-fidelity solver led to only 5% reduction of function J. For detailed view of this loss of results quality, the vibratory hub loads predicted through the high-fidelity aeroelastic model are presented in Figure 4.2b. Comparing it with the Figure 4.2a shows how vibratory loads are sensitive to the aerodynamic model used for their evaluation, with considerably higher values predicted by the high-fidelity aerodynamic model. Furthermore, the out-of-plane component of the hub forces, F_z, is significantly increased from its baseline value, whereas the in-plane force, F_x, and the torque moment, M_z, are weakly affected by the blade re-design. These results show that the sensitivity of the vibratory loads to the design vari-

ables as predicted by the two inflow models are very different (for some load components, even opposite), thus suggesting the need of using results of the more accurate aerodynamic model in rotor aeroelastic optimization process. These results are the natural consequence of using a linear inflow model as the Drees one. Indeed, although allowing to predict the overall inflow effect due to the current flight condition with sufficient accuracy for global rotor performance prediction, this model appears not able to capture local phenomena which may play an important role in generating vibratory loads. An example may be represented by loads arising from interaction between blades and trailed tip vortices, generally related to the flight condition or, in addition, to particular blade geometries, which alter blade-wake mutual distance. On the contrary, the surrogate models presented in Section 2.4.1, while still providing approximate inflow evaluations, allow to capture the local effects mentioned above, thus representing a good trade-off between computational speed and level of accuracy required for the analyses.

Consequently, the optimization process has been repeated replacing in the aeroelastic tool the Drees model with the surrogate model of the BEM free-wake inflow defined from nine trimmed aeroelastic solutions obtained for nine blade configurations, which differ for the values of the sweep and anhedral tip angles falling in the domain of definition of the optimization problem. This model is based upon linear interpolation of the inflow database evaluated off-line.

Using this surrogate wake inflow model in the optimization process, the optimal blade variables given in (column 3 of) Table 4.1 have been identified. They show decreased blade mass and bending stiffnesses with respect to the baseline values and an upward tip anhedral angle, instead of the downward one previously obtained using the Drees inflow model. The blade optimal configuration obtained produces a reduction of the objective function, evaluated through the surrogate model, of 74% in the synthesis phase, slightly lower than that previously obtained. However, in this case, validating the optimal design against application of the high-fidelity aeroelastic solver based on the (non-surrogate) BEM free-wake inflow model, confirms the better quality of results. Indeed, the optimal blade has confirmed both a stable aeroelastic behaviour (in advancing and in hovering flight conditions) and a confirmed significant (63%) reduction of the examined objective function. Again, for an insight view of results obtained in synthesis and verification phases, the 4/rev vibratory hub loads from baseline and optimal rotors are shown in Figure 4.3. In this case, results obtained in the synthesis and verification phases are quite similar, also in terms of vibratory loads components (just small discrepancies appear in the prediction of the in-plane force, F_y,

of the out-of-plane force, F_z, and of the torque moment, M_z). This means

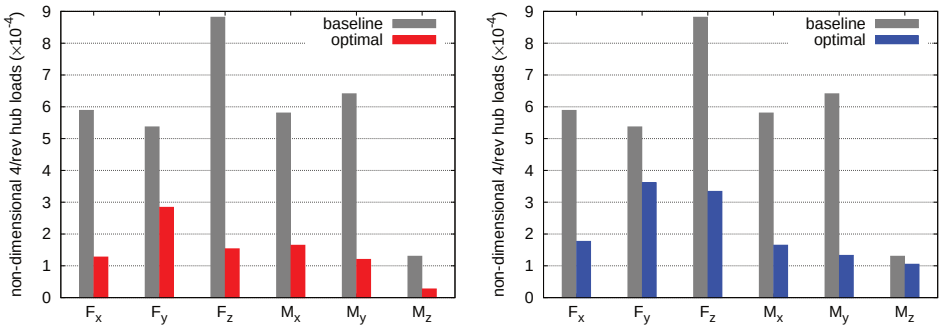

(a) Synthesis (linear surrogate model). (b) Verification (BEM wake inflow).

Figure 4.3: Vibratory 4/rev hub loads: optimal *vs* baseline configuration at $\mu = 0.30$.

that the sensitivity of vibratory loads to the design variables predicted by the linear surrogate wake inflow model is close to that from the high-fidelity aerodynamic model, thus proving that it is well suited for rotor blade optimal design.

Furthermore, the 1/rev and 2/rev root loads in the blade rotating frame[3] are monitored in Figure 4.4. Although not taken into account in the minimization process in that not contributing to the vibratory hub loads, these loads are either practically unaffected or decreased in the examined case, with the exception of the 2/rev out-of-plane shear force that is subject to an increase of about 25%. However, this can be considered as an acceptable minor drawback of the optimal design configuration.

Next, in order to assess the robustness of the optimal design with respect to off-design flight conditions, vibratory hub loads and aeroelastic stability of the optimal rotor configuration have been examined at advance ratio $\mu = 0.15$. Akin to the case with $\mu = 0.30$, the critical eigenvalues are not appreciably affected by the blade re-design, and thus a stable behaviour of the rotor is confirmed. With regard to the vibratory loads, although the objective function results reduced of about 32%, Figure 4.5 shows that the vibratory lateral shear force and torque moment are considerably increased with respect to those at the baseline configuration.

[3]The blade reference frame is a right-handed orthogonal system with x-axis corresponding to the undeformed elastic axis pointing to the blade tip. The y-axis has chordwise direction, pointing to the leading edge, whereas z-axis points upwards.

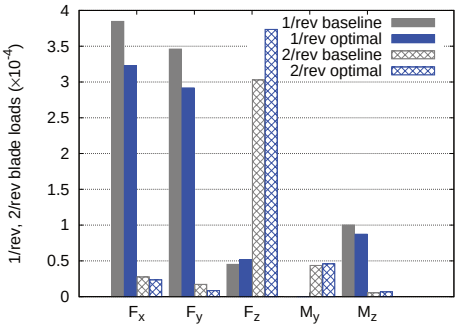

Figure 4.4: Vibratory loads at blade root (BEM non-surrogate model).

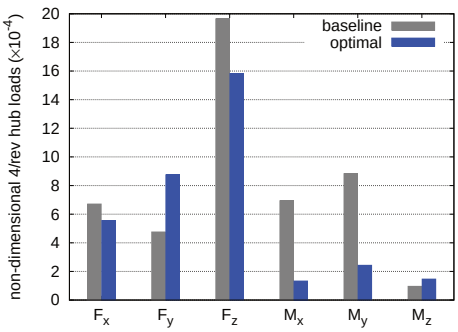

Figure 4.5: Optimized *vs* baseline rotor 4/rev hub loads at $\mu = 0.15$.

In addition, it is worth noting that at $\mu = 0.15$ the vibratory hub loads are higher than those at the $\mu = 0.30$ design flight condition. The reason is explained by Figure 4.6, which depicts the time histories of the blade lift spanwise distribution for the baseline rotor in the design and off-design flight conditions. Indeed, this figure shows a more irregular distribution (in space and time) of the airloads in the off-design flight condition because of the occurrence of strong blade-wake interaction effects, as also revealed in Figure 4.7, depicting an isometric view of the computed wake geometry at the two flight conditions. In particular, Figure 4.7b clearly shows that during the low-speed flight ($\mu = 0.15$), the wake remains close to the rotor disk, thus inducing severe blade-wake impingement, both at the advancing and retreating sides of the rotor.

The final observation that vibratory hub loads may change significantly with changing of flight conditions, thus leading to an unsatisfactory off-design behaviour, suggests to apply a multi-point optimization approach. It consists of taking into account several flight conditions in the optimization function,

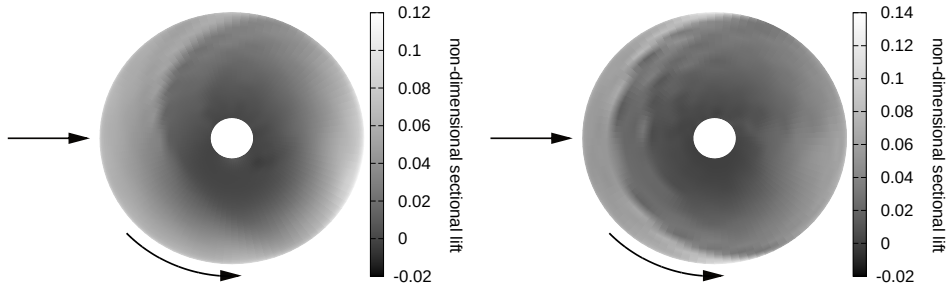

(a) Design flight condition, $\mu = 0.30$. (b) Off-design flight condition, $\mu = 0.15$.

Figure 4.6: Rotor disk distribution of blade sectional lift.

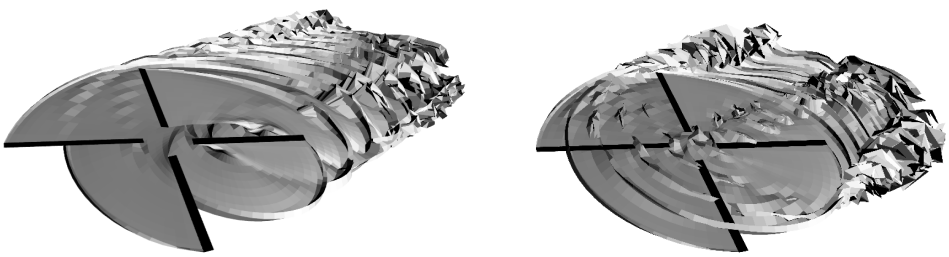

(a) Design flight condition, $\mu = 0.30$. (b) Off-design flight condition, $\mu = 0.15$.

Figure 4.7: View of BEM free-wake geometry.

so as to broaden the range of flight envelope where the optimal blade design might be effective.

4.1.2 Multi-point optimization

For the multi-point optimization purpose the objective function has been re-defined as a combination of vibratory hub loads arising at $\mu = 0.15$ and $\mu = 0.30$. The attempt is to develop a blade design process taking into account aerodynamic effects that characterize both high-speed and low-speed flight conditions. Specifically, the following expression has been considered:

$$J = \sum_{i=1}^{2} \frac{1}{2}\left(\frac{\sqrt{F_x^2 + F_y^2 + F_z^2}}{F_{ref}}\right)_i + \frac{1}{2}\left(\frac{\sqrt{M_x^2 + M_y^2 + M_z^2}}{M_{ref}}\right)_i \tag{4.2}$$

The design variables remain the same of the single-point optimization: blade mass per unit length, the bending and torsional stiffnesses, the sweep and anhedral angles.

The result of the optimization process is a reduction of the objective function, J, of about 64%, with the optimal design variables given in Table 4.2. There is a reduction of bending stiffnesses with respect to the baseline values, whereas torsional stiffness and blade mass per unit length are increased. Furthermore, a rearward tip sweep angle of about 18°, and an upward tip anhedral angle of about 4° have been identified.

	Baseline	**Single-point opt.**	**Multi-point opt.**
$EI_\eta/m_0\Omega^2R^4$	0.01060	0.00857	0.00898
$EI_\zeta/m_0\Omega^2R^4$	0.03010	0.02948	0.02570
$GJ/m_0\Omega^2R^4$	0.00147	0.00113	0.00188
m/m_0	1.0	1.188	1.033
$\Lambda_A[deg]$	0.0	-4.4	-4.1
$\Lambda_S[deg]$	0.0	23.7	18.2

Table 4.2: Blade design variables

The corresponding 4/rev vibratory hub loads are presented in Figure 4.8, where values obtained in the synthesis and verification phases are shown for both the design flight conditions $\mu = 0.15$ and $\mu = 0.30$. Significant

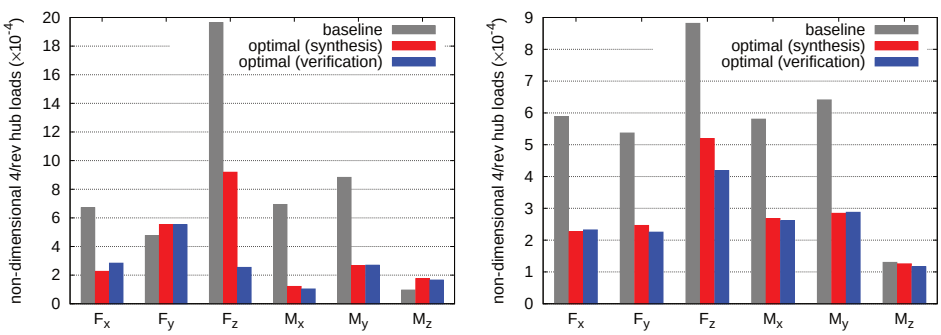

(a) Advance ratio $\mu = 0.15$. (b) Advance ratio $\mu = 0.30$.

Figure 4.8: Vibratory loads from multi-point, linear surrogate wake inflow optimization.

reductions of vibratory loads are evident at both design conditions, although small spillover effects on the in-plane shear force, F_y, and on the torque

moment, M_z, are present at $\mu = 0.15$ (see, Figure 4.8a). However, being these the loads having the smallest amplitude, the overall result may be considered satisfactory.

In addition, these figures present also the verification of the identified optimal blade against the high-fidelity aerodynamic model. Vibratory loads from the linear surrogate inflow model used in the optimal process appear quite similar to those from the more accurate BEM solution model, with the only exception of the out-of-plane shear force at $\mu = 0.15$ in Figure 4.8a, which is thoroughly overestimated by the solver used in the synthesis phase. Anyway, the effect of the changes of the design variables on this load seems to be well captured.

The multi-point optimization with linear surrogate inflow has produced reductions of vibratory loads quite uniformly distributed between the two design flight conditions, although these alleviations, for the flight condition at $\mu = 0.30$, are lower than those obtained by the single-point optimization procedure.

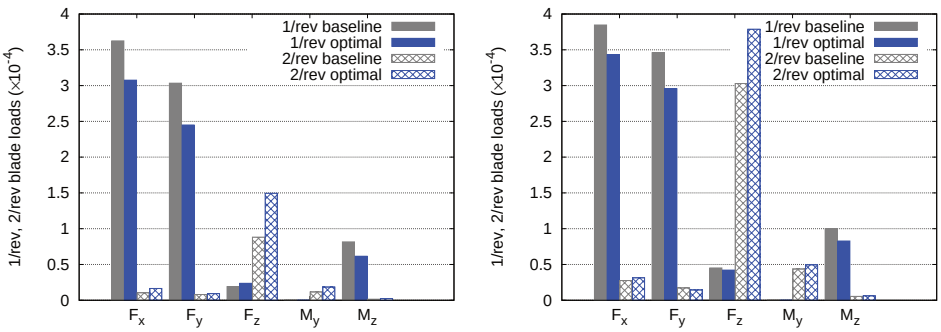

(a) Advance ratio $\mu = 0.15$. (b) Advance ratio $\mu = 0.30$.

Figure 4.9: Vibratory loads at blade root from multi-point optimization.

For the 1/rev and 2/rev rotating blade root loads, conclusions in line with those made in the case of single-point optimization can be drawn. Indeed, Figure 4.9 shows that, although not considered in the objective function, also these loads are reduced, with the only exception of the 2/rev vertical shear force that is subject to some amplification both at $\mu = 0.30$ and $\mu = 0.15$. Again, the amount of the increase is such that it can be considered as an acceptable minor drawback of the optimal blade configuration.

Then, the robustness of the optimal rotor configuration obtained is assessed by simulating rotor behaviour at off-design flight conditions, at advancing ratios $\mu = 0.10$, 0.20, and 0.25. Concerning the aeroelastic stability

requirements for the configuration obtained, a stable response has been observed in two of these three flight conditions, with a slightly unstable eigenvalue appearing at $\mu = 0.10$. However, this does not represent a critical issue, in that the only inclusion of a realistic structural damping in the analysis (not considered here) would avoid the onset of such a weak instability. Concerning the assessment of the off-design vibratory loads generated by the optimal rotor, the following hub loads index is introduced as the sum of the scalar norm of the 4/rev hub forces and moments:

$$\hat{J} = \left(\sqrt{F_x^2 + F_y^2 + F_z^2}\right) + \left(\sqrt{M_x^2 + M_y^2 + M_z^2}\right) \tag{4.3}$$

The values of this index computed through the high-fidelity aerodynamic model at design and off-design flight conditions are depicted in Figure 4.10. These show that, although never increased with respect to those related

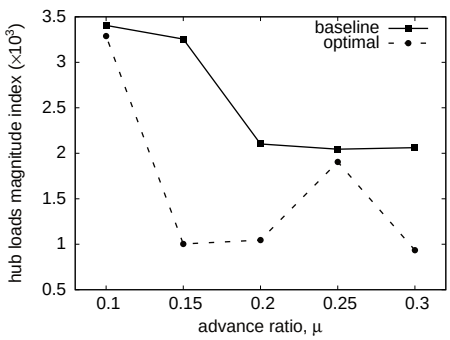

Figure 4.10: Hub loads magnitude index, $\hat{J}$, at different flight conditions.

to the baseline blade, very small reductions are obtained at $\mu = 0.10$ and $\mu = 0.25$ conditions. This is essentially due to spillover effects which typically appear at off-design conditions and that, here, are of particular strength at $\mu = 0.10$ and $\mu = 0.25$. As an example, Figure 4.11 compares the optimal rotor 4/rev vibratory hub loads evaluated at $\mu = 0.25$ with those from the baseline rotor in the same flight condition. Significant increases of in-plane, F_y, and out-of-plane, F_z, shear forces, as well as of torque moment, M_z, are observed in contrast to the reduced corresponding hub loads magnitude index in Figure 4.10.

4.1.3 Effects of surrogate models on optimized configuration

Although the linear surrogate inflow model has proved to be suitable for rotor blade aeroelastic optimization applications, in the multi-point procedure

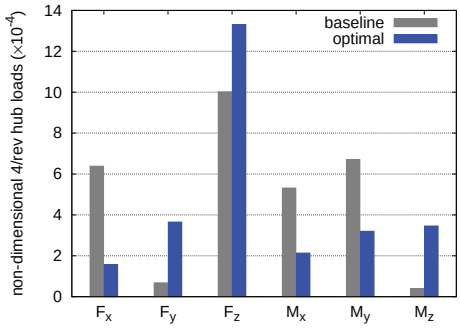

Figure 4.11: Vibratory 4/rev hub loads: optimal *vs* baseline configuration at $\mu = 0.25$.

other surrogate models have been considered, in order to assess the sensitivity of the optimization results to different wake inflow surrogate models. The additional models consist in different approaches, based on thin-plate splines (TPS) and multilayer feed-forward neural networks (NN), to interpolate the same BEM wake inflow database used for obtaining the results presented in previous section. The effectiveness of each surrogate model considered is investigated in terms of reduction of the objective function, J, defined in Eq. (4.2), and comparing the results achieved with those predicted using the high-fidelity BEM solver.

First, for both advance ratios considered in the multi-point optimization, the vibratory loads reduction obtained through a thin-plate spline surrogate model are presented in Figure 4.12. The optimal process has led to a re-

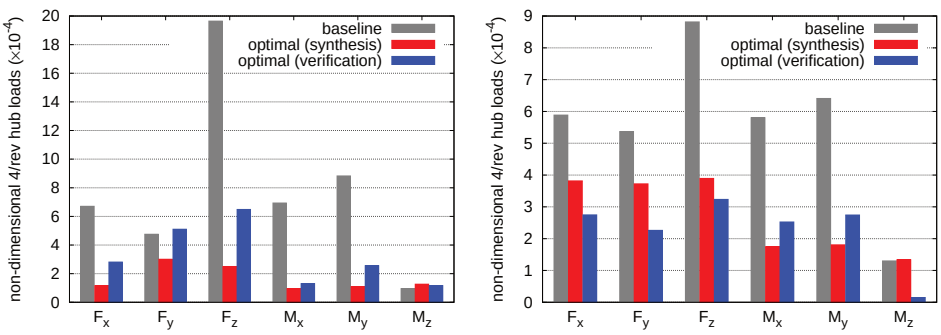

(a) Advance ratio $\mu = 0.15$.

(b) Advance ratio $\mu = 0.30$.

Figure 4.12: Vibratory loads from multi-point, TPS surrogate wake inflow optimization.

duction of the objective function, J, of about 62% with the design variables listed in the third column of Table 4.3, labelled as TPS surrogate. The op-

	Baseline	**LIN**	**TPS**	**NN**	**LIN-NN**
$EI_\eta/m_0\Omega^2R^4$	0.01060	0.00898	0.00856	0.00910	0.00857
$EI_\zeta/m_0\Omega^2R^4$	0.03010	0.02570	0.02940	0.02557	0.02664
$GJ/m_0\Omega^2R^4$	0.00147	0.00188	0.00187	0.00180	0.00188
m/m_0	1.0	1.033	1.164	1.101	1.051
$\Lambda_A[deg]$	0.0	-4.1	-3.9	-4.0	-4.2
$\Lambda_S[deg]$	0.0	18.2	18.7	20.1	17.7

Table 4.3: Blade design variables: multi-point optimization

timal configuration is close to that obtained by using the linear wake inflow model, with a slight reduction of the bending stiffnesses and an increase in torsional stiffness and blade mass. Also in this case, the vibratory loads are quite similar to those estimated by the high-fidelity BEM solver, with the exception of the out-of-plane shear force at $\mu = 0.15$ and the torque moment, M_z, at $\mu = 0.30$.

The further approach for the fast evaluation of the wake inflow in the aeroelastic tool consists in using feed-forward neural networks (NN) for the interpolation of the BEM wake inflow database. Results obtained are presented in Figure 4.13 in terms of vibratory hub loads. Also in this case a reduction of the objective function of about 60% is achieved, with the optimal configuration given in the fourth column of Table 4.3.

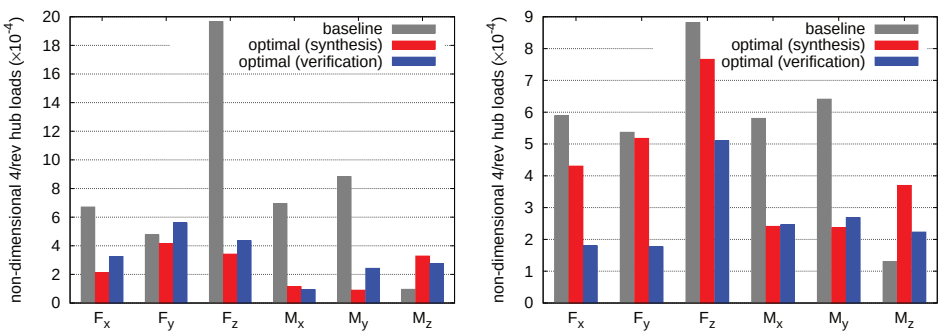

(a) Advance ratio $\mu = 0.15$. (b) Advance ratio $\mu = 0.30$.

Figure 4.13: Vibratory loads from multi-point, NN surrogate wake inflow optimization.

Again, the optimal blade properties are similar to those related with the linear surrogate optimal configuration (LIN), except for the sweep angle that, in this case, is about 20°. The verification with the high fidelity BEM solver has shown a satisfactory level of accuracy in the evaluation of the vibratory hub loads during the synthesis phase, with the better correlation achieved in the slower flight condition. However, some differences are present in the shear forces evaluation at $\mu = 0.30$, with loads overestimated in the synthesis phase.

These results have shown that the linear surrogate model appears more accurate for the wake inflow interpolation at $\mu = 0.30$, whereas the neural networks interpolation is better at $\mu = 0.15$. This is probably due to the fact that at higher advance ratios the wake is far from the rotor disk, and the wake inflow seems to be weakly influenced by the geometrical design variables. On the other hand, at lower advance ratios the wake remains nearby the rotor disk with the rotor operating in a more complex aerodynamic field, thus producing stronger variations in the wake inflow when the geometrical design variables change. In this case, the neural networks-based model appears better in interpolating the strong non linear behaviour. These observations suggest to perform a new optimization analysis, combining the two different approaches: the linear interpolation at $\mu = 0.30$, and the use of neural networks at $\mu = 0.15$.

The reduction achieved for the objective function, J, in this last optimization process is about of 62%, obtained with the design variables listed in the Table 4.3, column LIN-NN. Also in this case, they seem to remain close to the other cases except, again, for the sweep angle which seems to be the variables mainly affected by the new analysis. The performances of this combined optimization, in terms of vibratory hub loads, are depicted in Figure 4.14: the comparison of the loads predicted through the surrogate models with those from the high-fidelity solver reveals that the accuracy of the combined surrogate model is satisfactory, although the level of quality appears similar to the results obtained using the completely LIN surrogate.

It is worth reminding that in all analyses discussed, the satisfaction of the stability constraints is confirmed in the high-fidelity verification.

4.1.4 Assessment of noise emitted by optimized configuration

Noting that design strategies leading to reduced vibratory hub loads are often coupled to more acoustically annoying rotors, the comparison between baseline and optimal rotor configurations is completed by the assessment of the emitted noise. For this purpose, the linear-interpolated surrogate model is considered as candidate representative of the optimal configurations to be

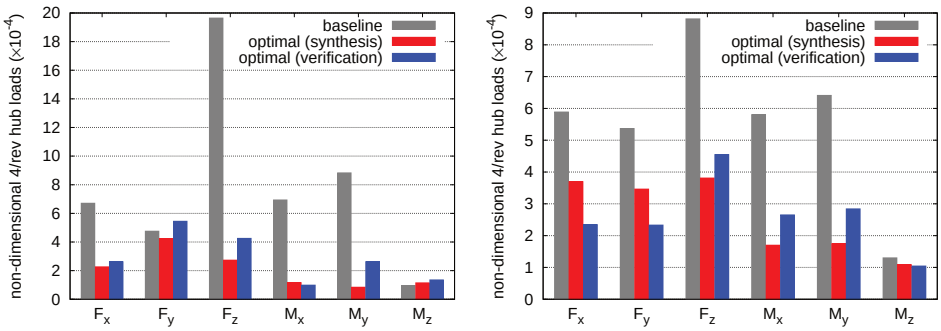

(a) Advance ratio $\mu = 0.15$.

(b) Advance ratio $\mu = 0.30$.

Figure 4.14: Vibratory loads from multi-point, NN surrogate wake inflow optimization.

compared with the baseline, in terms of acoustic annoyance generated. The results are shown over a horizontal plane located 5.5m below the rotor hub in terms of the Overall Sound Pressure Level (OASPL), that is a parameter typically considered to measure the acoustic disturbance. Firstly, Figures 4.15a and 4.15b show the OASPL contour plots related to the baseline and the optimal configuration concerning the flight condition at $\mu = 0.30$.

It can be seen that the sound radiated by the optimal rotor has higher OASPL peaks, along with a more pronounced directional propagation pattern.

Then, the acoustic disturbance associated to the same rotor configurations at slower advance ratio $\mu = 0.15$ are shown in the contour plots of Figure 4.16. In this case, uniformly higher noise levels are produced by the optimal rotor throughout the entire domain considered, with slight modification of the noise radiation pattern.

These results confirm the more acoustically annoying nature of less vibratory rotors, although it is worth highlighting that in high-speed flight the observed impact can be considered lower. This suggests the inclusion of acoustic annoyance measures within the objective function, using multi-objective optimization techniques. A valid alternative could be using advanced low-vibrating blades with integration of active control systems aimed at reducing acoustic annoyance. This is especially suitable for low advance ratio flights, where the noise generated is particularly annoying for the human hear and more power is available to actuators, compared to high speed forward flight.

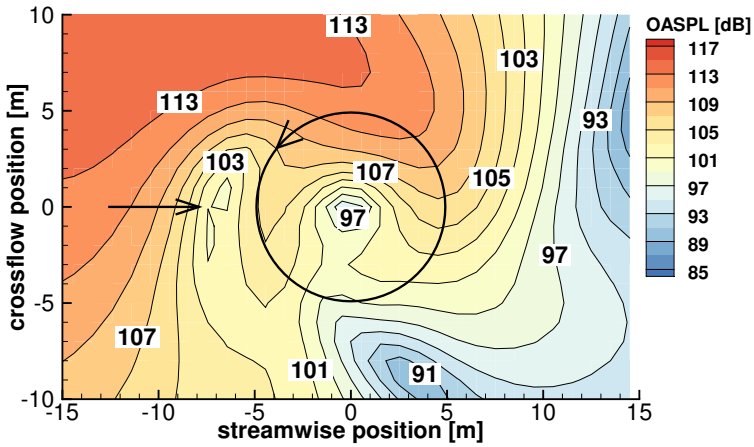

(a) Baseline configuration.

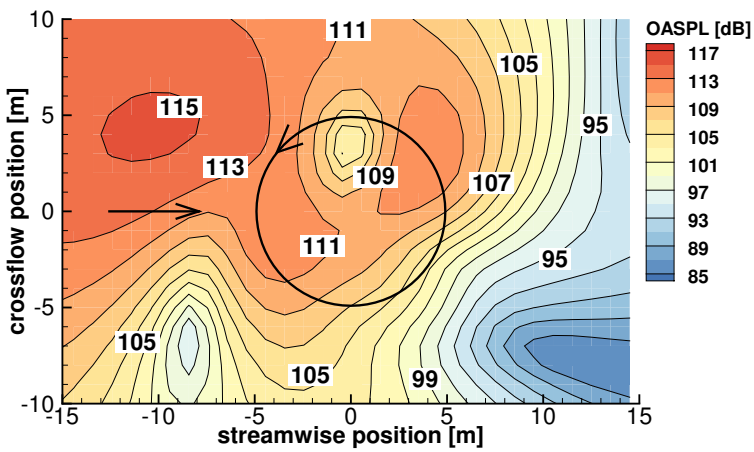

(b) Optimal configuration.

Figure 4.15: OASPL contour plot at $\mu = 0.30$.

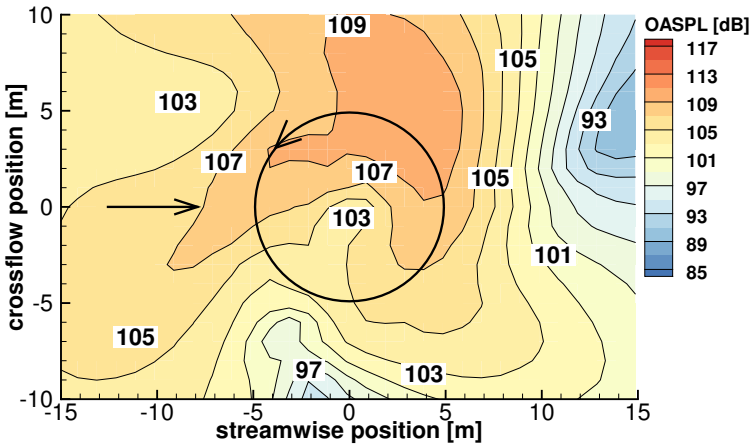

(a) Baseline configuration.

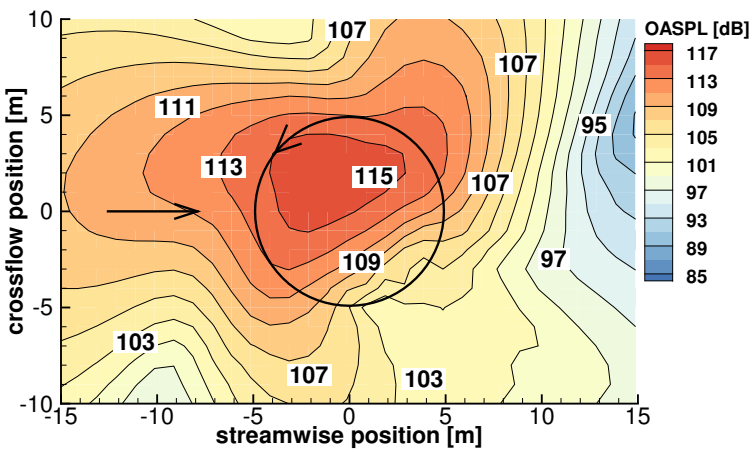

(b) Optimal configuration.

Figure 4.16: OASPL contour plot at $\mu = 0.15$.

4.2 High-frequency active control for BVI noise alleviation

Here, the high-frequency noise control methodology proposed in Section 3.2 is applied in order to reduce BVI contribution to the overall acoustic disturbance generated by the helicopter rotor described in Appendix C.2. The operating condition examined is typically affected by strong BVI events, and consists of a 6° descent flight at advance ratio $\mu = 0.15$, with a resulting shaft angle $\alpha_S = -5.4°$ (*i.e.*, tilted backwards).

In the present section, first, preliminary studies of the baseline (uncontrolled) case are shown, highlighting peculiar characteristics of the rotor operating conditions and allowing the identification of suited control variables. Then, results concerning two numerical applications of the closed-loop noise control approach are presented, differing in the aeroelastic tool providing the rotor response to the controller action. In the first one, rotor blades are assumed to have bending stiffnesses tending to infinity (rigid flapwise and chordwise bending), whereas, in the second case a complete, more realistic, aeroelastic modelling of the rotor blades is considered. From these results it is possible to assess the effectiveness of the control methodology investigated, as well as to estimate the influence of the approximations introduced in the blade aeroelastic modelling applied for control synthesis.

4.2.1 Preliminary analysis

Here, some results concerning the baseline (uncontrolled) descending flight condition considered are firstly presented in order to emphasize the characteristic effects related to the presence of strong BVI.

Figures 4.17 and 4.18 show uncontrolled blade loads and noise field emitted nearby the rotor. Specifically, Figure 4.17 presents time history of high-frequency, BVI-affected content (above 10/rev) of $C_n M^2$ coefficient during one revolution, at blade sections located in the outer blade half. Two main BVI occurrences are identifiable: one at the advancing side (the most severe one), and the other at the retreating side (in agreement with several experimental evidences reported in literature on this subject, [10, 32]).

Figure 4.18 shows contour plot of predicted uncontrolled noise emitted by the rotor, in terms of BVISPL (BVI-Sound Pressure Level) on a horizontal plane located $2.3m$ below the rotor hub, similarly to the analysis presented in Ref. [11] and other works on the same subject. This acoustic parameter, widely used in the following discussion, represents the high-frequency overall sound pressure level associated to noise spectrum between the 6th and the

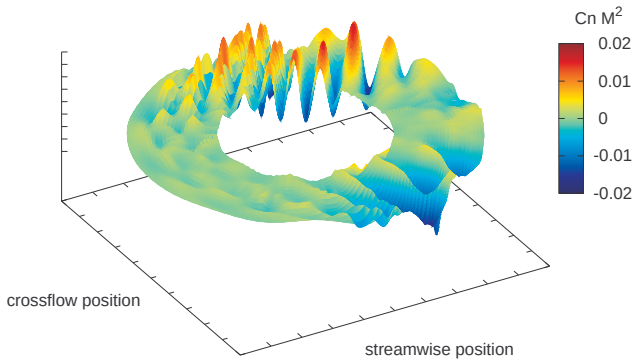

Figure 4.17: $C_n M^2$ high-frequency content, for $0.5 \leq r/R \leq 1$.

40th blade passage frequency (bpf), that is representative of the main BVI contribution to noise. Akin to load distribution, effects due to the main BVI events occurring in the advancing and retreating sides are clearly visible in the acoustic field, as well.

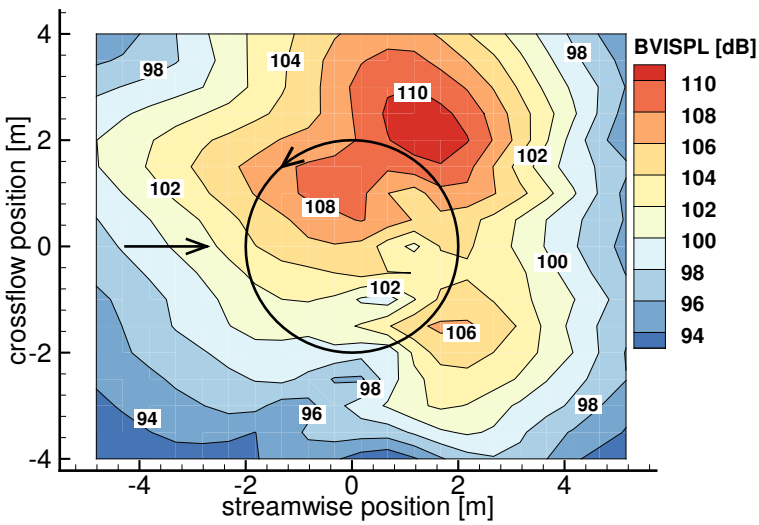

Figure 4.18: Uncontrolled rotor BVISPL.

Next, after a brief introduction of the baseline configuration, a further preliminary investigation is presented in order to identify sets of variables,

u and **z**, suitable for the control process. Since the purpose of this work is the assessment of the ATR ability to alleviate BVI noise through control of blades high-frequency aeroelastic behaviour, a more detailed analysis of the blade sectional loads is useful to derive guidelines for the definition of the most appropriate actuation process. In this regard, Figure 4.19 presents the time history[4] of the high-frequency content of the C_nM^2 coefficient at a specific cross section located at $r = 0.87R$ (the frequency content ≥ 7/rev has been selected, in that strongly affected by BVI events). As expected, also this figure shows two different blade-vortex interaction occurrences: the most severe in the advancing region, the other appearing in the retreating side.

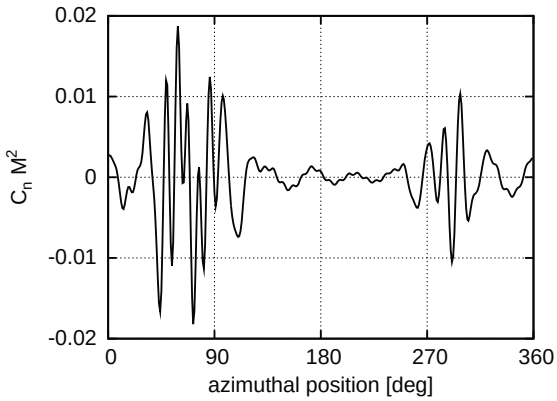

Figure 4.19: Time history of C_nM^2 high-frequency content (≥ 7/rev), at $r/R = 0.87$.

Hereafter, this high-frequency ATR control application will be focused on the alleviation of the retreating side BVI occurrence. Indeed, it generates effects that are more clearly bounded with respect to those due to advancing BVI, and hence provides a well-suited test case for proposed control verification. Of course, the approach adopted, if effective in reducing BVI noise related to retreating side occurrences, can be extended to advancing side control.

The Hann windowing function[5] is applied to the high-frequency content

[4]The zero position for the azimuth ψ is identified with the blade observed is positioned backwards.

[5]The Hann function is one of the window functions usually applied in digital signal processing in order to select a subset of a signal when multiplied for the signal function (or samples). Indeed, the main characteristic of window functions is being zero-valued outside a chosen interval. A further example is the rectangular window, which has a constant value

of Figure 4.19, in order to highlight the retreating side BVI effects. Figure 4.20a depicts the signal extracted in the azimuth range $\psi_{ret} = [260°, 320°]$, while Figure 4.20b shows its frequency content in terms of harmonics amplitudes related to the considered windowing period. The dominant BVI signal harmonics are the 4th and 5th in the window considered, respectively representing the 24/rev and the 30/rev frequencies (window length is 1/6 of the revolution).

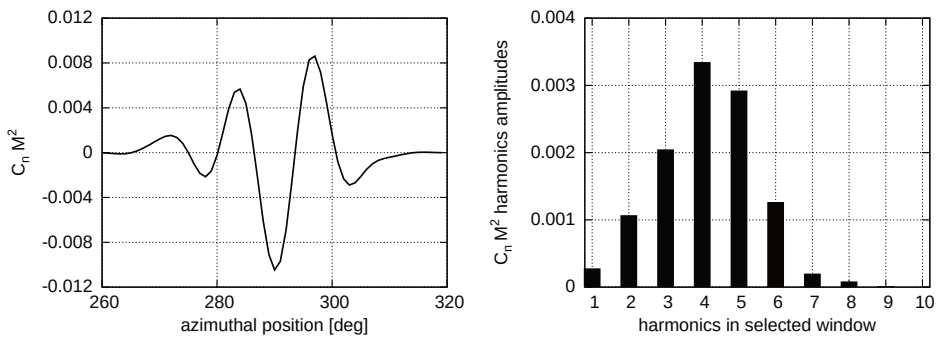

(a) Time history. (b) Spectrum.

Figure 4.20: Windowed $C_n M^2$ high-frequency content.

Considering this contribution, the sine and cosine components of the 4th and 5th harmonics within the same azimuthal window, of the first two blade torsional Lagrangian degrees of freedom, ϕ^I, ϕ^{II}, are assumed as control inputs, $\mathbf{u}$, *i.e.*,

$$\mathbf{u} = \{\phi^I_{4c}, \phi^I_{4s}, \phi^{II}_{4c}, \phi^{II}_{4s}, \phi^I_{5c}, \phi^I_{5s}, \phi^{II}_{5c}, \phi^{II}_{5s}\} \tag{4.4}$$

As mentioned above, the ATR actuation is related to these control inputs through the linearised aeroelastic system in Eq. (2.2), which yields the torque moment to be applied to the blade in order to get the twist deformations identified by the optimal control algorithm. In this work, ATR actuation consists of two concentrated torques located at $r_1 = 0.75R$ and $r_2 = 0.90R$, through which it is possible to control the first two blade torsional modes (indeed, their nodes are far from torque locations).

inside the selected interval and zero elsewhere.
In the case examined the Hann function has the expression

$$w_H(\psi) = \frac{1}{2}\left[1 - \cos\left(2\pi \frac{\psi - \psi_{min}}{\psi_{max} - \psi_{min}}\right)\right]$$

for $\psi \in [\psi_{min}, psi_{max}]$ and it is zero elsewhere.

Furthermore, SPLs of the noise signature evaluated/measured at the rear edge of the left skid of the helicopter have been selected as output variables, **z**. Specifically, these are the SPLs of the noise harmonics between the 6th and 17th blade passage frequency, which are strongly affected by BVI. Position of the monitoring microphone has been chosen to be approximately underneath the rotor disk retreating side (where the controller is actuated) of an equivalent real helicopter, as it is shown in Figure 4.21.

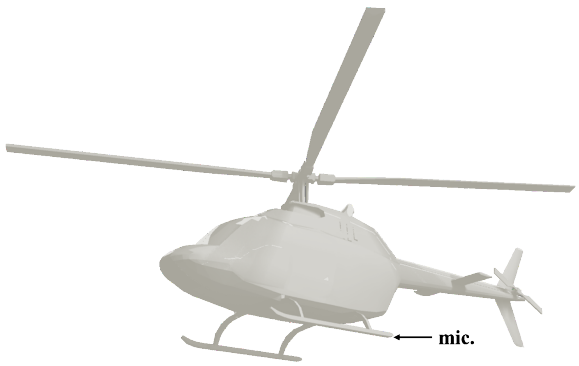

Figure 4.21: Location of on-board microphone.

4.2.2 Noise control with only-torsion rotor response

As first application of the efficient algorithm proposed for high-frequency ATR actuation, the closed-loop control is applied to alleviate the noise emitted by the rotor assumed to be composed of blades undergoing only-torsion deformations (*i.e.*, governed by Eq. (2.2)), as for the evaluation of the actuation torque moments. The choice is justified by the wish to provide information about the nominal performance of the controller synthesized, while the effect of a more realistic rotor aeroelastic response to the ATR actuation will be discussed later. Of course, in this first application, results obtained with controller action will be compared with an appropriate (uncontrolled) baseline condition, in which the blade model used to obtain the trimmed aeroelastic solution is that allowing only torsional deformations.

Figure 4.22 shows uncontrolled (baseline) and controlled high-frequency content (> 7/rev) of coefficient $C_n M^2$ evaluated at the blade cross section $r = 0.87R$ within the same azimuthal window considered above. The controlled signal is that obtained when the control algorithm convergence is reached. This figure demonstrates that a significant reduction of BVI-induced loads is achieved.

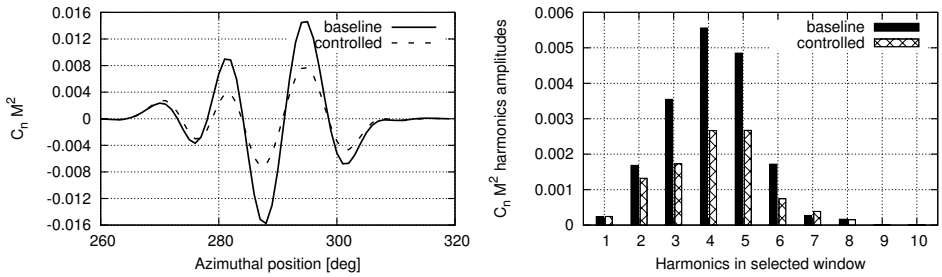

(a) Time history. (b) Spectrum.

Figure 4.22: $C_n M^2$ high-frequency, windowed signal from only-torsion aeroelastic model.

The corresponding actuation of the control variables are presented in Figure 4.23 in terms of their sine and cosine components, which refer to the input vector, **u**, expressed in the Eq. (4.4). Note that, these control variables

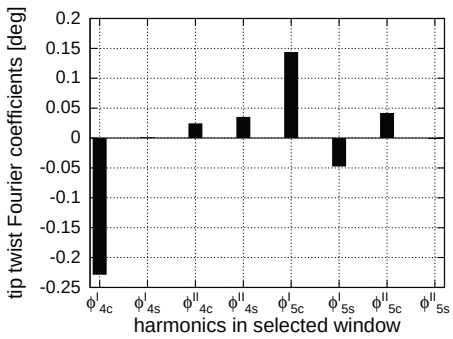

Figure 4.23: Control variables.

are such to yield a maximum peak-to-peak difference between controlled and uncontrolled responses of 0.6° at the blade tip. This is appreciable observing Figure 4.24, which depicts the effects of control action on blade tip torsion, also showing negligible transient oscillations due to actuation windowing.

Regarding the effects of control action on the acoustic field, the noise emitted on a horizontal plane located 2.3 m below the rotor hub is again examined and compared to the baseline condition. The differences between controlled and uncontrolled noise are presented in Figure 4.25, in terms of BVISPL. It is evident the presence of a quite large region of noise reduction in the rotor rear side (up to −7dB), whereas a noise increase (up to 2.5dB) appears in a limited area close to the rotor retreating side. This figure

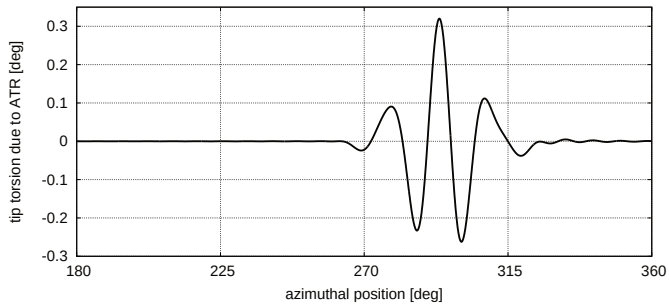

Figure 4.24: Difference between controlled and uncontrolled blade tip torsion.

demonstrates the evident effectiveness of the controller in alleviating the noise generated by the retreating-side BVI occurrence, particularly in the region behind the rotorcraft.

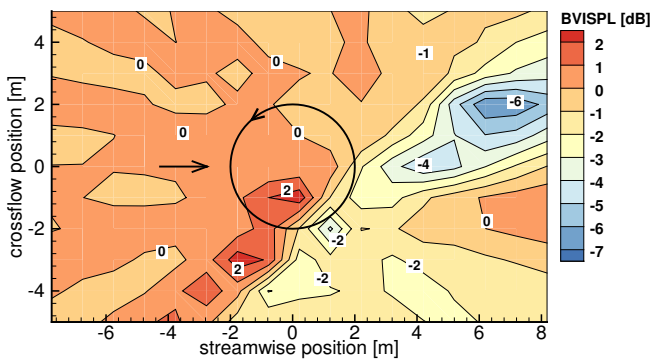

Figure 4.25: Effect of controller on BVISPL predicted by only-torsion model.

Furthermore, Figure 4.26 shows the difference between controlled and uncontrolled noise in terms of the OASPL, *i.e.*, including also the (not controlled) low-frequency harmonics. In this case, controller effects are smoother than those observed in Figure (4.25). The noise is generally alleviated with a maximum reduction of about 2dB, while the peak of noise increment (limited to a small region) is equal to 1dB.

The effects of the proposed control law on the emitted noise can be considered to be satisfactory, in that producing, with a remarkable directivity, reductions of noise levels in most of the examined region.

Finally, it is worth noting that the corresponding aeroelastic response has demonstrated no influence of control actuation on vibratory hub loads

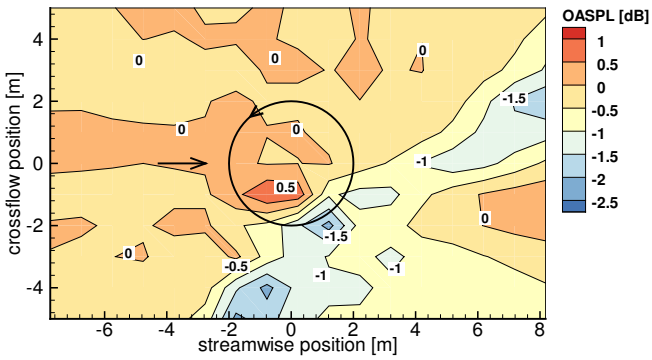

Figure 4.26: Effect of controller on OASPL predicted by only-torsion model.

transmitted to the airframe, thus confirming the advantage of high-frequency controllers in terms of drawbacks onset.

4.2.3 Noise control with complete rotor aeroelastic response

Here, results of high-frequency noise control application to a rotor simulated by a complete nonlinear, bending-torsional aeroelastic formulation are presented. Unlike the analysis discussed in the section above, here the aeroelastic tool yields a response that may significantly differ from that predicted by the sensitivity matrix, $\mathbf{T}$, used in the controller synthesis. Hence, following results represent a test for the proposed control robustness, namely, an assessment of its capability in providing good performance when applied to a system more complex than that used for its synthesis.

Figure 4.27 shows the high-frequency content of the $C_n M^2$ coefficient for the same blade section and azimuthal window considered in the previous analyses (in this case, the reference uncontrolled condition is the same shown in the preliminary analysis). Similarly, the controlled signal is that provided at the final step of the iterative control procedure. Moreover, Fig. 4.27b shows that, for the 4th and 5th windowed load harmonics, alleviations similar to those obtained by the only-torsion aeroelastic model are achieved, although the rest of the harmonics examined are subject to a smaller reduction. Nonetheless, the overall control effect appears still very satisfactory.

In Figure 4.28 the values of the corresponding $\mathbf{u}$ elements are depicted. In this case, the combination of these coefficients leads to a maximum peak-to-peak blade tip twist of 0.45°, showing that good results can be reached with smaller control effort, also. The difference between controlled and uncontrolled blade tip torsion responses is presented in Figure 4.29, showing

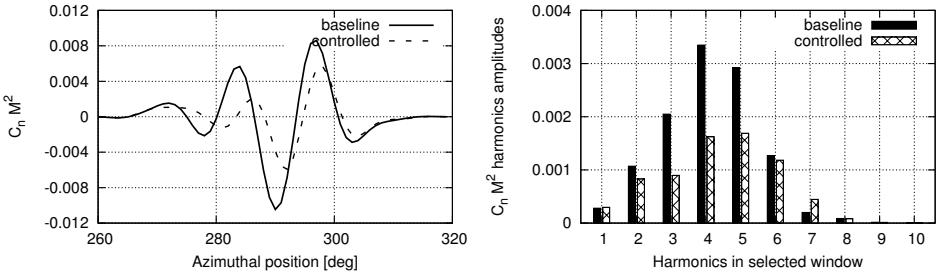

(a) Time history. (b) Spectrum.

Figure 4.27: $C_n M^2$ high-frequency, windowed signal from complete aeroelastic model.

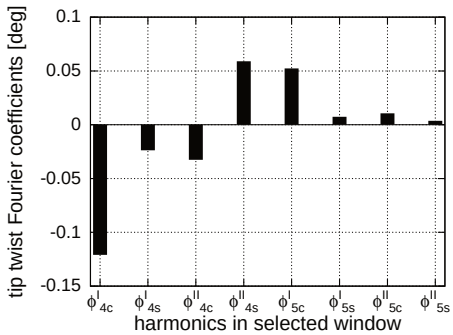

Figure 4.28: Control variables.

that transient effects due to actuation windowing are negligible also in this case.

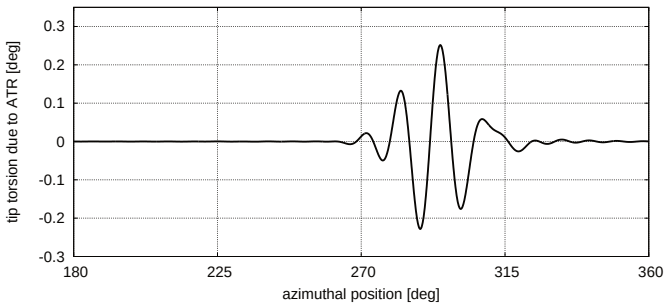

Figure 4.29: Difference between controlled and uncontrolled blade tip torsion.

Finally, the effect of the controller on noise alleviation is analyzed in terms of BVISPL contour plots, on the same plane considered above. Figure 4.31 presents the differences between the BVISPL distribution emitted by controlled and uncontrolled configurations. Compared to the results achieved by the only-torsion aeroelastic model, here a lower influence of the controller on the emitted sound is shown, both in terms of noise peaks and directivity modification. In this case, the maximum reduction of the BVISPL is about 2.7dB, whereas the BVISPL increase is grater than that from the only-torsion model, reaching 3dB in a limited portion of the observed region.

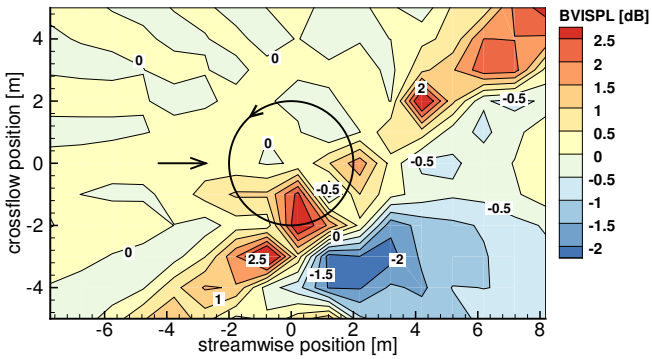

Figure 4.30: Effect of controller on BVISPL predicted by complete aeroelastic rotor simulation.

Furthermore, Figure 4.31 shows the control effectiveness in terms of differences between the OASPL distributions. This plot reveals that the inclusion of low-frequency acoustics tends to reduce peaks and the extent of the region where noise is increased; in this case, peaks of both augmented and alleviated noise are close to about 1.5dB.

In terms of vibration levels, also in this case, no differences have been found between baseline and controlled configurations, confirming the results obtained for the only-torsion blades rotor.

The outcomes presented in this section show that the efficiency of the control process proposed decreases when noise simulation is based on the complete rotor aeroelastic behaviour. Despite this, blade loads are still considerably alleviated, and a wide area in the vicinity of the rotor disk presents a satisfactory reductions of noise levels.

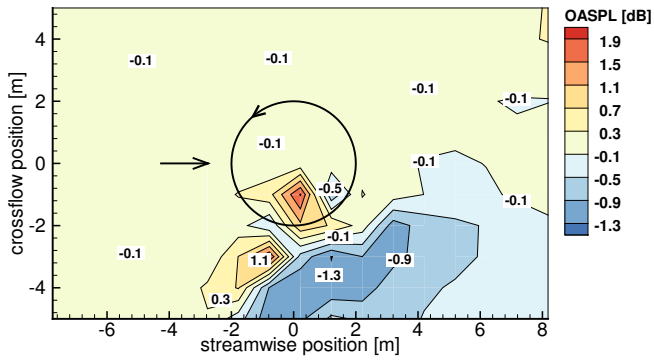

Figure 4.31: Effect of controller on OASPL predicted by complete aeroelastic rotor simulation.

4.3 Low-frequency active control for BVI noise alleviation

In this section, the low-frequency noise control methodology presented in Section 3.2 is applied to the model rotor presented in Appendix C.2 and already considered for the previous control application. The aim of the present control action is the reduction of BVI noise emitted through the application of spanwise distributed torque moments. The flight condition examined is the same descending flight of the previous case, chosen because affected by strong BVI events.

Control torque moments are assumed uniformly distributed along blade span between sections at 30% and 95% of blade radius. These are initially actuated in open-loop controls at different frequencies from 2/rev up to 5/rev, in order to assess effectiveness and convenience of different low-frequency controller actuations, and choice suitable input variables collected in vector $\mathbf{u}$[6] for the following closed-loop control application.

Noise measured at four microphones located on front and rear ends of helicopter skids (see Figure 4.32) are, instead, chosen as output (controlled) variables, observing the good correlation between noise reductions measured at on-board microphones and ground noise alleviation [91]. In particular, vector $\mathbf{z}$ collects SPLs of harmonics between the 6th and the 17th blade passage frequency of these signals, in that generally representative of BVI effects [11, 42].

[6]In particular, cosine and sine components of each torque moment harmonic are collected in the control input vector, $\mathbf{u}$.

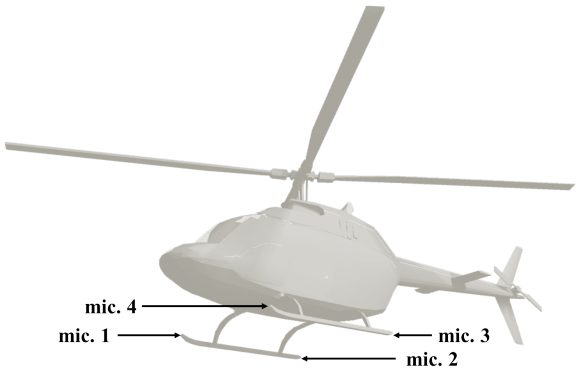

Figure 4.32: Location of on-board microphones.

First, preliminary studies are presented in the following, providing good understanding of open-loop, rotor acoustic response, in terms of high frequency noise emitted, to actuation of 2, 3, 4 and 5/rev active controls. The main purpose of these investigations is to determine the best actuation frequency, as best trade-off between effectiveness in reducing BVI noise and power consumption, for using it as control frequency in the closed-loop application. After this preliminary analysis, results from application of the proposed closed-loop noise control approach are presented and its effectiveness in BVI noise alleviation is discussed along with its drawbacks.

4.3.1 Preliminary analysis

Referring to the reference uncontrolled condition described in Section 4.2.1, assessment of system responses to 2, 3, 4 and 5/rev open-loop control actuations are independently carried out, and the corresponding results compared. These provide a detailed illustration of phenomenology involved in BVI occurrences and, moreover, allow to investigate some crucial aspects related to active control application, such as the choice of suitable input/output variables in the closed-loop controller, and the assessment of noise sensitivity to low frequency actuation. In particular, for each actuation frequency, a set of small perturbations of the ATR distributed torques are applied with different angular phases (incidentally, these simulations have also contributed to the definition of wake inflow database to be used in the closed-loop, control law synthesis process; see Section 2.4.1).

In this first analysis, the attention is focused on open-loop actuation effects on BVISPL and low-frequency sound pressure level (LFSPL, defined as the overall sound pressure level related to noise spectrum between the 1st

and the 5th bpf) at the same horizontal plane considered in noise contour plot in Figure 4.18.

Figure 4.33 compares (constant) mean values of baseline BVISPL and LFSPL with those predicted under the action of open-loop single-harmonic actuations, for several values of angular phases (amplitude of ATR distributed torques is unchanged). Specifically, in Figure 4.33a the capability of reduc-

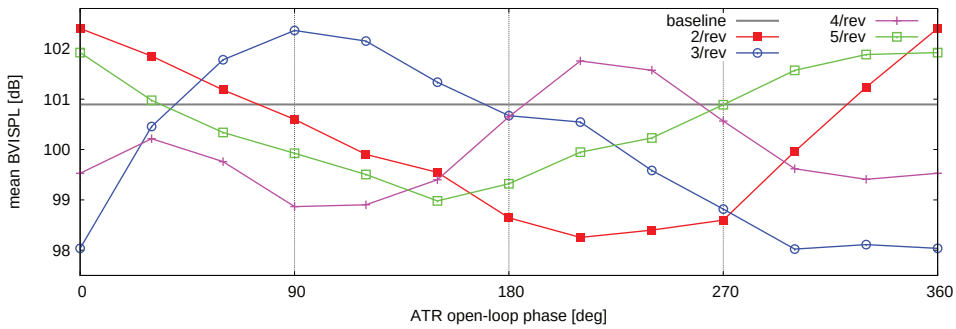

(a) Mean BVISPL.

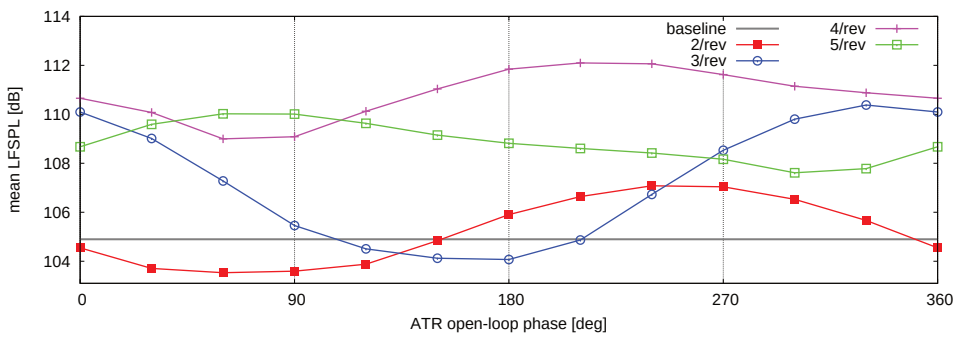

(b) Mean LFSPL.

Figure 4.33: Open-loop actuation effects on mean values of BVISPL and LFSPL.

ing mean BVI noise is observed in a wide range of angular phases for all the actuation harmonics considered, with greater effectiveness (higher maximum reduction achieved) shown by 2/rev and 3/rev ones.

Instead, Figure 4.33b shows a drawback of the proposed controller. Indeed, presenting the mean values of LFSPL, it highlights tendency of examined control action in increasing low-frequency noise. In particular, 4/rev and 5/rev actuations produce significant increase of LFSPL across the entire angular phase range, whereas for 2/rev and 3/rev ATR actuation, LFSPL

noise increase concerns smaller ranges of angular phases, and appears of lower intensity in the case of the lowest actuation frequency. However, low-frequency acoustic disturbance is scarcely annoying to the human ear, and this reduces the importance of the drawback shown[7].

A second by-product of the BVI noise controller deserving attention consists in the alteration vibrations transmitted to the fuselage. Figure 4.34

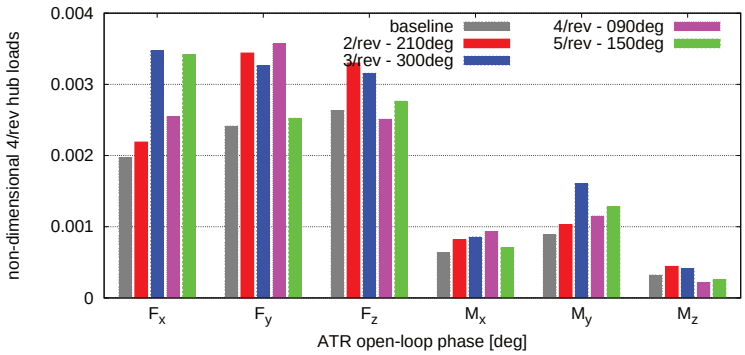

Figure 4.34: Vibratory 4/rev hub loads - minimum noise configurations.

compares 4/rev vibratory hub loads predicted for the baseline rotor configuration with those determined under single-harmonic ATR actuations. For each control frequency, the actuation law considers the angular phase corresponding to minimum BVISPL noise obtained (see Figure 4.33a). This figure proves that BVI noise reduction is typically associated with vibratory loads increase. A symmetrical behaviour has been observed in the case of blades optimized for vibrations reduction (Section 4.1.4), where an increase in the overall noise emitted was obtained for the optimized configuration, against a reduction of the vibratory loads. In the present application, mainly focusing on 2/rev and 3/rev actuation frequencies (in that, potentially the most effective ones for noise reduction), it is observed that their influence on vibratory loads is comparable, except for the in-plane longitudinal force, F_x, which is significantly excited by the 3/rev actuation.

Downstream of this preliminary analysis, 2/rev is selected as the actuation frequency in the closed-loop controller. Indeed, providing a potential reduction of BVI sound pressure levels comparable to that given by the

[7]Indeed, for the rotor model examined here, acoustic frequencies between 70Hz (*i.e.*, the 1^{st}bpf) and 350Hz (*i.e.*, the 5^{th}bpf) are considered in the LFSPL range. The human ear, that is highly frequency selective, appears instead more sensitive between 500Hz and 6kHz. This represents also the reason for frequent use of acoustic weighting curves (as, for example, the A-weighting), which correlate objective sounds measurements with the subjective human response.

3/rev actuation frequency, it is associated with smaller increase of both low-frequency noise emitted and vibratory hub loads. Furthermore, for equal amplitude of ATR torques, it is less power demanding due to the lower actuation rate.

Results in Figure 4.33a indicate that actuation angular phase equal to 210^{circ} provides the most effective 2/rev open-loop noise control in terms of mean value BVISPL reduction. The explanation of the fluid dynamics mechanism through which this occurs is given in Figure 4.35, where tip vortex-blade mutual positions corresponding to baseline rotor configuration (grey line) and actuated rotor blades (black line) are shown for a given BVI-critical rotor azimuth position in the first quarter of the advancing side: evidently, this severe parallel blade-vortex interaction appears significantly alleviated by the control action by means of increase of miss-distance. In the overall, actuated rotor blade-vortex interaction observed is weaker and tends to involve inner blade portions. Thus, this clearly shows how low-frequency control action reduces rotor acoustic disturbance by directly altering BVI phenomenon.

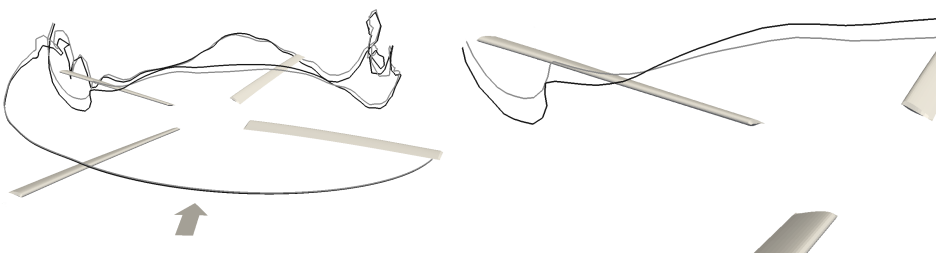

(a) Overall view. (b) Detailed view.

Figure 4.35: Advancing side BVI: uncontrolled (grey) and controlled (black) configurations.

Finally, Figure 4.36 presents results concerning alteration of mean BVISPL due to open-loop control, evaluated both on the considered carpet of microphones and at four positions selected on helicopter skids, as depicted in Figure 4.32.

The good correlation between noise control effects associated with these two predictions shows that output measurements at helicopter skids tips seem to be a suitable solution for the purpose of reducing noise emitted on a wide field region below the helicopter rotor by a closed-loop control based on a limited number of sensors, thus confirming what stated in Ref. [91].

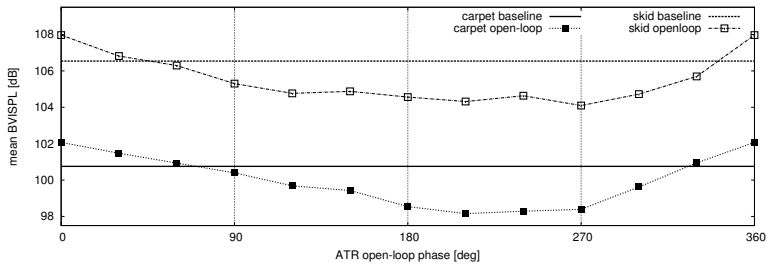

Figure 4.36: Skid-carpet noise prediction correlation.

4.3.2 Closed-loop control application

Here, effectiveness of 2/rev ATR closed-loop control in alleviating BVI rotor noise is investigated. As for the previous high-frequency control application, the controller law derives from the iterative adaptive **T**-matrix algorithm described in Section 3.2.

For the flight condition examined, the control process converges to ATR actuation with angular phase of 200^{circ} (*i.e.*, very close to that corresponding to maximum open-loop mean BVISPL reduction in Figure 4.33a), which yields maximum blade tip peak-to-peak twist of about 1.4^{circ}.

Firstly, the effects of this control action in terms of blade loads alteration are presented in Figure 4.37, which depicts uncontrolled and controlled time histories of $C_n M^2$ coefficient high-frequency content (> 10/rev), at the representative cross section $r/R = 0.95$. It reveals that the most relevant load

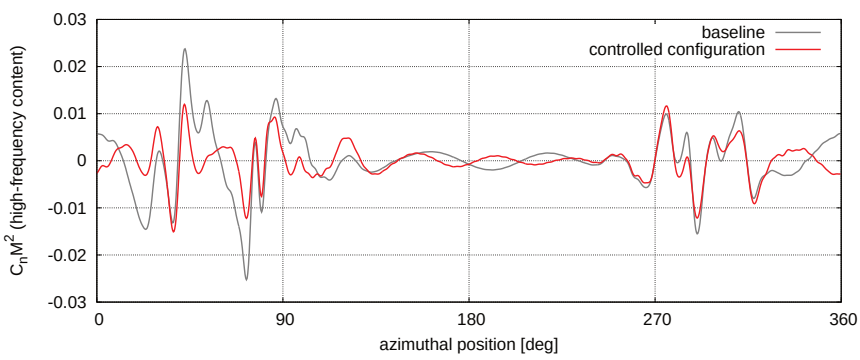

Figure 4.37: Time history of $C_n M^2$ high frequency content, at $r/R = 0.95$.

peaks due to BVI appearing in the advancing region are significantly alleviated by the control action, while a moderate effect is observed on weaker retreating side BVI loads.

Then, ATR closed-loop control effects on emitted noise are examined. Figure 4.38 shows the differences between baseline, $\mathbf{z}_0$, and converged controlled output variables. Specifically, results obtained through the efficient

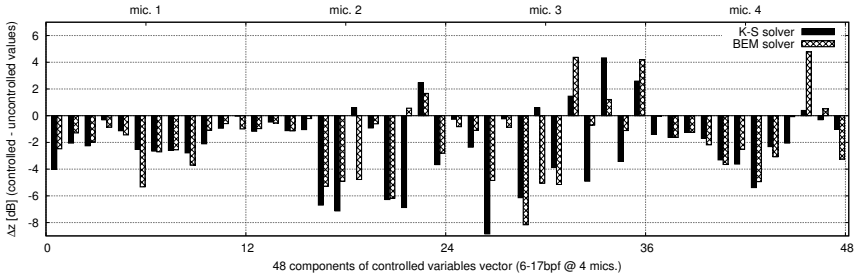

Figure 4.38: Effect of control on output variables.

solver used in controller synthesis and based on Küssner-Schwarz formulation coupled with the surrogate inflow model (indicated as "K-S solver"), are compared with those from the solver based on the high-fidelity BEM aerodynamic predictions (indicated as "BEM solver" solution). Note that, in this case, controlled BEM-based simulations are evaluated in open-loop mode, actuating ATR control as indicated by the converged "K-S solver" control process. This figure shows that, for most of noise harmonic components, "K-S solver" and "BEM solver" simulations of control effects are comparable, thus confirming the capability of the Küssner-Schwarz theory to provide quite accurate description of BVI unsteady loads and, at the same time, demonstrates control action effectiveness.

ATR control effects on rotor noise radiated on the considered carpet of microphones located below the rotor are depicted in Figures 4.39 and 4.40. Comparing controlled-rotor BVISPL in Figure 4.39 with the baseline BVISPL contour plot depicted in Figure 4.18 reveals that ATR actuation provides an overall reduction of high-frequency acoustic disturbance, except for a narrow area in the second quarter of the advancing side. This is highlighted in Figure 4.40, which depicts contour plot of BVISPL distribution variation due to controller. In the region examined, a maximum noise reduction of almost 6 dB is observed, whereas BVISPL increase in the advancing side is limited to 1 dB. Noise directivity pattern is not appreciably altered by blade control.

For the sake of completeness, Figure 4.41 presents uncontrolled and controlled LFSPL predicted on the same carpet of microphones. It demonstrates that emitted low-frequency noise is moderately increased by 2/rev closed-loop control action aimed at reducing higher-frequency noise, confirming the

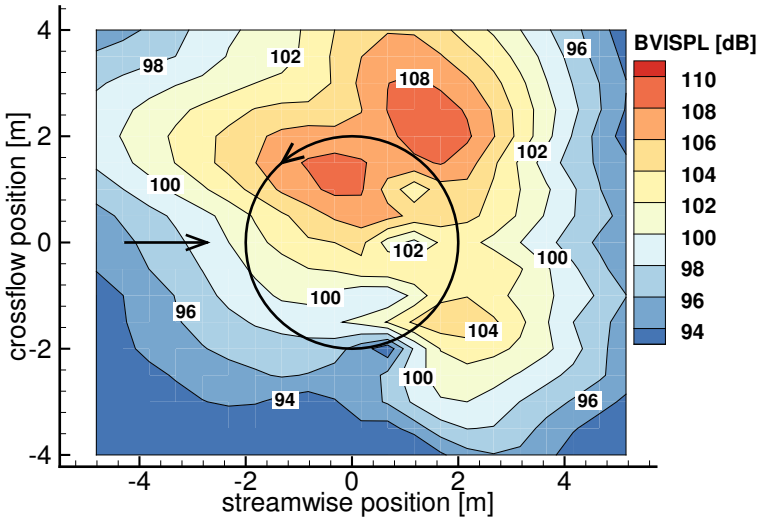

Figure 4.39: Controlled rotor BVISPL.

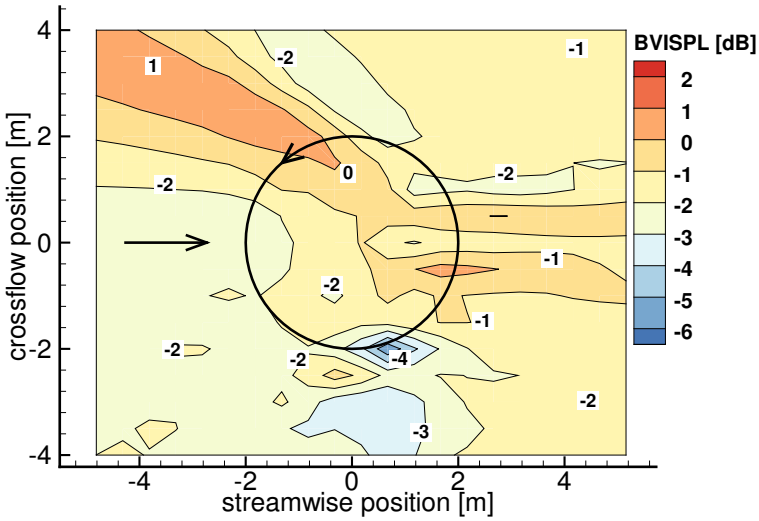

Figure 4.40: Difference between controlled and uncontrolled BVISPL.

outcomes of the open-loop preliminary analysis. However, as already stated, this is acceptable because of the negligible corresponding acoustic annoyance perceived by human ear[7].

Difficulty in simultaneous overall reduction of LFSPL and BVISPL through the proposed controller is confirmed by observing BVISPL and LFSPL mean

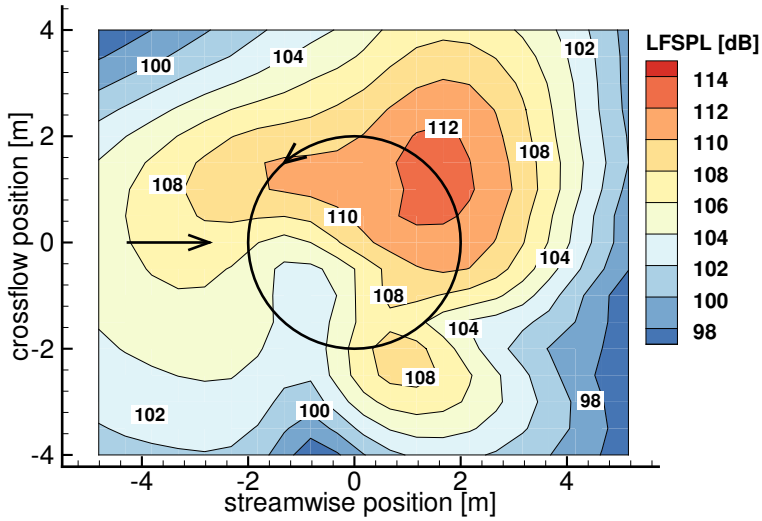

(a) Uncontrolled LFSPL.

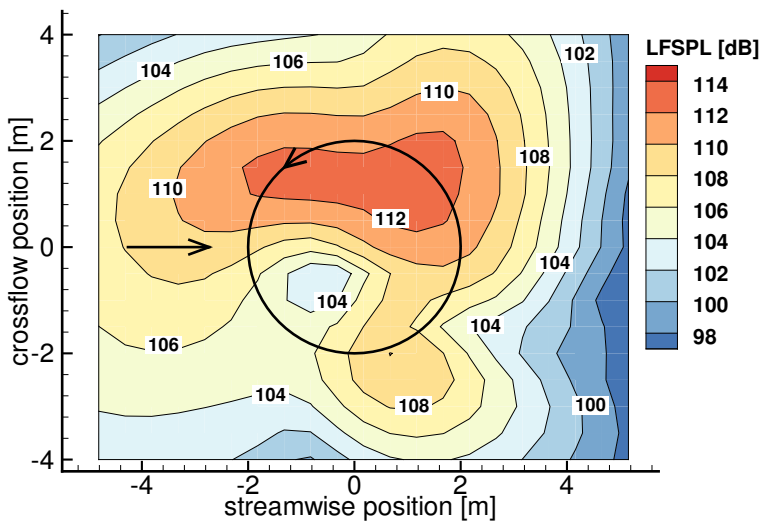

(b) Controlled LFSPL.

Figure 4.41: Low-frequency noise distribution.

values presented in Figure 4.33. It shows that both low-frequency and high-frequency noise alleviations are simultaneously obtained only in very short angular phase ranges of 2/rev and 3/rev actuation frequencies. However, even if considering the open-loop 2/rev frequency actuation with 120^{circ} angular phase falling within one of these ranges, Figure 4.42 demonstrates that

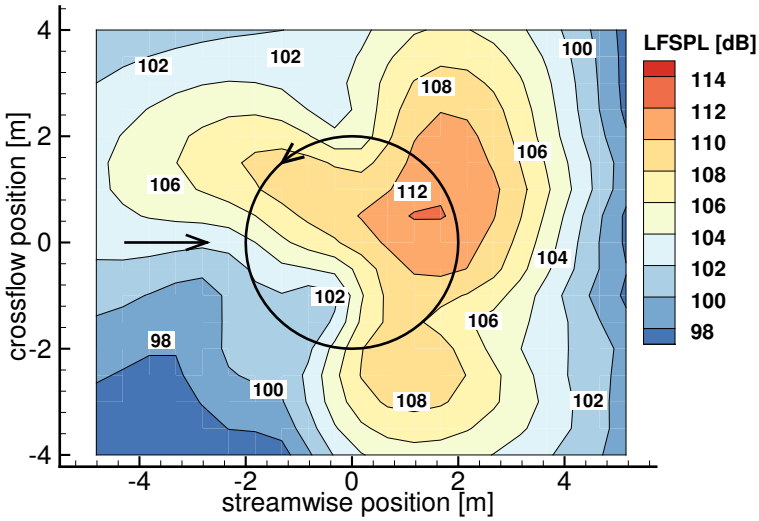

(a) Controlled LFSPL.

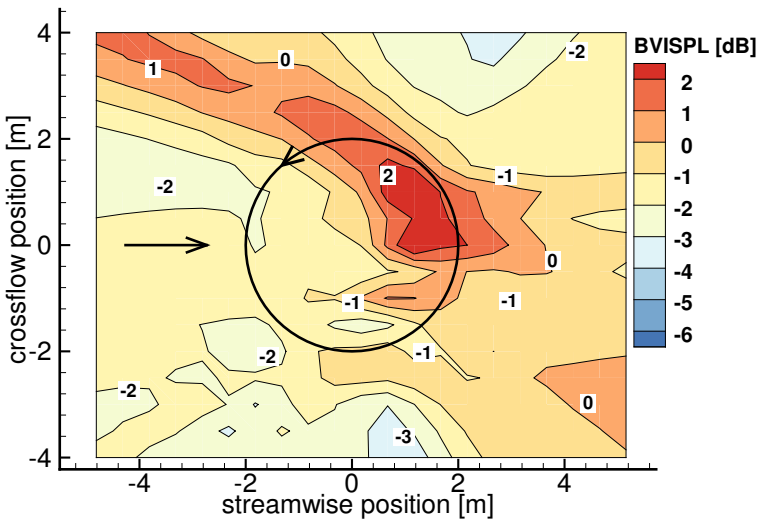

(b) Difference controlled-uncontrolled BVISPL.

Figure 4.42: Effects of 120°open-loop control on emitted noise.

corresponding effects on noise are conflicting. Indeed, the contour plot in Figure 4.42a compared with Figure 4.41a confirms beneficial influence of this specific control action on low-frequency content of emitted noise, but BVISPL control worsen, as shown by comparison of Figure 4.42b (where a large area of noise increase up to 2 dB is present in the advancing side region)

with Figure 4.40.

A second by-product of the present noise control activation concerns modification of vibratory loads transmitted to the fuselage. Figure 4.43 shows the comparison between 4/rev vibratory hub loads predicted for uncontrolled rotor and those deriving from the closed-loop control actuation. As typically occurring, noise reduction corresponds to increased vibratory loads. Nonetheless, for the case examined this drawback appears to be of limited, acceptable extent.

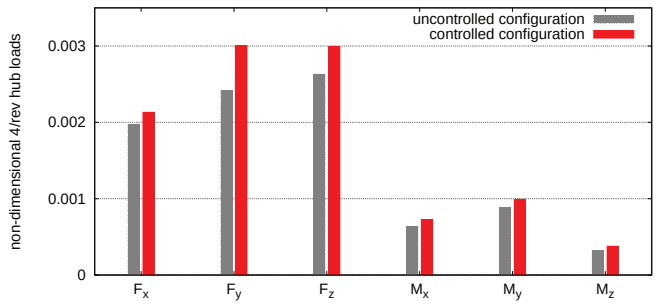

Figure 4.43: 4/rev vibratory hub loads.

A final investigation concerns the sensitivity of controller performance to the chosen monitored output variables, $\mathbf{z}$. Observing Figure 4.44, it is apparent that for all of the four microphones located at the skid ends, the most significant contribution to high-frequency noise comes from 6th to 11th bpf harmonics (note that the 12 harmonics represented per microphone range from the 6th to the 17th bpfs considered thus far). Starting from this observation, a new closed-loop controller based on vector $\mathbf{z}$ containing 6th to 11th noise bpfs is synthesized and applied, in order to investigate how the choice of the output monitored variables may affect controller effectiveness. The

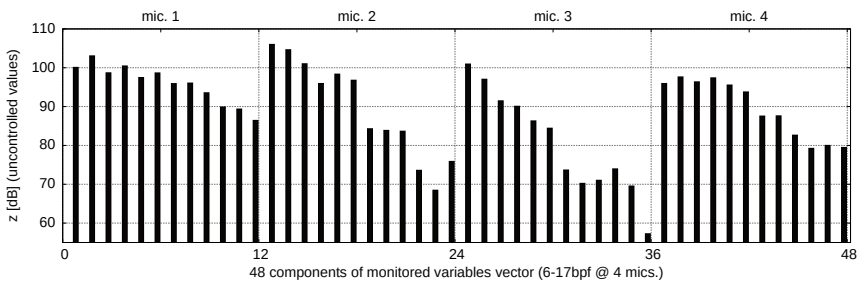

Figure 4.44: Uncontrolled monitored BVISPL harmonics.

converged ATR control action leads to a blade tip twist of about 2^{circ}, with angular phase equal to 221^{circ}. Effects of this controller on carpet microphones are shown in Figure 4.45. Comparing Figure 4.45a with Figure 4.40 reveals that the controller based on the selected number of most BVI-affected noise harmonics provides improved performance in terms of BVISPL reduction. On the other hand, Figure 4.45b compared with Figure 4.41b shows that this beneficial effect is associated with a slight further worsening of LF-SPL, which increases of 2 dB in the area already interested by the highest noise levels. This last application shows that, in reference to a given examined case, an optimal controller may be identified by adapting it to the most relevant specific outputs, and that, at the same time, this is always coupled with a drawback in terms of corresponding low-frequency noise increase.

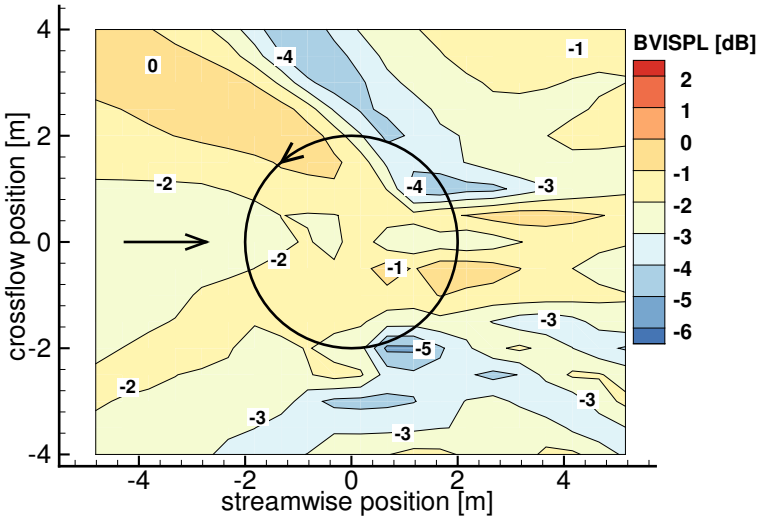

(a) Difference controlled-uncontrolled BVISPL.

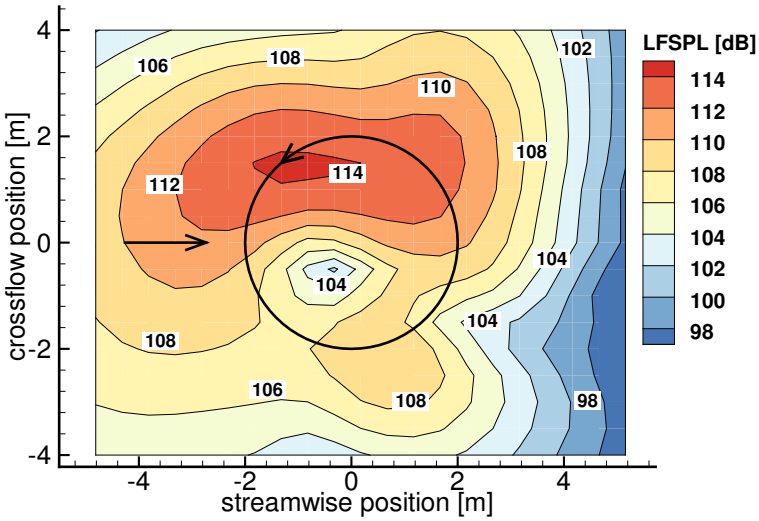

(b) Controlled LFSPL.

Figure 4.45: Control effects on high-frequency noise emitted.

Chapter 5

Concluding Remarks

Efficient formulations for fast and accurate rotor aeroelastic and aeroacoustic analyses are presented in this thesis. The availability of such tools is extremely useful in optimization and control synthesis procedures, and in the early stages of helicopter design, due to the high number of simulations that might be required. Some applications of the numerical tools developed are presented, in order to investigate different active and passive approaches for reducing vibratory hub loads and BVI noise due to the helicopter main rotors.

In particular, an advanced blade optimization has been investigated and successfully applied as passive approach, in which blade shape and its mechanical/structural properties have been selected using a genetic optimization algorithm, in order to reduce annoying vibratory loads at different flight conditions. Aeroelastic stability constraints have been considered during the search of minimum objective functions. Single-point and multi-point optimizations have been performed and robustness of the optimal configurations in off-design conditions have been examined, along with impact of low-vibrating blades on the emitted noise. Accuracy and computational efficiency have been guaranteed by application of surrogate wake inflow models, identified from a database given by a BEM aerodynamic solver. The effects of different surrogate models on the optimal results have been also investigated.

In examining active control strategies, benefits achievable through the active twist rotor (ATR) solution have been evaluated, investigating control effectiveness of both high-frequency and low-frequency actuators in reducing BVI noise generated during slow, descending flight conditions. An efficient procedure based on the optimal, multi-cyclic, control algorithm has been proposed and applied to identify the control law driving the ATR actuation. For the high-frequency control application, rotor blades have been actuated

through localized torque moments in order to drive their twist motion in specific intervals of the blade azimuth location, where the strongest interactions between blades and wake vortices occur. Instead, for the low-frequency control application, distributed torque moments have been actuated to produce low-frequency rotor blade twist and, in turn, alter directly blade-wake interaction and corresponding impulsive loads. In both cases, in order to ensure numerical efficiency and feasibility of a real-time controller, efficient aeroelastic and aeroacoustic solvers, based on surrogate wake inflow models and analytical sectional aerodynamic formulations, have been applied in the closed-loop actuation process. Furthermore, approximated adaptive methods for identification of the input-output gradient matrix of the local controller have been applied. Results obtained have been analysed in terms of noise control performance and onset of negative by-products effects like, for instance, vibratory hub loads and low-frequency noise increases.

The principal conclusions and observations of this studies are summarized in the following points, divided according to the different applications examined.

Blade optimization

- Both single-point and two-point blade optimization procedures successfully identify rotor blades configurations suited for vibratory hub loads alleviation at the flight condition(s) considered in the objective function (design conditions). Comparing results obtained, it has been observed that lower levels of vibration reduction are achievable for a single flight condition when in the objective function more flight conditions are considered. Further, the aeroelastic stability, imposed to the optimal rotor at the design flight conditions, is also maintained at off-design flights, including the critical hovering condition.
- Even a two-point optimization procedure has been shown to be unable to guarantee significant vibratory loads reductions in off-design flight conditions. Thus, vibratory hub loads reductions uniformly distributed throughout the helicopter flight envelope might be achieved by either including in the objective function several flight conditions or introducing active controls to reduce vibrations in off-design flights. The first strategy is simpler to apply in that does not require the application of active controls, but has the drawback of yielding low vibratory loads reductions. The implementation of the second one is more complex, but better performances might be achieved.

- Although the optimal design variables appear to be slightly affected by the surrogate inflow models applied in the blade optimization (with the sweep angle being the variable most affected), the different surrogate models have shown to be appropriate tools for the application, with accuracy depending on the specific configuration examined.
- When operating at off-design conditions, the identified low-vibrating rotor yields reduced objective functions, but spillover effects may occur (*i.e.*, the alleviation of each vibratory load component is not guaranteed), depending on the sensitivity of aerodynamic phenomena to changes of the flight condition.
- The acoustic assessment performed for the optimal rotor obtained has shown that low-vibrating blade configurations yield higher noise emissions, thus confirming the more acoustically annoying nature of low-vibrating rotors. At high-speed flight the increase of the acoustic peaks is not relevant, but the directivity of the noise emission pattern is significantly altered by blade re-design. At low-speed flight, the directivity of the noise is not significantly modified by blade re-design, but the acoustic peaks are subject to higher increase. The results of the present analysis suggest the inclusion of an acoustic annoyance measure within the objective function, using multi-objective optimization techniques, so as to define a tool capable to identify blades combining low vibration levels with low acoustic emissions. Using advanced low-vibrating blades with integration of active control systems aimed at reducing acoustic annoyance could be a valid alternative. This is especially suitable for low advance ratio flights, where the noise generated is particularly annoying for the community and more power is available to actuators, compared to high speed forward flight.

High-frequency active control

- Two different closed-loop high-frequency controls have been performed: first, considering a simplified aeroelastic system to derive the system response, then introducing the complete aeroelastic solver; a control law has been obtained for each application, leading a maximum peak-to-peak tip twist of 0.6° and 0.45°, respectively.
- Although significant reductions of the higher-harmonic loads and noise have been obtained in some areas of the acoustic field for both applications, more relevant BVI noise reductions and directivity pattern changes have been obtained when the simplified model has been used for system response (up to 7dB for the only-torsion response and 2.7dB for the complete aeroelastic response). In both cases, increase of the

controlled acoustic disturbance appears in a small area located below the rotor retreating side (more than 3dB in the worst case). Both positive and negative effects of the controller on the acoustic field appear mitigated (more than halved) if they are examined in terms of the OASPL, rather than in terms of the high-frequency acoustic content (BVISPL).
- Vibratory levels have been observed to be unaffected by control actuation, confirming the advantage of high-frequency controllers in terms of drawbacks onset.

Low-frequency active control

- Among the several actuation frequencies examined in the preliminary analysis, the 2/rev one appeared to be effective in reducing BVI noise, with limited drawbacks in terms of increase of vibratory loads and low-frequency acoustic disturbance with respect to 3, 4 and 5/rev actuations.
- A further preliminary result is the good correlation between noise evaluated on microphones in the field and noise evaluated at the on-board microphones located at the helicopter skid ends, thus proving the latter to be suitable as sensors in the closed-loop control chain.
- The application of the 2/rev ATR noise controller based on control law identified has been successful: in the field region observed, controlled noise have presented an overall satisfactory reduction of high-frequency components, without significant alteration of the directivity pattern. However, further investigations have been shown that efficiency of control action may be optimized, case by case, by suitable choice of output variables to be involved in the control algorithm.
- Drawbacks of noise control strategy adopted were limited increase of low-frequency noise and vibratory hub loads.

The findings mentioned above have proven the capacity of the proposed optimization approach for reduction of vibratory loads, and provided an assessment of the potentiality of two different active approaches for reducing noise due to BVIs occurrence, also confirming the attractiveness of smart materials for rotorcraft control applications, where low-mass, high-bandwidth actuators are of strong interest. Finally, the proposed efficient tools for rotor aeroelastic and aeroacoustic analyses can be considered successfully applied, and seem to be good candidates for the use in optimization and control synthesis procedures.

Appendix A

Blade Aeroelastic Modelling

In the following, an outline of the mathematical formulation implemented to predict the aeroelastic behaviour of curved elastic axis blades is presented (please, see Refs. [6, 7] for a more detailed description). First, a brief description of the structural model of arbitrarily curved blades is given, and then the equations applied for the quasi-steady aerodynamic sectional loads modelling are shown for the sake of completeness.

A.1 Blade structural dynamics model

A.1.1 Displacement variables and coordinate systems

Before developing the blade dynamics formulation, it is convenient to define main coordinate systems used and transformations relating the different frames of reference. Referring to the Figure A.1, the following orthogonal rotating systems of unit vectors are defined:

- a global system $(\vec{i}_1, \vec{i}_2, \vec{i}_3)$, centered at the rotor hub, with $\vec{i}_1$ tangent to the elastic axis at the root section;

- local systems $(\vec{e}_1, \vec{e}_2, \vec{e}_3)$, with $\vec{e}_1$ aligned to the undeformed blade elastic axis, and $\vec{e}_2, \vec{e}_3$ aligned with the blade section principal axes;

- local systems related to the blade deformed configuration having base unit vectors $(\vec{\hat{e}}_1, \vec{\hat{e}}_2, \vec{\hat{e}}_3)$, with $\vec{\hat{e}}_1$ tangent to the deformed elastic axis, and $\vec{\hat{e}}_2, \vec{\hat{e}}_3$ aligned with the principal axes of the elastically twisted blade sections.

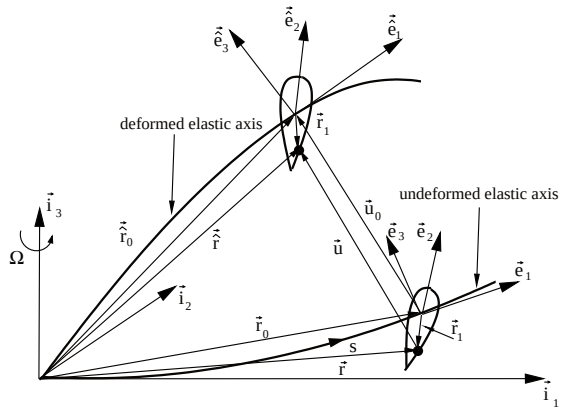

Figure A.1: Schematic representation of beam and coordinate systems [6, 7].

Then, the following matrices are defined for global to local undeformed-blade references transformations

$$\{\vec{e}_i\} = \mathbf{A}(s) \left\{\vec{i}_i\right\}$$

and the local blade-undeformed to local blade-deformed references transformations

$$\left\{\vec{\hat{e}}_i\right\} = \mathbf{T}(s) \left\{\vec{e}_i\right\}$$

where s denoting the curvilinear coordinate defined along the undeformed elastic axis.

Deformations are described in terms of displacement of the elastic axis and rotation of beam sections. The displacement components, u, v and w, are defined in the local frames fixed with the undeformed blade, respectively along the directions identified by $\vec{e}_1, \vec{e}_2$ and $\vec{e}_3$; the blade elastic torsion, ϕ, is defined as the rotation of the blade sections about direction $\vec{\hat{e}}_1$ (*i.e.*, about the deformed elastic axis).

A.1.2 Equilibrium relations

Considering a deformed beam element of length ds, the equilibrium of forces and moments acting on it yields

$$\frac{\partial \vec{v}}{\partial s} + \vec{p} = 0 \tag{A.1}$$

$$\frac{\partial \vec{m}}{\partial s} + \vec{\hat{e}}_1 \times \vec{v} + \vec{q} = 0 \tag{A.2}$$

where $\vec{v}$ and $\vec{m}$ are the internal structural forces and moments about the elastic axis, while $\vec{p}$ and $\vec{q}$ are the equipollent external distributed forces and moments.

In order to integrate the above differential equilibrium equations, it is convenient to write them in terms of forces and moments components, $\mathbf{v}_l, \mathbf{m}_l, \mathbf{p}_l, \mathbf{q}_l$, in the local, blade-undeformed frames. The equilibrium equations, projected onto the frame $\left\{\vec{i}_i\right\}$ and integrated, yield the following distribution of the internal shear loads

$$\mathbf{v}_l(s) = \mathbf{A} \int_s^R \mathbf{A}^T \mathbf{p}_l \, d\hat{s} \tag{A.3}$$

and internal moments

$$\mathbf{m}_l(s) = \mathbf{A} \left\{ \int_s^R \mathbf{A}^T \mathbf{q}_l \;\, d\hat{s} - \int_s^R \left(\mathbf{A}^T \mathbf{H}_l \mathbf{A} \int_{\hat{s}}^R \mathbf{A}^T \mathbf{p}_l \;\, d\tilde{s} \right) \;\, d\hat{s} \right\} \tag{A.4}$$

where $\mathbf{H}_l$ is the matrix of the components in the local undeformed frame of the axial tensor associated to vector $\vec{\tilde{e}}_1$, and R denotes the length of the undeformed elastic axis (thus neglecting second-order terms related to local slope).

Equations A.3 and A.4 are the general solutions for the internal shear loads and moments arising in a beam, from which the equations governing the blade elastic deformation may be derived, once strain-displacement and load-displacement relations are identified (see Refs. [6, 7]). Note that, because of shear undeformable assumption, the equations governing the blade deformation variables, u, v, w and ϕ, are derived from the first scalar equation in Eq. (A.3) and the three scalar equations in Eq. (A.4) (the second and the third scalar equations in Eq. (A.3) are used to determine the shear loads components lying in the plane of the beam cross sections).

A.1.3 Inertial loads

In case of a rotor blade, rotation effects and unsteady deformations make inertial loads arise. These appear in the equilibrium equations as external distributed loads and, combined with the internal structural loads, yield the equations governing the blade structural dynamics.

The acceleration of a generic point of the rotating blade is given by

$$\vec{a} = \vec{a}_r + \vec{a}_H + \vec{\Omega} \times \vec{\Omega} \times \vec{\hat{r}} + 2\vec{\Omega} \times \vec{\nu}$$

where $\vec{a}_r$ is the acceleration of the point with respect to a frame of reference rigidly connected to the undeformed blade. It is derived from the rigid motion of the beam cross sections expressed in terms of displacements of the elastic

axis and rotations about it. In addition, $\vec{a}_H$ is the rotor hub acceleration, $\vec{\nu}$ is the velocity of the examined point with respect to the frame fixed with the undeformed blade, while $\vec{\Omega}$ is the blade angular velocity.

Then, the resulting inertial distributed loads appearing in Eqs. A.1 and A.2 are expressed as

$$\begin{aligned} \vec{p} &= -\int_A \rho\, \vec{a}\, d\eta\, d\zeta \\ \vec{q} &= -\int_A \rho\, \vec{r}_s \times \vec{a}\, d\eta\, d\zeta \end{aligned}$$

where ρ is the material density and $\vec{r}_s = \vec{\hat{r}} - (\vec{r}_0 + u\vec{e}_1 + v\vec{e}_2 + w\vec{e}_3)$.

A.2 Aerodynamic loads

Aeroelastic application of the blade structural model outlined above requires the introduction of external aerodynamic loads. In the applications proposed in this thesis, the aerodynamic loads are derived from a quasi-steady approximation of the Greenberg theory [60, 61] for airfoils. Three-dimensional effects are taken into account by including wake inflow corrections, as stated in Chapter 2. Thus, the section force orthogonal to the chord, T, and the section force parallel to the chord, S, are given by

$$\begin{aligned} T &= \frac{\varrho\, C_{l_\alpha} c}{2}\left[-U_P U_T + \frac{c}{2}\,\omega\, U_T - \frac{c}{4}\dot{U}_P + \left(\frac{c}{4}\right)^2 \dot{\omega}\right] \\ S &= \frac{\varrho\, C_{l_\alpha} c}{2}\left[U_P^2 - \frac{c}{2}\,\omega\, U_P - \frac{C_{d_0}}{C_{l_\alpha}} U_T^2\right] \end{aligned}$$

while the section pitching moment at the quarter-chord point reads

$$M_\phi = -\frac{\varrho\, C_{l_\alpha} c^3}{32}\left(\omega\, U_T - \dot{U}_P + \frac{3c}{8}\dot{\omega}\right)$$

In the above equations, U_P and U_T are, respectively, the quarter-chord velocity components orthogonal and parallel to the chord after deformation, ω is the out-of-section component of the angular velocity of the blade section, c denotes the chord length, ϱ is the air density, C_{l_α} is the lift curve slope coefficient, while C_{d_0} is the drag coefficient.

The blade aeroelastic equations are derived by expressing U_P, U_T and ω in terms of u, v, w and ϕ and the aerodynamic forces T and S in terms of components in the local blade-undeformed frame of reference.

A.3 Numerical implementation

Combining internal and inertial loads with the first scalar equation in Eq. (A.3) and the three scalar equations in Eq. (A.4) yields a set of four integro-differential equations in the deformation unknowns, u, v, w, and ϕ, governing the structural dynamics of the curved blade. Akin to the approach followed in Ref. [60], the axial degree of freedom, u is derived as a consequence of beam bending, imposing axial strain $\epsilon_{xx} = 0$. The resulting set of governing equations is now that in Eq. (A.4), with unknown variables v, w, and ϕ. These equations are spatially integrated through the Galerkin approach, starting from description of elastic axis deformation as a linear combination of shape functions that satisfy homogeneous boundary conditions. Specifically, it consists in expressing blade displacements as

$$\begin{aligned} v(s,t) &= \sum_{n=1}^{N_v} q_n^v(t)\psi_n^v(s) \\ w(s,t) &= \sum_{n=1}^{N_w} q_n^w(t)\psi_n^w(s) \\ \phi(s,t) &= \sum_{n=1}^{N_\phi} q_n^\phi(t)\psi_n^\phi(s) \end{aligned}$$

with q_n^v,q_n^w,q_n^ϕ Lagrangian variables of the problem, and ψ_n^v, ψ_n^w, ψ_n^ϕ conveniently chosen as bending and torsion natural modes of vibration of a non-rotating, straight, cantilever beam [60].

The resulting aeroelastic system consists of a set of $(N_v + N_w + N_\phi)$ nonlinear, time-dependent equations with unknowns $\mathbf{q}$ which can be applied both for aeroelastic response and stability analyses. They may be rewritten as

$$\mathbf{f}_{el}(t,\mathbf{q}) + \mathbf{f_{in}}(\mathbf{t},\mathbf{q}) + \mathbf{f_{aero}}(\mathbf{t},\mathbf{q}) = \mathbf{0} \tag{A.5}$$

where $\mathbf{f}_{in}$, $\mathbf{f}_{aero}$ and $\mathbf{f}_{el}$ are the inertial, aerodynamic, and elastic generalized forces, respectively, and $\mathbf{q}$ is the vector collecting the Lagrangian variables of the problem, q_n^v, q_n^w, q_n^ϕ.

A.3.1 Aeroelastic response

Aeroelastic steady-periodic responses are numerically predicted through a harmonic balance approach. It is a methodology suitable for the analysis of the asymptotic solution (as time goes to infinity) of differential equations

forced by periodic terms, as it generally occurs in rotorcraft applications. The harmonic balance solution consists of: (i) expressing the contributions in Eq. (A.5) in terms of their Fourier series; (ii) equating the resulting harmonic coefficients; (iii) solving the corresponding algebraic system in terms of the unknown Fourier coefficients of the Lagrangian coordinates of the problem. Specifically, expressing $\mathbf{q}$ and $\mathbf{f} = \mathbf{f}_{el} + \mathbf{f}_{in} + \mathbf{f}_{aero}$ in terms of the following Fourier series

$$\begin{aligned}
\mathbf{q}(\mathbf{t}) &= \mathbf{q}_0 + \sum_{k=1}^{K} [\mathbf{q}_k^c \cos(\Omega_k t) + \mathbf{q}_k^s \sin(\Omega_k t)] \\
\mathbf{f}(t) &= \mathbf{f}_0 + \sum_{k=1}^{K} [\mathbf{f}_k^c \cos(\Omega_k t) + \mathbf{f}_k^s \sin(\Omega_k t)]
\end{aligned}$$

where $\mathbf{q}_k^c, \mathbf{q}_k^s, \mathbf{f}_k^c$ and $\mathbf{f}_k^s$ denote cosine and sine components of the k-th harmonic of $\mathbf{q}$ and $\mathbf{f}$, whereas $\Omega_k = k\Omega$ with Ω representing the fundamental frequency (*i.e.*, the rotor angular velocity) Eq. (A.5) becomes

$$\hat{\mathbf{f}}\,(\hat{\mathbf{q}}) = \mathbf{0} \tag{A.6}$$

with $\hat{\mathbf{q}}^T = \{\mathbf{q}_0\ \mathbf{q}_1^c\ \mathbf{q}_1^s\ \mathbf{q}_2^c\ \mathbf{q}_2^s\ \cdots\}$ and $\hat{\mathbf{f}}^T = \{\mathbf{f}_0\ \mathbf{f}_1^c\ \mathbf{f}_1^s\ \mathbf{f}_2^c\ \mathbf{f}_2^s\ \cdots\}$. Because of the presence of nonlinear terms, Eq. (A.6) has to be solved using an iterative procedure. To this aim, the Newton-Raphson method is applied.

A.3.2 Aeroelastic stability

Aeroelastic stability analysis is based on the eigenanalysis of the following set of linearised equations, where $\mathbf{q_0}$ is the reference (equilibrium) configuration obtained as aeroelastic solution

$$\mathbf{M}(\mathbf{q_0}, \mathbf{t})\,\ddot{\mathbf{q}} + \mathbf{C}(\mathbf{q_0}, \mathbf{t})\,\dot{\mathbf{q}} + \mathbf{K}(\mathbf{q_0}, \mathbf{t})\,\mathbf{q} = \mathbf{0}$$

In the above equation, $\mathbf{M}$, $\mathbf{C}$ and $\mathbf{K}$ are, respectively, mass, damping and stiffness matrices, numerically identified as

$$M_{ij} = \left.\frac{\partial f_i}{\partial \ddot{q}_j}\right|_{\mathbf{q_0}} \;;\; C_{ij} = \left.\frac{\partial f_i}{\partial \dot{q}_j}\right|_{\mathbf{q_0}} \;;\; K_{ij} = \left.\frac{\partial f_i}{\partial q_j}\right|_{\mathbf{q_0}}$$

with $(\cdot)|_{\mathbf{q_0}}$ denoting evaluation for $\mathbf{q} = \mathbf{q_0}$.

Appendix B

Rotor Hub Filtering Effect

For the problem illustrated here, an helicopter rotor hub dynamically balanced with an arbitrary number N_b of identical blades is considered, following the approach in Refs. [3, 8]. Hence, the shear forces (similar considerations can be made for the moments) at each blade root can be described by the same Fourier series with different angular phases. Referring to the coordi-

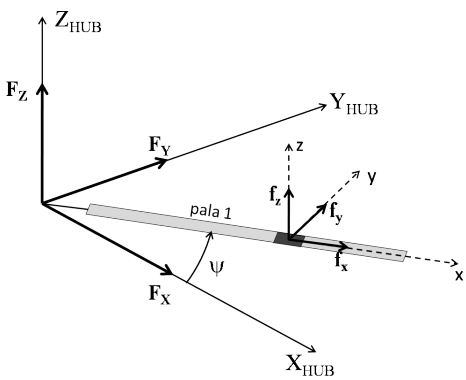

Figure B.1: Definition of lade and hub shears and moments.

nate system shown in the Figure B.1, and denoting the azimuthal position of the k-th blade by

$$\psi_k = \Omega t + \frac{2\pi}{N_b} k \quad , \qquad k = 1, ..., N_b$$

shears at root of the k-th blade can be written as

$$
\begin{aligned}
f_{x,k} &= f_x^0 + \sum_{n=1}^{\infty}\left[f_{x,n}^c\cos(n\psi_k) + f_{x,n}^s\sin(n\psi_k)\right] \\
f_{y,k} &= f_y^0 + \sum_{n=1}^{\infty}\left[f_{y,n}^c\cos(n\psi_k) + f_{y,n}^s\sin(n\psi_k)\right] \\
f_{z,k} &= f_z^0 + \sum_{n=1}^{\infty}\left[f_{z,n}^c\cos(n\psi_k) + f_{z,n}^s\sin(n\psi_k)\right]
\end{aligned} \tag{B.1}
$$

Assuming a steady-periodic condition, the total hub components of shears and moments can be found by summing contributions of each blade. Considering, as example, the only vertical, F_Z, and longitudinal, F_X, components, the following expression can be written for the contribution of a single blade:

$$
\begin{aligned}
F_{X,k} &= f_{x,k}\cos\psi_k - f_{y,k}\sin\psi_k \\
F_{Z,k} &= f_{z,k}
\end{aligned}
$$

Summing all the contributions, and using some trigonometric identities, total hub loads are obtained as:

$$
\begin{aligned}
F_X &= \frac{N_b}{2}\left[f_{x,1}^c - f_{y,1}^s\right] + \\
&+ \frac{N_b}{2}\sum_{n=1}^{\infty}\left[\left(f_{x,nN_b-1}^c + f_{y,nN_b-1}^s + f_{x,nN_b+1}^c - f_{y,nN_b+1}^s\right)\cos(nN_b\psi)\right] + \\
&+ \frac{N_b}{2}\sum_{n=1}^{\infty}\left[\left(f_{x,nN_b-1}^s - f_{y,nN_b-1}^c + f_{x,nN_b+1}^s + f_{y,nN_b+1}^c\right)\sin(nN_b\psi)\right] \\
F_Z &= N_b\left\{f_x^0 + \sum_{n=1}^{\infty}\delta_{n(nN_b)}\left[f_{z,n}^c\cos(n\Omega t) + f_{z,n}^s\sin(n\Omega t)\right]\right\}
\end{aligned} \tag{B.2}
$$

where δij is the Kronecker delta:

$$
\delta_{ij} = \begin{cases} 1; & for \;\; i = j \\ 0; & for \;\; i \neq j \end{cases}
$$

Starting from results obtained for these two shear loads, and noting that similar expressions can be found for the other loads (see, for example, Refs. [3, 8]), the following final considerations can be made:

- the hub acts as a filter for steady harmonic loads, in that admitting only the harmonics that are multiples of the number of blades N_b;

- for vertical shear load, F_Z, (and rotor torque, M_Z) blade loads contribution to the nN_b/rev hub loads have the same nN_b/rev frequency content;
- for in-plane components, F_X and F_Y, resultant nN_b/rev hub loads admit only the $(nN_b + 1)$ and $(nN_b - 1)$ blade harmonics (same results are obtained for corresponding moments, see Refs. [3, 8]).

Appendix C

Rotor Helicopter Models Considered

The numerical applications presented in this thesis have been carried out referring to two different models of helicopter rotor. A first rotor has been considered in the blade optimization aimed at reducing the level of vibratory loads transmitted to the hub, whose results are shown in Section 4.1. The second rotor has instead been considered in applications involving the use of active controls for the reduction of BVI noise, whose results are shown in Sections 4.2 and 4.3. The main characteristics of the two rotors are listed below.

C.1 Main rotor used in blade optimization

The optimal design processes have been applied to a counter-clockwise rotating, four-bladed, hingeless, BO-105 rotor type configuration having structural, geometric and aerodynamic characteristics given in Table C.1. Both the baseline and optimized rotor blades has been assumed to have uniform structural properties. Rotor control settings have been determined as those corresponding to the rotor momentum trim for each flight condition and blade configuration considered.

All computations have been carried out using nine shape functions in the modal description of each structural degree of freedom, whereas five harmonics have been included in the harmonic balance solution (these discretization parameters guarantee aeroelastic converged results).

Characteristic	Symbols	Values
blade radius [m]	R	4.91
rotational speed [rad/s]	Ω	44.506
airfoil		NACA 0015
lift coefficient	$C_{l\alpha}$	6.28
drag coefficient	C_{D0}	0.01
chord	c/R	0.055
solidity	σ	0.07
thrust coefficient	C_T	0.005
blade linear twist [deg]	θ_{tw}	-8.0
precone angle [deg]	β_{pc}	0.0
Lock number	γ	5.5
aerodynamic cut-off	x_{ae}/R	0.16
mass per unit length [kg/m]	m_0	5.56
flap stiffness	$EI_\eta/m_0\Omega^2R^4$	0.01060
lead-lag stiffness	$EI_\zeta/m_0\Omega^2R^4$	0.03010
torsional stiffness	$GJ/m_0\Omega^2R^4$	0.00147
flap mass moments of inertia	k_{m1}/R	0.02
lead-lag mass moments of inertia	k_{m2}/R	0.0
polar radius of gyration	$k_A^2/(k_{m1}^2+k_{m2}^2)$	0.0

Table C.1: Rotor blade properties.

C.2 Main rotor used for active control applications

For the noise control applications presented in this thesis, a counter-clockwise rotating, four-bladed, fully hingeless model rotor has been considered. Its main properties are listed in Table C.2.

Furthermore, blade mass distribution is given in Figure C.1, whereas blade structural properties are reported, in Table C.3, in terms of rotating frequencies.

Rotor control settings have been determined as those corresponding to the rotor momentum trim for the flight condition considered in the application.

All computations have been carried out using seven shape functions in the modal description of each structural degree of freedom, whereas five harmonics have been included in the harmonic balance solution (these discretization parameters guarantee aeroelastic converged results).

Characteristic	Symbols	Values
blade radius [m]	R	2.0
rotational speed [rad/s]	Ω	109.12
airfoil		NACA 23012
lift coefficient	$C_{l\alpha}$	6.0
drag coefficient	C_{D0}	0.01
chord	c/R	0.06
solidity	σ	0.077
thrust coefficient	C_T	0.005
blade linear twist [deg]	θ_{tw}	-8.0
precone angle [deg]	β_{pc}	2.5
Lock number	γ	5.25
aerodynamic cut-off	x_{ae}/R	0.22

Table C.2: Rotor blade properties.

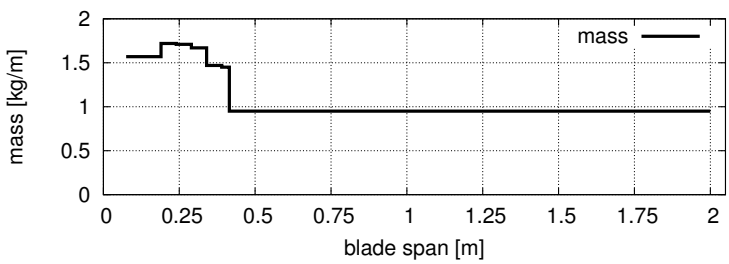

Figure C.1: Blade mass distribution.

Mode	Frequency [Hz]
lag	13.54
flap	48.82
torsion	89.15

Table C.3: Blade flap, lag and torsional first rotating frequencies.

Bibliography

[1] Edwards, B., Cox, C., and Worth, F., "Revolutionary Concepts for Helicopter Noise Reduction — S.I.L.E.N.T. Program," *Contract*, , No. May, 2002.

[2] Leishman, J. G., *The Helicopter: Thinking Forward, Looking Back*, College Park Press, 2007.

[3] Bramwell, A. R. S., Balmford, D., and Done, G., *Bramwell's Helicopter Dynamics*, Elsevier Science, 2001.

[4] Monner, H., Riemenschneider, J., Opitz, S., and Schulz, M., "Development of active twist rotors at the German Aerospace Center (DLR)," *proceedings of the 52nd AIAA/ASME/ASCE/AHS/ASC Structures, Structural Dynamics and Materials Conference*, No. April, 2011, pp. 1–10.

[5] Thom, A. and Duraisamy, K., "High-Resolution Simulation of Parallel Blade-Vortex Interactions," *AIAA Journal*, Vol. 48, No. 10, Oct. 2010, pp. 2313–2324.

[6] Piccione, E., Bernardini, G., Molica Colella, M., and Gennaretti, M., "Structural and Aeroelastic Modeling of Curved Rotor Blades Using a Galerkin Approach," *Proceedings of 3rd CEAS Air & Space Conference/21st AIDAA Congress*, Venice, Italy, 2011, pp. 615–624.

[7] Piccione, E., Bernardini, G., Molica Colella, M., and Gennaretti, M., "A Spectral Formulation for Structural/Aeroelastic Modeling of Curved-Axis Rotor Blades," *Aerotecnica Missili & Spazio*, Vol. 91, No. 1-2, 2012, pp. 42–52.

[8] Arra, M., *L'elicottero*, Biblioteca tecnica Hoepli, Hoepli, 2001.

[9] McGowen, S. S., *Helicopters: An Illustrated History of Their Impact*, Weapons and warfare series, ABC-CLIO, 2005.

[10] Yu, Y., "Rotor Blade-Vortex Interaction Noise," *Progress in Aerospace Sciences*, Vol. 36, No. 2, Feb. 2000, pp. 97–115.

[11] Patt, D., Liu, L., and Friedmann, P. P., "Simultaneous Vibration and Noise Reduction in Rotorcraft Using Aeroelastic Simulation," *Journal of the American Helicopter Society*, Vol. 51, No. 2, 2004, pp. 127–140.

[12] Kessler, C., "Active Rotor Control for Helicopters: Individual Blade Control and Swashplateless Rotor Designs," *CEAS Aeronautical Journal*, Vol. 1, No. 1-4, May 2011, pp. 23–54.

[13] Hartjes, S., Buys, Y., Visser, H. G., Pavel, M., Gennaretti, M., Bernardini, G., and Arntzen, M., "Optimization of Rotorcraft Noise Abatement Trajectories," *Proceedings of Internoise Conference*, New York City, USA, 2012.

[14] Flannelly, W. G., "The Dynamic Anti-Resonant Vibration Isolator," *Proceedings of 22nd Annual Forum of the American Helicopter Society*, Washington, D.C., USA, 1976.

[15] Friedmann, P. P., "Helicopter Vibration Reduction Using Structural Optimization with Aeroelastic/Multidisciplinary Constraints - A Survey," *Journal of Aircraft*, Vol. 28, No. 1, 1991, pp. 8–21.

[16] Chattopadhyay, A., "Vibration Reduction in an Articulated Rotor Blade Using Structural Optimization," *Engineering Optimization*, Vol. 19, No. 1, 1992, pp. 37–50.

[17] He, C. and Peters, D., "Optimization of Rotor Blades for Combined Structural, Dynamic, and Aerodynamic Properties." *Structural Optimization*, Vol. 5, 1992, pp. 37–44.

[18] Crossley, W. A., "Genetic algorithm approaches for multiobjective design of rotor systems," *Proceedings of the 6th AIAA, NASA, and ISSMO, Symposium on Multidisciplinary Analysis and Optimization*, 1996, pp. 384–394.

[19] Ganguli, R. and Chopra, I., "Aeroelastic Optimization of an Advanced Geometry Helicopter Rotor," *Journal of the American Helicopter Society*, Vol. 41, No. 1, 1996, pp. 18–29.

[20] Ganguli, R. and Chopra, I., "Aeroelastic Optimization of a Helicopter Rotor to Reduce Vibration and Dynamic Stresses," *AIAA journal*, Vol. 34, No. 4, 1996, pp. 835–854.

[21] Ganguli, R., "Optimum Design of a Helicopter Rotor for Low Vibration Using Aeroelastic Analysis and Response Surface Methods," *Journal of Sound and Vibration*, Vol. 258, No. 2, 2002, pp. 327–344.

[22] Hu, H., Jordan, L. a., and Baeder, J. D., "Computational simulation and analysis of double-swept blade in BVI noise reduction," *Advances in Engineering Software*, Vol. 36, No. 2, Feb. 2005, pp. 67–76.

[23] Glaz, B., Friedmann, P. P., and Liu, L., "Helicopter Vibration Reduction Throughout the Entire Flight Envelope Using Surrogate-Based Optimization," *Journal of the American Helicopter Society*, Vol. 54, No. 1, 2009, pp. 1–15.

[24] Rauch, P., Gervais, M., Cranga, P., Baud, A., Hirsch, J. F., Walter, A., and Beaumier, P., "Blue edge: the design, development and testing of a new blade concept," *Proceedings of 67th Annual Forum of the American Helicopter Society*, Virginia Beach, VA, 2011.

[25] Guglieri, G., "Using of Particle Swarm for Performance Optimization of Helicopter Rotor Blades," Vol. 3, 2012, pp. 1403–1408.

[26] Brocklehurst, A. and Barakos, G. N., "A Review of Helicopter Rotor Blade Tip Shapes," *Progress in Aerospace Sciences*, Vol. 56, Jan. 2013, pp. 35–74.

[27] Ganguli, R., "A Survey of Recent Developments in Rotorcraft Design Optimization," *Journal of Aircraft*, Vol. 41, No. 3, 2004, pp. 493–510.

[28] Millott, T. A. and Friedmann, P. P., "Vibration Reduction in Helicopter Rotors Using an Actively Controlled Partial Span Trailing Edge Flap Located on the Blade," *NASA STI/Recon Technical Report*, , No. June, 1994.

[29] Pearson, J. T., Goodall, R. M., and Lyndon, I., "Active Control of Helicopter Vibration," *Computing and Control ENgineering Journal*, , No. December, 1994.

[30] Johnson, W., "Self-tuning regulators for multicyclic control of helicopter vibration," , No. March 1982, 1982.

[31] Yu, Y., Gmelin, B., Splettstoesser, W., Philippe, J., Prieur, J., and Brooks, T., "Reduction of Helicopter Blade-Vortex Interaction Noise by Active Rotor Control Technology," *Progress in Aerospace Sciences*, Vol. 33, No. 9-10, 1997, pp. 647–687.

[32] Splettstoesser, W., Kube, R., Wagner, W., Seelhorst, U., Boutier, A., Micheli, F., Mercker, E., and Pengel, K., "Key Results from a Higher Harmonic Control Aeroacoustic Rotor Test (HART)," *Journal of the American Helicopter Society*, Vol. 42, No. 1, 1997, pp. 58–78.

[33] Friedmann, P. and de Terlizzi, M., "New Developments in Vibration Reduction with Actively Controlled Trailing Edge Flaps," *Mathematical and Computer Modelling*, Vol. 33, 2001, pp. 1055–1083.

[34] Yu, Y., Tung, C., der Wall, B. V., and Pausder, H., "The HART-II test: Rotor wakes and aeroacoustics with higher-harmonic pitch control (hhc) inputs-the joint german/french/dutch/us project," *the American helicopter Society 58th Annual Forum, Montreal, Canada*, 2002.

[35] Bebesel, M., Roth, D., and Pongratz, R., "Reduction of BVI Noise on Ground - In-Flight Evaluation of Closed-Loop Controller," *Proceedings of 28th European Rotorcraft Forum*, No. September, Bristol, UK, 2002.

[36] Riemenschneider, J. and Keye, S., "Overview of the common DLR/ONERA project active twist blade (ATB)," *Proceedings of the 30th European Rotorcraft Forum*, 2004.

[37] Patt, D., Bernstein, D., Chandrasekar, J., Friedmann, P. P., and Liu, L., "Higher-Harmonic-Control Algorithm for Helicopter Vibration Reduction Revisited," *Journal of Guidance, Control, and Dynamics*, Vol. 28, No. 5, Sept. 2005, pp. 918–930.

[38] Arnold, U. T. P. and Fürst, D., "Closed Loop IBC Results from CH-53G Flight Tests," *Aerospace Science and Technology*, Vol. 9, No. 5, July 2005, pp. 421–435.

[39] JanakiRam, R. D., Sim, B. W., Kitaplioglu, C., and Straub, F. K., "Blade-Vortex Interaction Noise Characteristics of a Full-Scale Active Flap Rotor," *American Helicopter Society 65th Annual Forum*, Grapevine, Texas, 2009.

[40] Tanabe, Y. and Kobiki, N., "Prediction of Noise Reduction by an Active Flap of a Model Rotor," *Proceedings of the 39th European Rotorcraft Forum*, Moscow, 2013.

[41] Pape, A. L., Lienard, C., and Bailly, J., "Active Flow Control for Helicopters," *Journal AerospaceLab*, , No. 6, 2013.

[42] Chia, M. H., Padthe, A. K., and Friedmann, P. P., "A Parametric Study of On-Blade Control Device Performance for Helicopter Vibration and Noise Reduction," *Proceedings of 70th Annual Forum of the American Helicopter Society*, Montreal, Quebec, Canada, 2014.

[43] Straub, F. K., Anand, V. R., Birchette, T. S., and Lau, B. H., "Smart Rotor Development and Wind Tunnel Test," *Proceedings of 35th European Rotorcraft Forum*, Hamburg, Germany, 2009, pp. 1–18.

[44] Morbitzer, D., Arnold, U., and Muller, M., "Vibration and Noise Reduction Through Individual Blade Control Experimental and Theoretical Results," *Proceedings of 24th European Rotorcraft Forum*, Marseille, France, 1998.

[45] Thakkar, D. and Ganguli, R., "Active Twist Control of Smart Helicopter Rotor – A Survey," *Journal of Aerospace Sciences and Technologies*, Vol. 57, No. 4, 2005.

[46] Straub, F. K., Kennedy, D. K., Domzalsky, D. B., Hassan, A. A., Ngo, H., Anand, V. R., and Birchette, T. S., "Smart Material-Actuated Rotor Technology -– SMART," *Journal of Intelligent Material Systems and Structures*, Vol. 15, 2004.

[47] Chopra, I., "Status of Application of Smart Structures Technology to Rotorcraft Systems," *Journal of the American Helicopter Society*, Vol. 45, No. 4, 2000, pp. 228–252.

[48] Chopra, I., "Review of State of Art of Smart Structures and Integrated Systems," *AIAA Journal*, Vol. 40, 2002, pp. 2145–2187.

[49] Cesnik, C. E. S., Opoku, D. G., Nitzsche, F., and Cheng, T., "Active Twist Rotor Blade Modelling Using Particle-Wake Aerodynamics and Geometrically Exact Beam Structural Dynamics," *Journal of Fluids and Structures*, Vol. 19, 2004, pp. 651–668.

[50] Chen, P. C., Baeder, J. D., Evans, R. a. D., and Niemczuk, J., "Blade-Vortex Interaction Noise Reduction with Active Twist Smart Rotor Technology," *Smart Materials and Structures*, Vol. 10, No. 1, Feb. 2001, pp. 77–85.

[51] Glaz, B., *Active/Passive Optimization of Helicopter Rotor Blades for Improved Vibration, Noise, and Performance Characteristics*, Ph.D. thesis, 2008.

[52] Piccione, E., Anobile, A., Bernardini, G., and Gennaretti, M., "Optimal Design and Acoustic Assessment of Swept-Tip Helicopter Rotor Blades," *Proceedings of ISMA Noise and Vibration Engineering Conference*, Leuven, Belgium, 2012, pp. 587–602.

[53] Bernardini, G., Anobile, A., Piccione, E., and Gennaretti, M., "Genetic Algorithm with Surrogate Wake Inflow Models for Helicopter Rotor Optimal Design," *Proceedings of XXII AIDAA Conference*, Naples, Italy, 2013.

[54] Anobile, A., Bernardini, G., and Gennaretti, M., "Active Twist Rotor Controller Identification for Blade-Vortex Interaction Noise Alleviation," *Proceedings of 19th AIAA/CEAS Aeroacoustics Conference*, Berlin, Germany, May 2013.

[55] Anobile, A., Bernardini, G., Testa, C., and Gennaretti, M., "Synthesis of Rotor BVI Noise Active Controller Through Efficient Aerodynamics/Aeroacoustics Solver," *Proceedings of 20th AIAA/CEAS Aeroacoustics Conference*, Atlanta, USA, 2014.

[56] Celi, R., *Aeroelasticity and Structural Optimization of Helicopter Rotor Blades with Swept Tips*, Ph.D. thesis, University of California, Los Angeles, 1987.

[57] Celi, R. and Friedmann, P. P., "Aeroelastic Modeling of Swept Tip Rotor Blades Using Finite Elements," *Journal of the American Helicopter Society*, Vol. 33, No. 2, 1988, pp. 43–52.

[58] Bir, G. S. and Chopra, I., "Aeromechanical Stability of Rotorcraft with Advanced Geometry Blades," *Mathematical and computer modelling*, Vol. 19, No. 314, 1994, pp. 159–191.

[59] Hodges, D. H. and Dowell, E. H., "Nonlinear Equations of Motion for the Elastic Bending and Torsion of Twisted Nonuniform Rotor Blades," *NASA TN D-7818*, 1974.

[60] Hodges, D. H. and Ormiston, R. A., "Stability of Elastic Bending and Torsion of Uniform Cantilever Rotor Blades in Hover with Variable Structural Coupling," *NASA TN D-8192*, 1976.

[61] Greenberg, J. M., "Airfoil in Sinusoidal Motion in a Pulsating Stream," *NACA TN-1326*, 1947.

[62] Gennaretti, M. and Bernardini, G., "Novel Boundary Integral Formulation for Blade–Vortex Interaction Aerodynamics of Helicopter Rotors," *AIAA Journal*, Vol. 45, No. 6, June 2007, pp. 1169–1176.

[63] Murugan, M. S., Ganguli, R., and Harursampath, D., "Surrogate Based Design Optimisation of Composite Aerofoil Cross-Section for Helicopter Vibration Reduction," *Aeronautical Journal*, Vol. 116, No. 1181, 2012, pp. 709–725.

[64] Mallick, R., Ganguli, R., and Bhat, M. S., "Robust Design of Multiple Trailing Edge Flaps for Helicopter Vibration Reduction: A Multi-Objective Bat Algorithm Approach," *Engineering Optimization*, , No. October 2014, Oct. 2014.

[65] Holland, J. H., *Adaptation in Nature and Artificial Systems*, Ann Arbor, 1975.

[66] Goldberg, D. E., "Optimal Initial Population Size for Binary-Coded Genetic Algorithms," Tech. rep., TCGA Report No. 85001, University of Alabama, Tuscaloosa, Alabama, 1985.

[67] Haykin, S., "Neural Networks: A Comprehensive Foundation," *Neurocomputing*, Aug. 1999.

[68] Zaknich, "Introduction to neural networks," *Neural Networks for Intelligent Signal Processing*, 2003.

[69] Ffowcs Williams, J. and Hawkings, D., "Sound Generation by Turbulence and Surfaces in Arbitrary Motion," *Philosophical Transactions of the Royal Society A: Mathematical, Physical and Engineering Sciences*, Vol. 264, No. 1151, May 1969, pp. 321–342.

[70] Fung, Y. C., *An Introduction to the Theory of Aeroelasticity*, Dover Phoenix Edition: Engineering, Dover Publications, Incorporated, 2002.

[71] Gennaretti, M., Testa, C., Bernardini, G., and Anobile, A., "An Analytical–Numerical Aerodynamic Formulation for Efficient Aeroacoustics Analysis of Rotorcraft," *Proceedings of the ASME 2012 Noise Control and Acoustics Division Conference*, New York City, 2012.

[72] Gennaretti, M., Testa, C., and Bernardini, G., "An Unsteady Aerodynamic Formulation for Efficient Rotor Tonal Noise Prediction," *Journal of Sound and Vibration*, Vol. 332, No. 25, Dec. 2013, pp. 6743–6754.

[73] Anobile, A., Bernardini, G., and Gennaretti, M., "Investigation on a High-Frequency Controller for Rotor BVI Noise Alleviation," *International Journal of Acoustics and Vibrations*, Vol. in press, 2015.

[74] Bernardini, G., Serafini, J., Ianniello, S., and Gennaretti, M., "Assessment of Computational Models for the Effect of Aeroelasticity on BVI Noise Prediction," *International Journal of Aeroacoustics*, Vol. 6, No. 3, Sept. 2007, pp. 199–222.

[75] Theodorsen, T., "General Theory of Aerodynamic Instability and the Mechanism of Flutter," *NACA Report 496*, 1935.

[76] Gennaretti, M. and Bernardini, G., "Aeroelastic Response of Helicopter Rotors Using a 3D Unsteady Aerodynamic Solver," *The Aeronautical Journal*, Vol. 110, No. 1114, 2006, pp. 793–802.

[77] Gennaretti, M., Molica Colella, M., and Bernardini, G., "Prediction of Tiltrotor Vibratory Loads with Inclusion of Wing-Proprotor Aerodynamic Interaction," *Journal of Aircraft*, Vol. 47, No. 1, Jan. 2010, pp. 71–79.

[78] Gennaretti, M. and Bernardini, G., "Aeroacousto-Elastic Modeling for Response Analysis of Helicopter Rotors," *Variational Analysis and Aerospace Engineering: Mathematical Challenges for Aerospace Design*, edited by G. Buttazzo and A. Frediani, Springer Optimization and Its Applications, Berlin, 2012, pp. 27–50.

[79] Gennaretti, M., Luceri, L., and Morino, L., "A unified boundary integral methodology for aerodynamics and aeroacoustics of rotors," *Journal of sound and vibration*, Vol. 200, 1997, pp. 467–489.

[80] Bernardini, G., Serafini, J., Molica Colella, M., and Gennaretti, M., "Analysis of a Structural-Aerodynamic Fully-Coupled Formulation for Aeroelastic Response of Rotorcraft," *Aerospace Science and Technology*, Vol. 29, No. 1, Aug. 2013, pp. 175–184.

[81] Lighthill, M. J., "On Sound Generated Aerodynamically. I. General Theory," *Proceedings of the Royal Society of London A: Mathematical, Physical and Engineering Sciences*, Vol. 211, No. 1107, March 1952, pp. 564–587.

[82] Brentner, K., "Prediction of helicopter rotor discrete frequency noise: a computer program incorporating realistic blade motions and advanced acoustic formulation," *NASA - TM 87721*, 1986.

[83] Farassat, F., "Derivation of Formulations 1 and 1A of Farassat," *NASA TM 214853*, 2007.

[84] Johnson, W., *Helicopter Theory*, Dover Books on Aeronautical Engineering Series, Dover Publications, 1994.

[85] Leishman, J. G., *Principles of Helicopter Aerodynamics*, Cambridge aerospace series, Cambridge University Press, 2002.

[86] Smith, R. E. and Smuda, E., "Adaptively Resizing Populations: Algorithm, Analysis, and First Results," *Complex Systems*, Vol. 9, No. 1, 1995, pp. 47–72.

[87] Haftka, R. T. A. and Gurdal, Z. A., *Element of Structural Optimization*, Kluwer Academic Publishers, Dordrecht, 1992.

[88] Venkatesan, C., Friedmann, P. P., and Yuan, K. A., "A New Sensitivity Analysis for Structural Optimization of Composite Rotor Blades," *Mathematical and Computer Modelling*, Vol. 19, No. 3-4, 1994, pp. 1–25.

[89] Gennaretti, M., Colella, M. M., and Bernardini, G., "Analysis of helicopter vibratory hub loads alleviation by cyclic trailing-edge blade flap actuation," *The Aeronautical Journal*, Vol. 113, 2009, pp. 549–556.

[90] Drees, J. M., "A Theory of Airflow Through Rotors and Its Application to Some Helicopter Problems," *Journal of the Helicopter Association of Great Britain*, Vol. 3, No. 2, 1949, pp. 77–104.

[91] Schöll, E., Splettstoesser, W., and Pongratz, R., "Noise Reduction by Blade Root Actuation-Analysis of Flight and Wind Tunnel Tests," *Proceedings of 24th European Rotorcraft Forum*, Marseilles, France, 1998.